Barite nucleation - Measuring effects of solution stoichiometry on crystal population and critical nucleii size

David J. Riedinger

Abstract Crystal growth is ubiquitous in natural and anthropogenic systems. Comprehension of the effects of solution stoichiometry on crystal growth is very limited. Barite is chosen as a model crystal due to its relevance in the hydrocarbon and geothermal industry and the effects of solution stoichiometry ($r_{aq} = \frac{\{Ba^{2+}\}}{\{SO_4^{2-}\}}$) varying between $r_{aq} = 0.01$ and $r_{aq} = 100$ on crystal nucleation are researched. The development is explored at different supersaturations. Supersaturation is defined as $\Omega = IAP/K_{SP}$ where IAP is the ion activity product and K_{SP} the solubility product. $\Omega = 100$ and $\Omega = 500$ in regards to barite are measured. A synergistic approach of dynamic light scattering (DLS), scanning electron microscopy (SEM) and small angle X-ray scattering (SAXS) is used to determine the size of stable populations at different stoichiometries, the critical nucleus size and crystal shape. The dominant crystal size is 400nm (equivalent sphere) at all stoichiometries and supersaturation. At $\Omega = 100$, the largest crystals are observed at $r_{aq} > 1$ and at $\Omega = 500$ at $r_{aq} = 1$. Barium desolvation seems to be a limiting step in crystal growth. Critical nucleus size generally slightly decreases with increasing barium activity. There is a strong stoichiometric effect on crystal morphology, with a high shape variation at $\Omega = 500$ and $r_{aq} = 0.1$ and $r_{aq} = 10$ and very limited effects at other measured stoichiometries. Varying stoichiometry is a promising solution to scale formation in geo-industry by inhibiting crystal nucleation through application of extreme stoichiometries modifying growing and nucleation behaviour.

GEO4-1521
Master Thesis (37.5 ECTS)
Date 22/06/2020
First supervisor: Dr. Mariëtte Wolthers (Utrecht University)
Second supersivors: Sergej Seepma Msc (Utrecht University)

Acknowledgements

Special thanks goes out to Mariëtte Wolthers for providing the research idea, allowing me to participate as a full member of her research team and creating the unique opportunity to conduct research at the ALBA synchrotron. Sergěj Seepma for the help and guidance in the lab. Annet Baken for being a constant beaken of answers for all my R and Python questions. Sergio Ruiz-Hernandez and Janou Koskamp for working on the automation of the Minteq software and John Visser for staying in the lab till late in the evening to allow me to finish my experiments on time and in general for being good company.

Contents

List of Figures

List of Tables

1

Introduction

Crystal formation in aqueous environments plays a critical role in a wide variety of natural and anthropogenic systems. Understanding the effects of stoichiometry on crystal nucleation is immediately applicable to a variety of industries such as the oil-and-gas industry (Delshad et al. (2003)), hydro-geothermal (Wittenberger and Šofranko (2015)). In these industries, barite scaling is a major issue due to its very low solubility (Yuan and Wood (2018)), its resistance to chemical and acid removal (Christy and Putnis (1993); Dove and Czank (1995)) and its hardness (Mavredaki et al. (2011)). These characteristics do make sedimentary barite a suitable proxy to study the history of biogeochemical cycles on earth (Table 1.1). Scaling minerals are formed through a reaction of oppositely charged ions. There is extensive research on the growth and dissolution rates of crystals and crystal surface deposition under charge and non-charge balanced ion ratios ((Crabtree et al., 1999); (Kitamura, 2002); (Dyer and Graham, 2002); (Yu et al., 2004); (Peyvandi et al., 2012); (Wolthers et al., 2012)). Yet many systems deviate from our expectations regarding crystal nucleation and growth rate. This is due to most studies being conducted using ideal solutions with charge-balanced ionic ratios ($r_{aq} = 1$) or using titration set-ups, whereas these systems have widely diverging ratios and are more similar to batch experiments. The dependency of nucleation on the stoichiometry has not been thoroughly researched.

This disconnect between our expectations and observations illustrates a gap in our understanding of stoichiometric effects on the rate of crystal formation. This study aims to provide insights into the effects of widely diverging ionic ratios on the nucleation rate of barite and to provide experimental data to compare with previously published research on calcite nucleation under the same conditions (Seepma et al., in prep).

The driver of barite scale formation in the hydrocarbon industry is the mixing of incompatible waters during enhanced oil recovery. For instance, to maintain high pressure and thus production during later stages of oil or gas production in the offshore industry and to sweep the oil towards production sites, seawater is often injected into the reservoir. This seawater is naturally high in sulfate (Forchhammer (1865)) whereas formation water is generally rich in dissolved barium (Merdhah and Yassin (2007); BinMerdhah et al. (2010)). Upon mixing, barite quickly precipitates from these concomitant waters, lowering permeability and porosity in the reservoir (Yuan et al. (1994)), clogging the wellbore and strongly reducing the integrity of components such as the subsurface control valve and hydraulic actuators(Vazirian et al. (2016)). After the initial deposition of barite in the reservoir, the water reaches equilibrium at reservoir conditions, as pressure and temperature decrease, the water becomes supersaturated in regards to barite and precipitation occurs (BinMerdhah et al. (2010)). This leads to lower production efficiency and incurs major costs for the industry (Collins (2005)). Adhesion of pre-precipitated crystal is specifically problematic

at ground level (Vazirian et al. (2016)) and mediating this through the prevention of nucleation under specific ionic ratios would increase efficiency. Tests have been performed with de-sulphated seawater to prevent the aforementioned problems, but this is however not economically viable (Jordan et al. (2001)). Understanding the initial stages of barite nucleation could potentially provide a cost effective and environmental friendly way to prevent these problems. More examples of the importance of barite in both industry and research are provided in Table 1.1

Table 1.1: Applications and problems of natural and industrial barite

Subject	Field	Source
Prevention of barite scaling in oil, gas and geothermal wells	Energy industry	Delshad et al. (2003); Tomson et al. (2004a); Collins (2005); Zhang et al. (2017)
Low toxic and non-magnetic weighting agent for drilling mud	Energy/Water Extraction	Rabia (1985); Mitchell et al. (2006)
Measuring paleo-productivity and climate through a marine barite proxy	Paleo-reconstruction	Paytan et al. (1993); Paytan et al. (1996); Stroobants et al. (1991); Hanor (2000)
Producing barium meal for Upper Gastrointestinal Endoscopy	Medical industry	DOOLEY et al. (1984)
Barite inclusion into x-ray shielding	Nuclear industry	Akkurt et al. (2010); Akkurt and El-Khayatt (2013)

1.1 Historical perspective barite research

Historically, research on barite formation has focused strongly on mineral properties, mining and scaling prevention methods as these were the main concerns of the petroleum (Read et al. (1982); Corsi (1986)) and mining industry (Stuckey and Davis (1933); Fritts (1962); Raghu (2001)). Subsequently, it was found to be a suitable proxy for paleo-environmental analysis (Jewell and Stallard (1991); Gingele and Dahmke (1994); Ahsan and Mallick (1999); Eagle et al. (2003); Gillikin et al. (2006); Arndt et al. (2009)). With the advent of dynamic light scattering (DLS) (Stetefeld et al. (2016)) and Small-angle X-ray scattering (SAXS) (Guinier (1939)), real time measurements of 3D-nucleation became possible. Recent technological advances like atomic force microscopy in 1985 (Rugar and Hansma (1990)), which offered resolution on the order of fractions of a nanometers, enabled highly detailed research into the growth of minerals. This resulted in influential research on crystal growth processes in general (Hillner et al. (1992); Zhang and Nancollas (1998)) and investigations specifically focussed on barite surface growth and 2D-nucleation (Pina et al. (1998); Kowacz and Putnis (2008)).

1.2 Thesis Outline

The aim of this research is to experimentally investigate the dependency of barite nucleation on stoichiometry ($r_{aq} = \{Ba^{2+}\}/\{SO_4^{2-}\}$). Specifically focusing on timing, aggregation behaviour and size and shape. This is done at different supersaturation degrees ($\Omega = IAP/K_{SP}$, IAP being the

ion activity product and K_{SP} the solubility product). This research aims to answer three specific research questions.

1. Does stoichiometry affect crystal populations at constant supersaturation?
2. Does critical nucleus size depend on the stoichiometry?
3. Is crystal shape dependent on stoichiometry?

Understanding these dependencies is part of the larger Crystal Clear project (Wolthers et al. (2012)). The results are also evaluated to determine different growth modes (subcritical particle aggregation *vs* ion addition). To understand the experimental data and substantiate the chosen physico-chemical parameters, relevant aspects to barite nucleation are described, background theory is provided and previously published literature and its specific relevance to this project is discussed. Additionally, the physics background of DLS, scanning electron microscopy (SEM) and SAXS measurement technique are elaborated on (Section 2.2). Subsequently, the theoretical calculations, experimental set-up and research method are described, with a specific focus on validity, reliability and suitability. Additionally, justification for the chosen research method is provided and potential pitfalls of the method are identified (Section 3). Afterwards, collected experimental data is presented, precision and accuracy are included to facilitate the reader to create their own line of thinking (Section 4). Section 5 discusses the potential answers to the research questions above, discusses the individual results, synthesizes the experimental results and relates them to previous literature, explores and debates alternative explanations, provides the societal relevance and addresses the limitations of the research. Lastly, the most important conclusions (Section 6) are presented, the research questions are answered and implications for the larger field of crystal nucleation are provided with the arguments for the exclusion of rivaling explanations.

2

Theoretical Background

The following chapter will discuss the nucleation process from a thermodynamic and kinetic point of view. Provide the principles of the dynamic light scattering, small-angle X-ray scattering and the scanning electron microscope.

2.1 Theoretical background of nucleation

Homogeneous nucleation follows several consecutive steps. The initial step entails the formation of an unstructured aggregate of ions, the growth to a critical nucleus, restructuring into a distinct crystal shape and the subsequent addition of growth units (Figure 2.1). This paragraph discusses these steps and the theoretical considerations behind them.

The first theoretical framework for crystal nucleation, classical nucleation theory (CNT) was developed 150 years ago by Josiah Willard Gibbs (Gibbs (1878)). It describes the nucleation based on the tendency of a system to equilibrate at the lowest possible Gibbs free energy. The original nucleation theory was based on cloud condensation, but it is widely utilized to describe the formation of a solid phase from an aqueous phase. The following paragraphs will discuss individual parameters essential for nucleation.

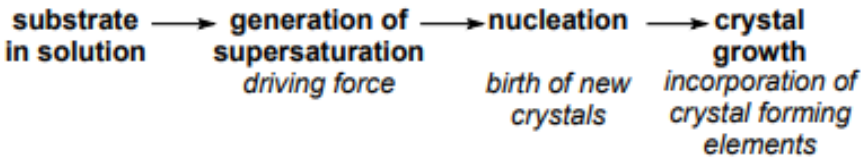

Figure 2.1: Generalized scheme of crystal formation (Adapted from Dalmolen, J.2005)

2.1.1 Supersaturation

Supersaturation is a state where the product concentration of the relevant crystal building ions is higher than the solubility of the relevant crystal phase. As a general rule, temperature decreases result in saturation state increases (Figure 2.2), notable examples include calcite ($CaCO_3$). The lowered solubility is a direct consequence of the changing thermodynamic circumstances. In undersaturated state (1), no crystal nucleation occurs and any pre-existing crystal structures are

thermodynamically unstable and likely to dissolve. At lower temperatures or higher ion concentrations, metastable state (2) is reached. This state will be discussed in the subsequent paragraph. In a state of supersaturation, also known as labile, a phase change is likely to occur at minimal disturbance triggering nucleation (Figure 2.2). These crystals will subsequently grow until equilibrium at the present conditions is reached. This nucleation and growth can be either endothermic or exothermic, consequently the progress of the precipitation reaction can result in increases or decreases in temperature. Mathematically, the saturation index is defined according to Equation 2.1

$$SI = \frac{(IAP)}{Ksp} \tag{2.1}$$

Where SI is the saturation index, IAP the ion activity product and K_{sp} their solubility product of the mineral. SI > 0 indicates supersaturation and precipitation of the mineral will occur. SI < 0 indicates undersaturation, and if the mineral is present, dissolution occurs (Stanton (1996)).

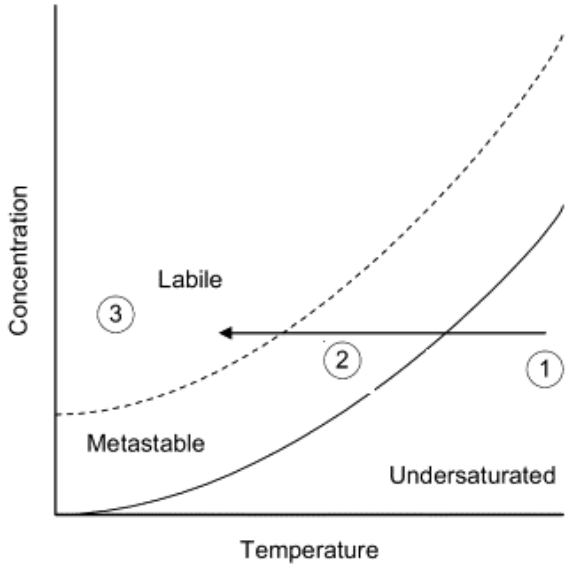

Figure 2.2: Effects of ion concentration and temperature on the state of supersaturation of most minerals (Adapted from Reklaitis et al. (2017)),

2.1.2 The Metastable state

When the parent phase (the pre-nucleation phase) is metastable, nucleation can occur (Figure 2.2). This metastable state represents a local minimum in Gibbs free energy. This state is stable to minor changes in the thermodynamic variables but will evolve into a state where it is at a global minimum of free energy (bulk solid) when $t \to \infty$. The critical nucleus size controls the probability of a nucleus to form and thus the timescale on which a crystal will start to form. To achieve this transformation, the system needs to overcome a local maximum of free energy. This maximum is an unstable equilibrium state or transition state, where minor fluctuations in the thermodynamics of the systems cause the formation of a stable new phase (Figure 2.3).

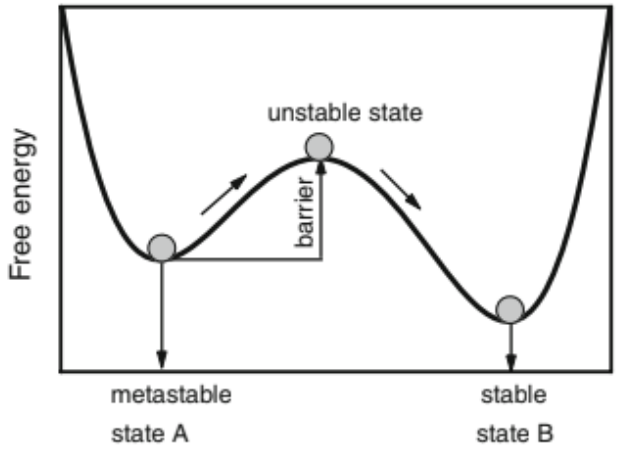

Figure 2.3: A sketch of the energy barrier that the metastable state A (supersaturated liquid) needs to overcome in order to reach the stable state B (bulk solid) adapted from (Adapted from Classical Nucleation Theory by Kalikmanov (2013))

2.1.3 Critical nuclei formation

Three dominant theories for the formation of critically sized nuclei exist. Classical nucleation theory states that growth towards a critical size occurs due to ion addition to subcritical particles (Cölfen and Mann (2003)). The second theory states that subcritical particles aggregate and coalesce, almost instantaneously transforming from multiple subcritical particles to a supercritical particle (Ogino et al. (1987); Gebauer et al. (2008)) (Figure 2.4). The third theory explains cluster and subsequent crystal formation through a two-step process, where the first step is the formation of a dense cloud of ions, which exists as a microemulsion of liquid-like particles. The second step is the rearrangement of the dense cloud of particles into a crystal structure (2.5). These mechanisms are not necessarily exclusive and will potentially contribute to different extents under different physio-chemical parameters. These parameters will be further explored in the coming chapter. Many details of these theories stay ambiguous (Meldrum and Sear (2008); Cölfen (2010)), but it is clear that their effect on the nucleation time and rate will be different as will be the particle size distribution during nucleation and growth.

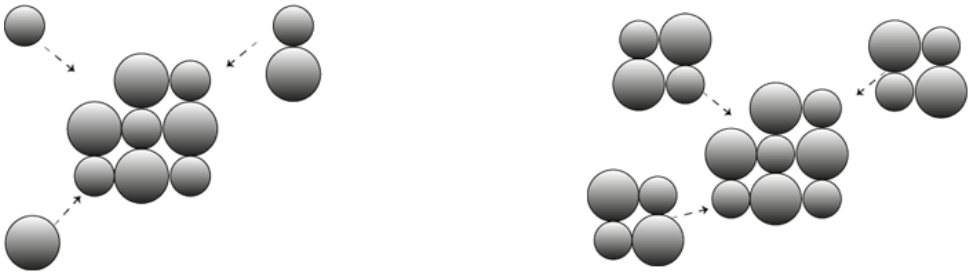

Figure 2.4: left: Single ion or building block addition, critical nuclei growth according to classical nucleation theory. Right: Coalesence of multiple pre-critical nuclei to form a supercritical nucleus.

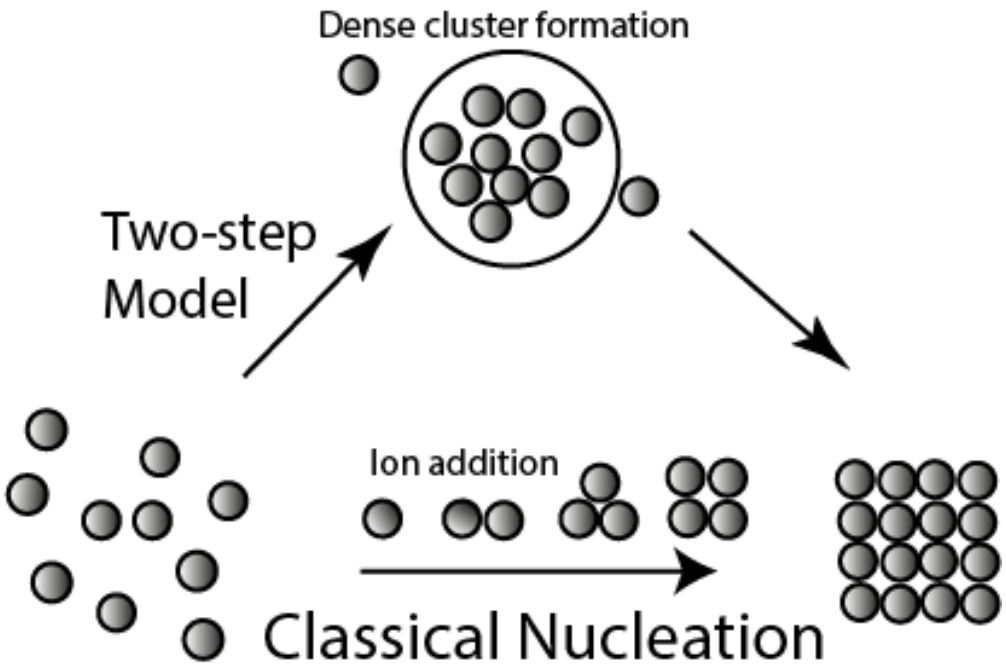

Figure 2.5: Original classical nucleation theory for cluster formation and modern two-step approach

Classical nucleation theory limitations and alternative

In order for classical nucleation theory to be valid, a number of assumptions have to be made. Predictions made with CNT do not generally align with measurements and observations. Even for the most simple systems, single-component fluids or condensation of water droplets from a cloud, CNT predicts nucleation rates that are one to two orders of magnitudes higher than the experimentally defined rates (Sharaf and Dobbins (1982)). This discrepancy is most presumably the result of major assumptions. Firstly, uniform density throughout the newly formed cluster is assumed, implying strong ordering, akin to that of the fully grown crystal. This is not the case according to the two-step model. Secondly, the surface tension is assumed to be temperature and curvature (size) independent (Fokin and Zanotto (2000)), meaning that the effects of surface curvature are not critical nucleus size dependent, which they are (Fokin and Zanotto (2000)), and is equivalent to the respective interfacial tension if the phases would coexist in a stable manner at a planar interface (Laaksonen and Napari (2001)). Essentially, this means that the crystal is ordered in the same manner at the critical nucleus size as when it is fully grown. This results in identical surface tensions (De Yoreo and Vekilov (2003)). This is known as the capillarity approximation. Thirdly, all clusters are assumed to be at rest, no translational, vibrational or rotational motion exists and all non-ion-addition interactions are ignored. Fourthly, all processes are described in terms of steady-state kinetics and all subcritical clusters are present immediately after supersaturation is established.

The two-step nucleation model

The two-step model (Figure 2.5) fits experimental observations of nucleation for organics and colloids much better (Georgalis et al. (1997); Pontoni et al. (2004)) and is supported by a numerical simulation of homogeneous crystal nucleation (ten Wolde and Frenkel (2016)) which predicts the much higher observed nucleation rates due to a strong reduction in free-energy barrier (Figure 2.3) for protein synthesis in the two-step model. Besides experimental and computational support

for the two-step model, theoretical studies have also provided evidence for a two-step process (Talanquer and Oxtoby (1998)). This subdivision of nucleation into two steps also divides the thermodynamic energy barrier into two parts. The first, low energy, barrier is for the formation of the dense ion cloud, the second for the ordering of the pre-nucleus. This second step is the rate determining step (Filobelo et al. (2005)) due to its higher energy barrier. The energy barrier for this step is however lower than for CNT and as a result, the nucleation rate is higher. The theory also introduces an area in the vicinity of the dense cloud or pre-nucleus which has a higher concentration of ions. Consequently, the sharp boundary between nucleus and solvent, as proposed by CNT, does not exist (Haas and Drenth (2000)) and is more accurately described as a concentration gradient. Although most studies regard protein nucleation, its findings are relevant to ion-crystal nucleation as well, because both processes are underlain by the same fundamental driving forces and limitations. For this research, the exact pathway of cluster formation is not the research target. It is assumed that a mix of processes occurs and in order to foster understanding, the thermodynamic and kinetic considerations are expatiated from the viewpoint of CNT.

2.1.4 Thermodynamics

The driving force of a phase change is the exceedance of Gibbs free energy of the aqueous phase compared to the energy of a potential new solid phase (Hohenberg and Halperin (1977); Chaikin et al. (1995)). The bulk of the potential new phase has a lower Gibbs free energy compared to the surrounding phase (Sun and Seider (1995)). At the interface between the two phases, a certain degree of disruption of intermolecular bonds occurs. This disruption is known as interfacial free energy and the surfaces are intrinsically less energetically favourable than the bulk of the material (Li and Ishigaki (2002)). In nanoparticles, the ratio between bulk and surface is small, making the newly formed phase unstable and prone to dissolution (Liu et al. (2007)). As the particle increases in size, the ratio between the bulk phase and the surface of the new phase becomes more energetically favourable. A cluster N_c contains sufficient molecules to overcome the critical energy barrier and is known as the critical nucleus. When the amount of molecules in an aggregate is smaller than N_c ($N < N_c$), the particle will on average dissociate, whereas $N > N_c$ will promote growth of the aggregate (Figure 2.6). It has surpassed the CNT free energy barrier, also called the nucleation barrier. N_c is not a set amount of molecules, but depends on local variables, which vary and fluctuate throughout the bulk liquid. Therefor it's preferable to discuss a critical size region instead of a critical size. The formation of small solid clusters of ions and molecules is a continuous

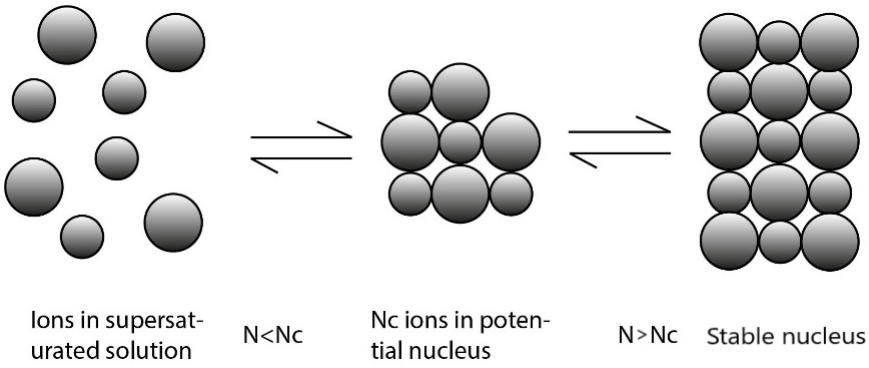

Figure 2.6: Critical nucleus size illustrated

process, only stable new phases are referred to as a nucleus. The Gibbs free energy of these clusters is divided into ΔG_v (Free energy of the bulk phase) and ΔG_s (Interfacial energy), The clusters

that have a net negative Gibbs Free Energy ($\Delta G_r < 0$) grow (2.3)($N > N_c$). All other preliminary clusters on average dissolve again into individual ions($N < N_c$). This critical size is strongly dependent on physico-chemical conditions and can vary between 1 and 10nm, but under extreme conditions can be as large as 100nm (De Yoreo and Vekilov (2003)). At this critical size, the Gibbs free energy continuously decreases with growth. Consequently, the nucleus remains stable and likely grows as long as the medium is supersaturated with respect to the growing mineral. During this growth, additional new nuclei form in the solution (3D-nucleation) and 2D-nucleation occurs simultaneously on the crystal surface. Particles with a size in the range of the critical nucleus size are expected to be the most prominent in an emerging system, due to the diffusion limitation on further growth (Chernov (1961); Zettlemoyer (1969)). Very small particles are limited only by transition state (Petsev et al. (2003)) The change in free energy during the formation of a critical nucleus (ΔG_r) can be expressed by the following relationships (Porter et al. (2009))

$$\Delta G_r = \Delta G_v + interface_{area} * \gamma + Strain_{energy} \tag{2.2}$$

where G_v is the free energy of the bulk and γ the surface Gibbs energy per unit area (surface tension) or ΔG_s. Note that G_v is negative. For liquid to solid transition, an increase in strain energy can be disregarded (Kalyanaraman (2008)) and by assuming the critical nucleus is round, which minimizes the free energy of the interface, the following equations can be derived (Kashchiev (2000)):

$$\Delta G_v = -\frac{4\pi r^3}{3a^3}\Delta\mu \tag{2.3}$$

where r is the cluster size, a is the size of individual growth units and $\Delta\mu$ is the chemical potential difference between the growth units ($\mu_s ol$) in solution and in the nucleus ($\mu_n uc$) and defined as follows:

$$\Delta\mu = \mu_{sol} - \mu_{nuc} = kTln(\frac{c}{c_0}) \tag{2.4}$$

where c is the concentration of growth units in the solution and c_0 the equilibrium concentration of growth units in the solution in a saturated solution. This directly relates to the degree of supersaturation $\Omega = \frac{c}{c_0}$. The interfacial energy term (ΔG_s) is positive and can be calculated for the specific nucleus surface area by:

$$\Delta G_s = \frac{4\pi r^2}{a^2}\gamma \tag{2.5}$$

When these equations are combined, the overall energy change due to nucleus formation can be calculated:

$$\Delta G_r = -\frac{\Delta\mu(\frac{4}{3})\pi r^3}{a^3} + \gamma\frac{4\pi r^2}{a^2} \tag{2.6}$$

ΔG_v becomes increasingly negative (cubically) as cluster size (r) increases. ΔG_s increases quadratically with increasing cluster size. Below $r = 1$, the lower power dominates and above the higher power. Resulting in a maximum in the ΔG vs r plot. This maximum can be found by $d\Delta G/dr = 0$, This gives equation (Nehrke (2007)):

$$r_{crit} = \frac{2\gamma a}{\Delta\mu} = \frac{2\gamma a}{kTln(\frac{c}{c_0})} \tag{2.7}$$

The activation energy of the formation of a critical nucleus naturally follows from by inserting this equation into Equation 2.6.

$$\Delta G_r* = \frac{16\pi\gamma^3}{3[K_b T\ln(\Omega)]^2} \tag{2.8}$$

This is the energy barrier to nucleation. It becomes clear that this barrier decreases with increasing supersaturation (Ω). From Equation 2.3, the aforementioned continuous growth of a critically sized nucleus becomes immediately apparent, growth being energetically more favourable than stagnation as long as the relative supersaturation remains sufficiently high (ΔG_r remains negative).

The relationship between these energies is shown in the following graph 2.7. This is a thermo-

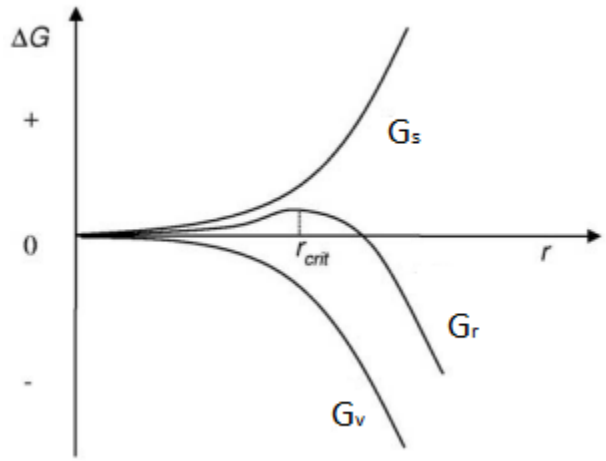

Figure 2.7: Interfacial free energy (ΔG_s) and bulk free energy (ΔG_v) of an emerging nucleus. r_{crit} is the critical nucleus size, at which the nucleus becomes stable adapted from Sunagawa (2007). This critical nucleus size becomes smaller as supersaturation increases

dynamic description of homogeneous nucleation in CNT, dependent on supersaturation but not on solution stoichiometry.

2.1.5 Kinetics

Classical nucleation theory states that increasing the supersaturation and/or reducing the interfacial tension increases the nucleation rate by lowering the nucleation barrier.

The free energy of formation can be related, according to CNT, to the rate at which nuclei are formed (J) through the following relationship (Nielsen (1964); Abraham (1974) Strey et al. (1994); Wyslouzil and Wölk (2016)):

$$J = k * e^{(-\Delta G^* / K_b T)} \tag{2.9}$$

Where J is the rate of nucleation [number m^{-3} s^{-1}] (Volmer and Weber (1926)), k is the kinetic pre-exponential factor (provided by Farkas (1927)) and T is the temperature [K].

Experiments have shown that under identical conditions, except the type of background electrolyte, the kinetic pre-exponential factor (k) varies. The kinetic barrier (k) can be the rate limiting factor in crystal nucleation. The kinetic barrier is "proportional to the diffusion constant" (Kowacz et al. (2010)). In order to form ion-pairs and eventually aggregates, effective ion contact needs to occur. Ion association is facilitated by water exchange between the solvation shell and the bulk fluid ($f(H_2O)$) (Lee and Rasaiah (1994); Chong and Hirata (1997); Lynden-Bell et al. (2001)). $f(H_2O)$ is a balance between the tendency of ions to order the water molecules in their solvation shell and the preservation of the hydrogen-bond-network of water (Hribar et al. (2002)). Due to different background electrolytes in the solvent, ion-water affinity can increase or water-water

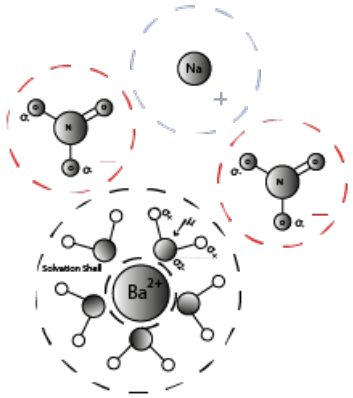

Figure 2.8: Schematic overview of the effects of electrolytes on solvation shell stability

affinity can decrease. Both increase the residence time of water in the solvation shell, making k less favourable while simultaneously decreasing interfacial tension, respectively decreasing and increasing nucleation rate (Kowacz et al. (2007)). These effects have also been documented in molecular simulation studies (Piana et al. (2006); Jones et al. (2008)) on 2D-nucelation. 3D-nucleation in a multicomponent electrolyte solution is also strongly affected, because the starting point of any nucleation event of an ionic crystal, is the contact between a cation and anion with dehydrated solvation shells. All these individual factors are summarised in k and can be used to calculate J. The rate-limiting step of nucleation is different depending on parent-phase properties. Providing more favourable conditions for nucleation will not increase the rate except if the speed of the rate-limiting step is increased.

Electrolyte solution and ionic strength

The residence time is defined as t_i/t_0, the ratio between the time of a molecule of water in the closest possible location to the ion and the time in the bulk solvent. At higher ionic strengths, the position of the water molecule in the solvation shell is stabilized.

Anions are naturally more proximal to cations than cations to cations due to electrostatic interactions. The partial charge of the dipole moment of water (u), is affected by both the charge of the cation (Ba^{2+}) and the anion (NO_3^-) (Figure 2.8). These ions move as one complex, reducing the water exchange rate in their respective solvation shells by lowering their potential energy. Some anion-cation interactions exist however, where the exchange rate increases due to the addition of the background electrolyte, notably the Mg^{2+}/Br^- system (Di Tommaso and De Leeuw (2010)). The effects of the electrolyte solution on the water exchange rate can be influenced by different characteristics of the background electrolytes. At low ionic strengths ($I < 0.05$), electrostatic interactions are dominant. Consequently, background electrolyte pairs are formed, strongly decreasing their effect on the hydration shells of the barite forming ions and, thus their hydration characteristics. Background electrolyte pair formation is directly related to the respective solubility of the electrolytes. More soluble ions retard barite nucleation rates to a higher degree than less soluble background electrolytes (Kowacz et al. (2010)). At relatively high ionic strengths ($I > 0.05$), the individual charge distribution within the ion pairs is of minor importance due to the suppression of electrostatic interactions and the overlap of ion hydration shells (Kowacz et al. (2010)). There is a distinct switch to long range electrostatic interactions at these high ionic strengths. These long range interactions consist of two components and the relative importance of these components dependents on the characteristics of the background ion, predominantly their affinity to

water (Kowacz et al. (2010)). Ions with a strong affinity compete with the crystal building ions and increase the water frequency exchange rate($f(H_2O)$). Whereas in electrolytes with a lower water affinity, the structure created in the water in their direct vicinity (Koneshan et al. (1998)) decreases $f(H_2O)$ due to decreased water mobility. At very high ionic strengths ($I > 0.1$), ion concentrations are sufficiently high that bulk water is structured (Kowacz et al. (2010)). The main kinetic barrier for nucleation can be the water exchange frequency and the likelihood of effective (dehydrated) contact between two crystal building ions and is directly related to water solvent dynamics and the amount of reactive material in the system.

Regarding growth and particle size, it is worth noting that in general higher I leads to retardation of crystal growth, due to the electrostatic stabilization of the bulk water (Kowacz et al. (2010)). The effect of increasing supersaturation (Ω) depends on the hydration characteristics (positive versus negative) of the background electrolyte due to the difference of kinetic barriers for growth and nucleation (Kowacz and Putnis (2008)). Positively hydrated ions predominantly increase nucleation rates and negatively hydrated ions mainly increase particle growth at increasing supersaturation (Matynia et al. (2004)).

That the kinetic barrier can be dominated by water exchange kinetics, is further substantiated by experimental observations of increased nucleation rates of barite in solvents with added methanol (Tomson et al. (2004b)). This addition decreases solvent structure and lowers the barrier of cation desolvation. This is in contrast with the effect of the background electrolytes on the nucleation barrier. The effects of the ionic strength on zetapotential and on the Debeye length will be discussed in Section (2.3.2)

pH control on nucleation

Physico-chemical parameters at ambient conditions that affect nucleation rates and mechanisms (Ω, I and pH) are interconnected. The effects of pH on crystal nucleation are most strongly forced by its effect on the interfacial tension during the initial stages of nucleation and the disruption of existing solvent structure by OH^- ions. There are ongoing debates about the exact value for the decrease in interfacial tension (Söhnel (1982); Fernandez-Diaz et al. (1990); Ruiz-Agudo et al. (2015)), but they agree that increasing pH lowers the interfacial tension. Conducted conductivity experiments show that pH barely affects nucleation rates between pH 3 and 9 (Figure 2.10). In strongly alkaline ($pH > 10$) and in acidic solutions ($pH < 2$) induction time decreased (Ruiz-Agudo et al. (2015)). Induction time is inversely proportional to nucleation rate. The predominance of effects at a very high/low pH, points towards an interpretation of these results akin to the effects of background electrolytes, with H^+ and OH^- modifying the solvent structure and, as previously mentioned, the kinetic barrier. Nucleation is limited by the desolvation of the hydrogen shell of the barium ion (Kowacz et al. (2007)), so the structure of water in the vicinity of barium is the most relevant for the nucleation rate. Due to electrostatic interactions, this vicinity is dominated by oppositely charged ions (Kowacz and Putnis (2008)) and is either unpopulated (low pH) or densely populated with OH^- (high pH). Additionally, the effect of H^+ and OH^- ions on the solvent structure is different. Protons in solution rapidly associate with the oxygen molecule of the solvent (water) to form H_3O^+. Due to the integration of H_3O^+ into the hydrogen bond network, the solvent structure is not significantly disturbed. This is in contrast with the local ordering of water caused by the OH^- ion. OH^- is a kosmotrope ion, which orientates the water molecules in its hydration shell due to its high charge density (Tuckerman et al. (1995)). This reorientation disturbs the local hydrogen bond network. The increase in desolvation rate, and thus nucleation rates in strongly alkaline solutions, due to the abundance of OH^-, can be

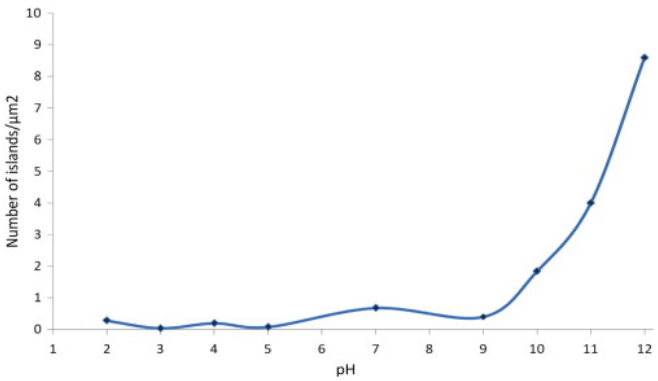

Figure 2.9: pH plotted versus island spreading rate on the [001] surface of an existing barite crystal, subsequent to growth solution injection. Measured after 250s (Ruiz-Agudo et al. (2015))

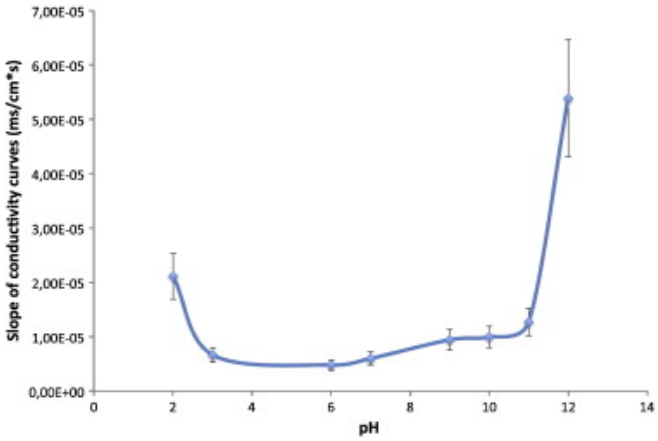

Figure 2.10: Slope in conductivity plotted versus pH. The slope is directly related to precipitation rates, increasing pH leads to increased precipitation rates (Ruiz-Agudo et al. (2015))

understood through competition for water molecules. This is analogous to competition for water molecules by background electrolyte ions (Ruiz-Agudo et al. (2015)). The mobility of water is relatively decreased around the hydroxyl ion, due to its kosmotropic character, and leads to a relative increase around Ba^{2+} and SO_4^{2-} (Ruiz-Agudo et al. (2015)). Higher exchange rate of water molecules, as discussed in Section 2.1.5, leads to a higher probability of a desolvated barium and sulphate ion colliding forming a pre-nucleus or causing ion addition to an existing nucleus (ion addition growth, CNT). This higher nucleation rate combined with lower interfacial tension at high pH leads to smaller sized critical nuclei (Ruiz-Agudo et al. (2015))

Stochiometric effects on crystal growth and formation

Deviating from a perfect stoichiometric ratio has been shown to modify growth of certain crystals (Kowacz et al. (2007) Nehrke et al. (2007)). Due to limited research into 3D-nucleation under varying stoichiometry, a potential analogue for the effects can maybe be found in crystal growth kinetics (2D-nucleation). For simple ionic compounds such as gypsum (Witkamp et al. (1990)) and calcite (Bracco et al. (2012)) the 1950's *BurtonCabreraFrank* (BCF) model holds; for a detailed explanation of what the BCF model entails see Burton et al. (1951). However, extensive limitation of this model have been documented (Teng et al. (2000); Chernov (2004)). This led to the development of more mechanistic models by Zhang and Nancollas (Zhang and Nancollas (1998)) (ZN98) and Wolthers et al. (2012) (W12). The experimental data for an AB-type crystal such as calcite (Perdikouri et al. (2009); Larsen et al. (2010); Wolthers et al. (2012) and Van Der Weijden and Van Der Weijden (2014)), barite (Kowacz et al. (2007)) gypsum,(Zhang and Nancollas (1992)) Mg- and Ca-oxalate,(Chernov et al. (2006)) and AgCl (Davies and Jones (1949)), show an optimum in growth rate at or near an activity ratio of 1. This was accounted for by the ZN98 model, but further research revealed multiple observations that could not be explained by ZN98 (Larsen et al. (2010)). This led to the creation of W12 (Wolthers et al. (2012)), which, besides accounting for step-by-step addition of either A or B ions, incorporated the idea of surface speciation and pH dependency of attachment and detachment kinetics of potential growth units. It was created through a synthesis of the surface structure model, referred to as Wolthers 2008 (Wolthers et al. (2008)) and the ZN98 model. The W12 is one of the current state of the art model for crystal growth

under different stoichiometric circumstances and its validity and effectiveness for nucleation will be evaluated. For barite, non-stoichiometric solutions, with excess barite ($r_{aq} > 1$) show an increase in 2D-nucleation and kinkstep attachment rate (Kowacz et al. (2007)). This rate increase is likely related to the aforementioned kinetic limitation (Section 2.1.5) on nucleation due to the desolvation of barium ions and is supported by the fact that addition of 5% methanol increases barite growth rates (Tomson et al. (2004b)). Barite growth rates were enhanced by this addition, presumably due to improved desolvation kinetics. One should however be careful when comparing the impact of solution stoichiometry on crystal growth kinetics with the impact on crystal nucleation kinetics. Growth kinetics are strongly affected by surface kink density, 2D-nucleation, surface charge effects, destructive step-edge interaction and specific equilibrium conditions on the crystal surface. This is different for incumbent nucleation, with a nascent surface. 2D-nucleation under non-stochiometric conditions does not provide a suitable analog, due to the strong influence of the surface on the electro-chemical parameters in its vicinity. This further illuminates a gap in our knowledge, as research into the stoichiometric effects on 3D-nucleation is limited.

2.1.6 Desolvation and growth

Crystals grow along distinct axes and on distinct faces. These are illustrated in Figure 2.11. Barite crystals generally have a tabular {001} side ranging from thin to thick. This face is bound by {210} and sometimes {101}, {011}, {010} and {100}. The growth might vary with varying stoichiometry due to desolvation kinetics

The anion tends to traverse the diffuse double layer more easily than the cation (Nielsen (1984); Piana et al. (2006)) The activation energy of surface adsorption of barium is higher than of sulfate (Piana et al. (2007)), making barium desolvation a possible rate limiting step. The water exchange frequency around barium can be aided by the presence of anions by their destabilizing effect on the water structure. At the (010) surface, the desolvation of barium is aided by the presence of sulphate in some experiments (e.g. Piana et al. (2006)), this lowers the activation energy and increases barium attachment frequency. The energy barrier of 10-20 kJ mol[1] remains at the (100) and (210) surface. Molecular dynamics studies suggest that at step edges, regardless of the crystal face, the desolvation of barium is aided by the presence of sulphate (Stack et al. (2012)). The energy barrier for attaching a barium ion to the sulphate ion present at the step edge is relatively low, the attachment seems to be limited by the bond created with the second sulphate ion present at the surface.

Research by Koskamp et al. (2019) suggests that in calcium growth, the dehydration of the cation (Ca^{2+}) is not rate limiting, contrary to earlier research by Nielsen (1984). This research was not performed directly for barite growth but indicates that more uncertainty exists regarding the desolvation of the cation as the rate limiting step then previously thought. There is also an inherent assumption to the conclusion that desolvation of an ion is the rate limiting step. Mainly that the ions arrive simultaneous at the crystal surface (Zhang and Nancollas (1998)). Research does however suggest that surface diffusion can be more significant (Hellevang et al. (2016)). Their statistical model indicated that barite has a low probability of ion complexation. Ion complexation ensures that ions arrive simultaneously and are transported across the surface more easily because they are neutral. This low level of complexation is most likely due to the low electro-negativity of the barium ion (Kresse et al. (2000)). Consequently, it is not completely clear if barium desolvation is actually limiting as the process might be limited by surface diffusion.

If surface diffusion is limiting, Hopper crystal structures might be encountered (García-Ruiz and Otálora (2015)). This means that the desolvation of barium is most likely not the limiting

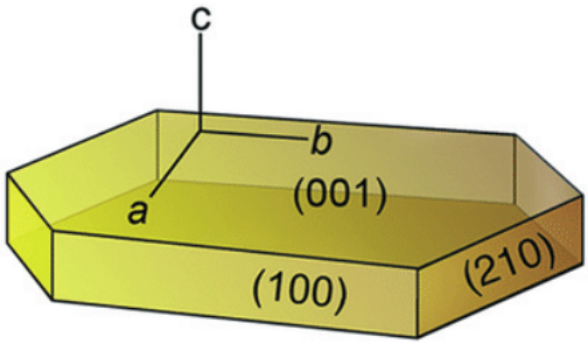

Figure 2.11: The crystallogrpahic indices of a schematic barite crystal with the separate crystal planes indicated. From Sosa et al. (2019).

step. Crystal twinning could also occur as a crystal lattice changes due to the substitution of ions. At very extreme stoichiometries (e.g. $r_{aq} = 0.01$ and $r_{aq} = 100$), intuitively we expect a higher chance of inclusion of non-fitting ions such as Na^+ and NO_3^-. This would occur due to a shortage of respectively Ba^{2+} or SO_4^{2-}. When these ions are replaced at a later moment in time, twinning can occur at this surface due to the possible deformation (Klassen-Neklyudova (2012)).

2.2 Theoretical principles of measuring techniques

The primary measuring technique utilized for this study was DLS to determine particle size and development. Complementary SEM and SAXS experiments were performed. In this chapter, first, the principles of DLS are elucidated, for its application in particle size measurements and zeta potential. This is done through an introduction into particle movement, light scattering and model independent and dependent results. Subsequently the principles of SAXS and SEM are explained.

Brownian motion

The basis of DLS is utilizing intensity variation due to Brownian motion to calculate the size of individual particles. Brownian motion is the erratic movement of particles caused by constant, random collision with solvent molecules and their inherent thermodynamic movement above absolute zero (Karatzas and Shreve (1998)). Collisions with solvent molecules cause a transfer of kinetic energy and constantly change the velocity and direction of particles in solution. Smaller particles are more strongly affected by these collisions due to lower inertia than their larger counterparts (Karatzas and Shreve (1998)). The velocity of particles due to Brownian motion is defined as the translational diffusion coefficient (D_{trans}). The translation from translational diffusion coefficient directly to particle size is not possible. The hydrodynamic diameter of the equivalent sphere of the particle can however be calculated through the use of the Stokes-Einstein equation (Einstein et al. (1905))

$$d(H) = \frac{K_b T}{3\pi\eta D_{trans}} \tag{2.10}$$

where $d(H)$ is the hydrodynamic diameter $[m]$, Kb is Boltzmann's constant $[m^2\ kg\ s^{-2}\ K^{-1}]$, T is the absolute temperature in Kelvin $[K]$, η is the viscosity of the dispersant $[kg\ s^{-1}\ m^{-1}]$ and D_{trans} is the translational diffusion coefficient $[m^2\ s^{-1}]$

To accurately calculate the hydrodynamic diameter, it is essential that the temperature and viscosity of the system are known at the time of measurement and stay constant as these parameters directly affect the movement of the particles in the solvent. Changes in the temperature will affect the resulting hydrodynamic diameter in three distinct ways: firstly, affecting D_{trans} by creating internal convection currents, introducing non-Brownian motion into the system; secondly by affecting D_{trans} by changing the viscosity of the solvent and thirdly by directly affecting d(H) as it is a separate parameter in the Stokes-Einstein equation (Equation 2.10).

Hydrodynamic diameter

The result of the Stokes-Einstein (Equation 2.10) should be understood as the way the particle diffuses within the solvent. The diameter calculated is that of an equivalent sphere with the same translational diffusion coefficient as that of the measured particle. Besides the size of the particle, D_{trans} is influenced by all factors that influence the diffusion speed, such as ionic strength and surface structure. Additionally, there is an inherent problem measuring the size of non-spherical particles and will be further expanded on in Section 2.2 (Non-Spherical) (Hackley and Clogston (2007)).

Modification by Ionic strength The particle diffusion velocity is partly influenced by the thickness of the electric double layer (Debye length) of any particle in solution. The thickness of this layer is modified by the ionic strength of the medium, as high ionic strength restricts the size of this layer (through high concentrations or higher valence of counterions), increasing the diffusion velocity, while at low ionic strengths, the diffusive speed is retarded by an extended double layer. If measurements are conducted at a higher ionic strength, the results will be closer to the size of the crystal nucleus (Hosse and Wilkinson (2001)).

Non-Spherical particles The size of any non-spherical particle measured will be equal to that of the size of the hydrodynamic diameter of a spherical particle with the same translational diffusive speed. The only measurable changes in size of a non-spherical particle are the increases or decreases in size that affect the translational diffusive speed. Addition of building units to a rod-shaped particle will for example only be visible in the length axis, whereas increases in the rod's diameter will not modify the diffusive speed to any noticeable effect (Pecora (2000)).

2.2.1 Light scattering

Light scatters differently depending on the ratio between the laser wavelength and the particle size. It can be subdivided into 3 categories: Rayleigh scattering, Mie scattering and geometric/optical scattering. At particle sizes much smaller than the wavelength ($a << 1$), the light scatters according to Rayleigh scattering, at $a \approx 1$, Mie scattering occurs and with particles much larger than the wavelength, geometric scattering is sufficient to describe the scattering patterns (Bhattacharjee (2016)), the exact reasoning behind this falls outside the scope of this work, but excellent and detailed descriptions are available (Yguerabide and Yguerabide (1998); Uemura et al. (1978)). a is defined as:

$$a = \frac{2\pi r}{\lambda} \tag{2.11}$$

where $2\pi r$ is the circumference of a circle $[m]$ and λ the laser wavelength $[m]$

Rayleigh and Mie scattering are parametric processes and thus non-invasive (Reintjes (2012)). Both these scattering regimes are considered to be elastic scattering processes. In elastic scattering, the energy of the wave does not substantially change and thus the wavelength and frequency stay the same (Hübschen et al. (2016)). The scattering results from the electric polarizability of the nanoparticle, the oscillation of the electric field of the wave causes the charges of the particle to move at the same frequency. This transforms the particle into a radiating dipole, whose radiation can be measured (Murthy (2013)). At particle sizes approximately up to $\lambda/10$, light scatters indiscriminately, from an experimental point of view, and its intensity follows the Rayleigh approximation (2.12) (Murthy (2013); Seinfeld and Pandis (2016))

$$I = Io\frac{(1 + cos^2(\Theta)}{(2R^2)} * \frac{2\pi}{\lambda}^4 * \frac{(n^2 - 1)}{(n^2 + 2)}^2 * \frac{d}{2}^6 \tag{2.12}$$

Where I is the intensity of scattered light $[W/m^2]$, I_0 is the intensity of the unpolarized laser $[W/m^2]$, Θ is the scattering angle, R is the distance of the light source to the intersection of the scattering object [m], λ is the wavelength of the laser [m], n the contrast in refractive index between the particle and the medium ($\frac{n_{par}}{n_{sol}}$) and d is the particle diameter [m]. In Rayleigh scattering, light scatters almost equally in all directions (Hallett (1999)). At 90°, the scattering is $\frac{1}{2}$ that of the forward and backward direction due to the $cos^2(\Theta)$ angle dependency in the first term of Equation 2.12.

Following from Equation (2.12), a six orders of magnitude dependency of intensity on the particle diameter becomes apparent (d^6). A tenfold increase in particle size results in a million-fold increase in light intensity. This imposes limitations on the measurement possibilities of DLS (Section 2.3.2). The relationship between intensity and particle diameter in Equation 2.12 is additionally used when calculating the number of particles from the amount of scattered light by the particle populations of a specific size (Section 2.3 and 2.12). Using the Maxwell's equations, the relative volume and number of particles can be calculated. Assuming two particles that differ in size by one order of magnitude, the larger particle will have a thousand times the volume and its intensity will by a million times bigger compared to the smaller particle (Figure 2.12).

Mie Scattering occurs as the diameter of the particle approaches the wavelength of the incoming light (Deshler (2015)). For DLS purposes, it relates the volume of a particle to intensity according to the Maxwell's electromagnetic field equation (Born and Wolf (2013)). The essential difference between Rayleigh and Mie scattering arises from the fact that Mie scattering has a strong preferential forward scattering direction (Deshler (2015)) (Figure 2.13). The scattering intensity of all particles within the measurement range is predicted under a set of assumptions (Hulst and van de Hulst (1981)). These assumptions are that all particles are spherical, light is only scattered once, the optical properties of both the particles and the medium is known and constant and the particles are completely homogeneous. The difference between refractive index of the particles and the surrounding medium is used to calculate the intensity of scattered light. This theory is also utilized to predict how the absorption affects the transmitted light and the quantify absorption versus refraction. The translational diffusive coefficient (the raw data) is measured irrespective of the difference in refractive index. It becomes relevant during the translation to particle size. (Kuipers (2020b)).

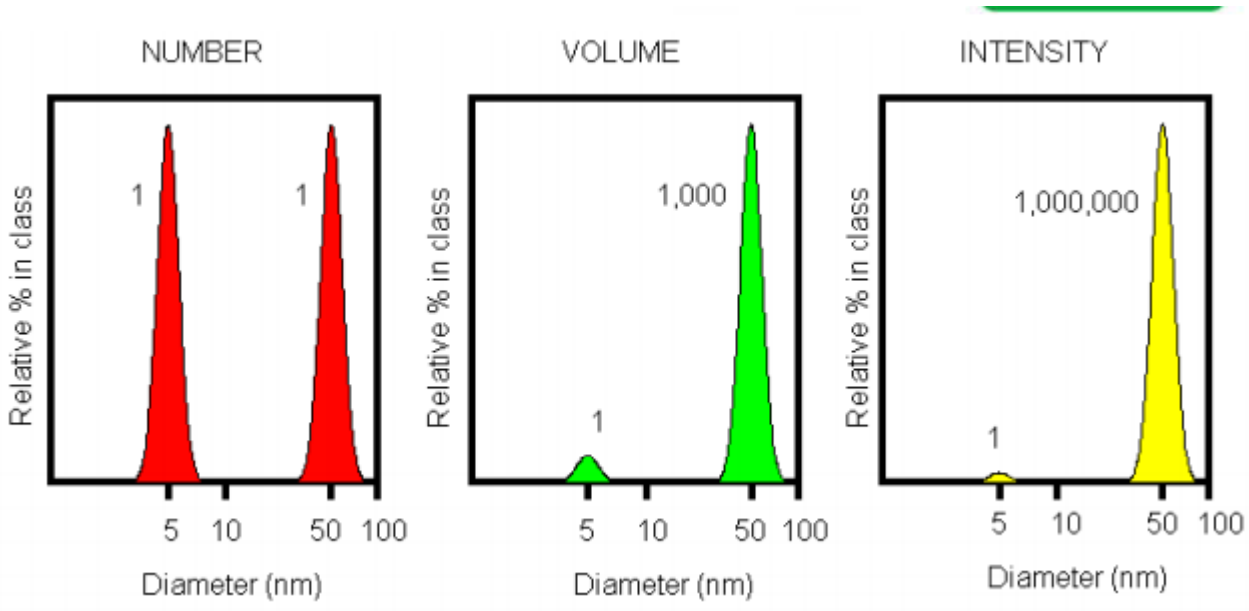

Figure 2.12: Transformation of intensity to number of particles over diameter of a bimodal mixture of 5 and 50 nm lattices present in equal numbers. Clearly displaying the power of 6 and power of 3 dependency of respectively intensity and volume (Source: Adapted from Dynamic light scattering: an introduction in 30 minutes by M. Instruments, 2012)

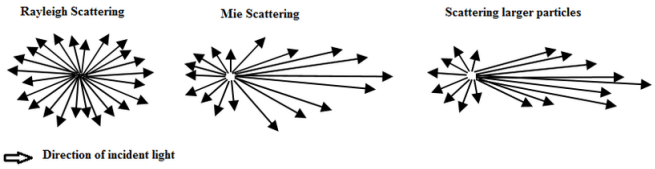

Figure 2.13: Schematic overview Rayleigh, Mie and geometric light scattering. Note the preferential forward scattering of the larger particles compared to the smallest particle, adapted from Alkholidi (2014). A cosinus term in the Mie

The impact of choice of scattering angle

In theory, the scattered light can be measured under any angle. Resulting in the measurement of variation in scattering intensity with measurement angle such as illustrated in Figure 2.13. Many technical solutions rely on a combination of small angle, forward scattering, side scattering and large angle back scattering. In principle, these angles should yield the same results but some distinct differences in their results exist. These differences arise from changes in measured volume and angle of the scattered light (Kuipers (2020b)). The assumption made in the Mie theory, that each photon is only scattered once needs to be true to make any inferences on particle size. It follows logically that, in order to minimize multiple scattering events, it can be beneficial to decrease the volume through which the laser travels in a concentrated sample. This can be achieved by the application of Non-Invasive BackScatter (NIBS). In NIBS, the focus of the laser can be adjusted to either increase or decrease the volume traversed, depending on the concentration of particles and turbidity of the sample. Relying on NIBS comes with additional advantages, mainly, that larger particles scatter more strongly in the forward direction. This means that noise coming from possible contaminants such as dust and the scattering by larger populations in a polydisperse sample preferentially scatter in the forward direction, consequently very small

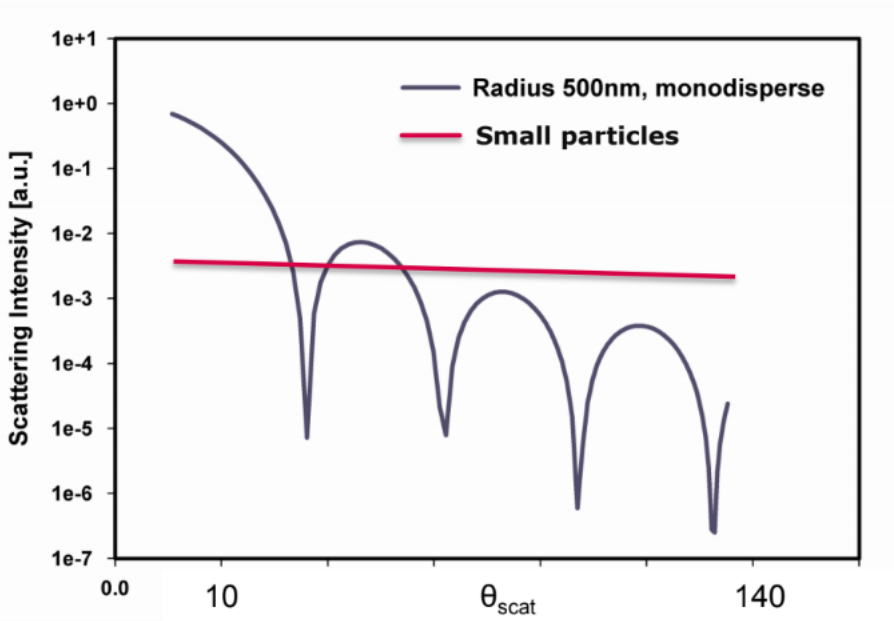

Figure 2.14: Scattering intensity of particles of a specific size over scattering angle. Note how the small particle does not have a strong preferential scattering direction, akin to Figure 2.13. The angle dependency of larger particles becomes clear, with local minima and maxima (Kuipers (2020b))

particles can be measured, even in the presence of larger particles, using NIBS. However, reducing secondary scattering events can lead to significant influence from lens flare. Lens flare is caused by the scattering of photons by the cuvette wall. This decreases the signal to noise ratio, especially for weakly scattering samples. For samples with low concentrations or very small particles, traditional side-scatter circumvents the lens flare problem. Sidescatter suffers from smaller scattering volume and consequently has more particle size fluctuation at higher concentrations. With a strongly disperse sample, forward scattering provides a solution. Due to the longer path length, increased secondary scattering becomes a greater concern, but it increases the chance of measuring individual larger aggregates or larger particles that are of concern. The angular dependence on the scattering behaviour of certain particles means that the same solution can produce different size distributions under different measurement angles. Preliminary knowledge of expected particle sizes is thus very beneficial as the correct scattering angle can be chosen to highlight desired parts of a polydisperse sample.

Multi-Angle Dynamic Light Scattering provides the possibility to create a completely angular-independent particle size measurement. It aims to provide a complete picture of all populations present in the sample by combining measurements at multiple measuring angles. This ensures that particles that scatter weakly in one direction (large particles in backscatter for example (Figure 2.14)) are measured in a different angle, forwardscatter in this example. PSD is derived from multiple autocorrelation functions of individual detection angles. These are treated as simultaneous, parallel functions and a single PSD, accounting for all different measuring angles (Cummins and Staples (1987); Bryant and Thomas (1995)).

$$\begin{pmatrix} g_1(\Theta_1,\tau) \\ g_1(\Theta_2,\tau) \\ g_1(\Theta_3,\tau) \end{pmatrix} = \begin{pmatrix} K(\Theta_1,\tau,d)x(d) \\ K(\Theta_2,\tau,d)x(d) \\ K(\Theta_3,\tau,d)x(d) \end{pmatrix} x(d) \tag{2.13}$$

where Θ signifies the different scattering angles. Solving this equation is not straightforward, as inherent weighting of PSD for each separate measuring angle needs to be accounted for. This is achieved through multiple steps: Firstly, weighting, using the computed scattering intensity, is applied through the Mie function. Secondly. from the concatenated autocorrelation function, the residual is calculated between the predicted autocorrelation function and the measured function and is minimized through application of least squares (similar to single angle measurements). Lastly the PSD is extracted. The separate angular contributions to the residuals are calculated in order to account for different degrees of uncertainty at different measurement angles. This process produces a result which can be, in essence, seen as a angular-independent measurement. In order to apply the Mie Theory, optical properties of the dispersant and measured material need to be known. Approximations can be made through Fraunhofer Diffraction Theory (de Boer et al. (1987)) if the material is unknown, very diverse or has different scattering angles on different faces (Weiner (1971)). MADLS becomes specifically relevant if populations are larger than 50 nm. In this size-range, particles can scatter non-isotropically, resulting in different size measurements at different measurement angles. However, even in isotropically scattering size ranges, improvements in data quality (for some applications), through use of MADLS, can be theoretically substantiated. The multi-variate information constrains the solution so that only common components (signal), represented in all autocorrelation functions, are incorperated in the result, while single measurements get rejected (noise). This improves the signal to noise ratio. This is specifically useful for low concentration, non-disperse samples. The true improvement compared to single angle measurements comes however, from the possibility to analyse mixtures in which particles scatter at different intensities under different detection angles and the improved statistics of the results. A clear drawback is the loss of information on very large particles that are only recorded in the forward scattering angle.

2.3 Size information

2.3.1 The correlation function

Information about particle size is extracted from the correlation function. This function is an exponential decay, which is a measure of similarity between random variables. For the DLS, the correlation function is used to describe the intensity change of the scattered light for a chosen time domain. In that time domain, it is used to establish coherence between fluctuating signals. It has been mathematically defined as the following equation (Kuipers (2020a))

$$G^{int}(\tau) \equiv \langle I(t)I(t+\tau)\rangle \tag{2.14}$$

When sampling at discrete time intervals τ and $n_i \propto I(t)$ the equation becomes

$$G_2(j \cdot \Delta\tau) = \lim_{N\to\infty} \frac{1}{N} \sum_{i=1}^{N} n_i \cdot n_{i-j} \tag{2.15}$$

where i is the sample time period and j the memory channel. This means that n_i is the intensity at a specific time step and n_{i-j} is the intensity of previous time steps. This calculation is performed for a large variety of τ simultaneously. Shorter time shifts are used for the high range of exponential decay whereas longer time shifts provide high resolution information on the lower part of the decay. This decay can be mathematically described (Kuipers (2020c)):

$$G^{int} =' contrast' e^{2D_{trans}k^2\tau} \tag{2.16}$$

with the magnitude of the scattering vector being defined as q by:

$$q = \frac{4\pi n_{medium}}{\lambda_{vac}} \sin \frac{\Theta_{scat}}{2} \tag{2.17}$$

where n_{medium} is the refractive index of the medium, λ_{vac} is the wavelength of the laser and 'q' the reciprocal vector length.

'Contrast' refers to the intercept with the normalized y-axis of the autocorrelation function Figure 2.15. Running parallel memory channels, where the autocorrelation function is calculated over a large range of τ, providing the possibility to simultaneously measure small and large particles. The x-axis of the correlation function (τ) is plotted on a logarithmic scale to display large spread in τ and the y-axis is normalized to ≈1, by division with average intensity $\langle I(t)\rangle^2$ (base line value). This normalization leads to (Kuipers (2020a)):

$$G_2(\tau) = \langle I(t)\rangle^2 \cdot C_0 e^{-2D_t k^2 \tau} + \langle I(t)\rangle^2 \tag{2.18}$$

where C_0 is the contrast factor and as $\tau \Rightarrow \infty$,

$$G_2(\infty) = \langle I(t)\rangle^2$$

and as $\tau \Rightarrow 0$,

$$G_2(0) = \langle I(t)^2\rangle$$

From statistical mechanics, it can be deduced that

$$\langle I(t)^2\rangle = 2 \cdot \langle I(t)\rangle^2$$

Examining the autocorrelation function is of vital importance, since it can illuminate many potential errors in the measurement. If the 'contrast' (C_0) of the function is below 0.8, the result of the low amplitude of the intensity fluctuation, the data should be examined critically for one of the following problems: Bad optics (a badly focussed laser), bad signal-to-noise ratio (low particle concentrations are low degree of scattering), multiple scattering events or heterodyne detection.

Problems in the optics can not be solved internally, but require professional repairs. Bad signal-to-noise ratio can also be the origin of low contrast and can be improved by either increasing the concentration of the sample, increasing the difference between the refractive index between the particle and the solvent (by changing the solvent) or increasing the number of sub-runs for the measurement. Multiple scattering events can be detected by creating a concentration range and see if the apparent particle size decreases with increasing concentrations. If this is the case, a simple dilution of the sample will improve the measurement dramatically. Additionally, a different solvent can be chosen with a refractive index closer to the target particles. Heterodyne detection means that not all measured particles are moving and a different definition of the decay function needs to be employed, particles could, for example, attach to the cuvette wall, interfering with the laser. In this modified decay function, the multiplication by 2 is removed in the $e^{-D_t k^2 \tau}$-term, compared to the original function (2.18) to account for only half of the particles moving.

$$G_2(\tau) = \langle I(t)\rangle^2 \cdot C_0 e^{-D_t k^2 \tau} + \langle I(t)\rangle^2 \tag{2.19}$$

Additional understanding can be gained from the shape of the autcorrelation function, irrespective of C_0. A superimposed sinusoidal on the autocorrelation function indicates a measure of lateral movement in the sample. For known flow conditions, this can be mathematically subtracted to a certain level. In batch measurement however, it is an indicator for thermal convection. Thermal convection occurs when the laser heats up the particles or the solvent. Larger particles are measured on longer timescales and deviations from the expected autocorrelation function at very large τ are evidence of sedimentation in the sample. Both can be seen in Figure 2.15

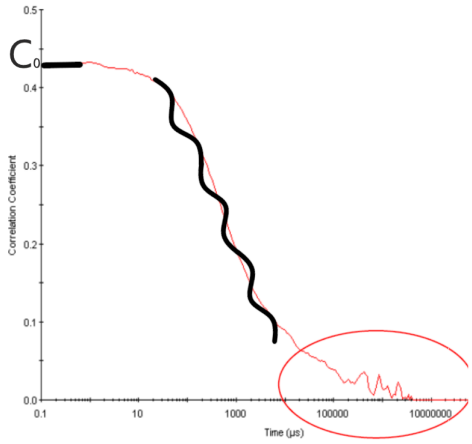

Figure 2.15: Example of the effects of linear velocity and sedimentation on the shape of the autocorrelation function. Additionally, the contrast factor (C_0) is indicated (Kuipers (2020a))

2.3.2 Size information, polydisperse samples and model-independent analysis

To deduce size information from the correlation function, multiple model dependent and independent approaches are available. The model dependent solutions are much simpler, but have fallen out of favour (Kuipers (2020c)). The cumulants analysis is the most basic method of analysing a correlation function. It consists of fitting a single exponential to the correlation function, yielding the average diameter and providing an estimate width of the distribution (PDI). As the Taylor expansion underlying this method is only valid for mono-disperse samples, it is not applicable. The model independent inversion methods, namely, Contin (Provencher (1982)), General Purpose, Multiple Narrow Modes (MNM) (Kuipers (2020c)) will be discussed. Plots generated from these methods are intensity over particle size. To achieve this, the sphere approximation is made. This facilitates the transfer from translational diffusion coefficient to particle size.

The example autocorrelation function (Figure 2.15) is of a monodisperse sample. For polydisperse samples however, multiple exponential decay function are fused. Its scattering intensity cannot be described in the same way as for a monodisperse sample but by (Kuipers (2020c)):

$$I_{scat}(q) = \int_0^\infty I(q,r)N(r)dr \tag{2.20}$$

where $I(q,r)$ is the weight factor and $N(r)$ the particle size distribution. To solve this problem, an approximation is made:

$$I_{scat}(q_m) = const \sum_{j=1}^{N} I(q_m, r_j)n_j \tag{2.21}$$

with $m = 1, ...M$ (M being the scattering angles) for N radii and r is the radius. This is very similar to the monodisperse system, except a weight factor is added to each individual population. Contin, General Purpose and Multiple Narrow Method all employ Non-Negative Least Squares method (NNLS) (Lawson and Hanson (1995)), but employ different degrees of regularization. Regularization is an additional term in the NNLS, which smooths the function. It is useful to filter random noise peaks and creates a Gaussian distribution of particles. In a monomodal system, the difference between higher or lower degrees of regularization is limited but in multimodal systems, as is expected in our research, the difference can be determining for the interpretation. A higher degree

of smoothing (General Purpose) will group different populations under the same size distribution peak, whereas a lower degree of regularization, Contin or MNM will display separate populations. The latter are however more prone to noise.

DLS limitations

DLS measurement devices have multiple limitations on absolute size that can be measured and the polydispersity of measured particles. It is essential that all particle motion is the sole result of Brownian motion in order to obtain accurate measurements. If a particle settles is dependent on the Stokes law and the Brownian motion, and thus density and temperature dependent. Very small particles $< 0.1\mu m$ almost never settle (Haranas et al. (2012)), unless they are extremely dense. When particles start to settle is not completely clear, but up to particle sizes of $1 * 10^3 nm$, the measurements are relatively unaffected Ruseva et al. (2018)). The size of any settling particle is automatically underestimated due to its increased velocity. Larger particles can also overexpose the sensor to light, which makes measurements impossible (Equation 2.12). By attenuating the laser, it is possible to overcome this issue to a certain extent. This option has the definitive drawback of completely obscuring the smaller particles. The lower limit of DLS is defined by the signal-to-noise ratio. As particles become excessively small, the intensity of Rayleigh scatter, due to their presence becomes so small that it is indistinguishable from background noise ($\approx 1nm$). This is observed during the measurement if photon countrates of 10 kcps or less are measured. 10.000 photons per second are expected to reach the sensor, unrelated to scattering by the sample (Kuipers (2020c)). Meaning, samples which do not scatter sufficiently to reach ≈20kcps can not be accurately measured due to a low signal to noise ratio (Kuipers (2020c)). Additionally, a large spread of particle sizes also has an inherent problem, as the intensity of scattered light has a power 6 dependency on particle size (Equation 2.12), consequently large particles can obscure the signal of smaller particles, limiting the applicability to systems with many populations. DLS is a statistical method, each extractable measurement consists of many sub-measurements. Any sub-run which is not repeated is removed automatically, resulting in only statistically valid measurements. Consequently, particles which are very rare and are only measured once or twice are not represented in the final measurement. Due to recent computing improvements, DLS equipment has significantly improved run retention. For trustworthy results, this retention should be between 80 and 100 %.

Zeta Potential

In essence, zetapotential (ZP) (electrokinetic potential) reflects the effectiveness of the double layer to counteract the surface charge density (Hunter (2013)). Counterions accumulate close to the particle (Stern Layer), whereas co-ions are depleted in the particle vicinity, following the Boltzmann distribution. The ZP is dependent on surface and dispersant properties and is essential for understanding the stability of systems, regarding flocculation, coagulation and colloidal particles (Hunter (1993)). Due to brownian motion (Section 2.2), particles randomly approach other particles, this leads to attractive Van der Waals forces (Klimchitskaya and Mostepanenko (2015)) and a potential electric double layer repulsive force (Gruen and Marčelja (1983)). The strength of the repulsive force of the diffusive double layer is either sufficient to prevent flocculation and the particles stay in suspension as small particles or sufficient force is applied and the particles stick together (Albers and Overbeek (1959); Letterman et al. (1999)). This leads to increasingly large particles, potentially undergoing sedimentation or creaming, depending on their relative density

to the dispersant (Albers and Overbeek (1959)). Under low ionic strength conditions, this coagulation is relatively permanent. When ZP is surpressed however, an energy minimum occurs which leads to unstable flocs. Brownian motion does not suffice to deflocculate the system, but external agitation of the system will break these flocs up. The repulsive force is proportional to the square of the zetapotential, electrostratic stability is thus greatly enhanced or decreased by incremental changes in zetapotential. Repulsive force V_R is calculated through the following equation (Fairhurst (2012)).

$$V_R = D * a * \xi^2 e^{-KH} \tag{2.22}$$

Where D is a constant related to the dielectric constant of the material [F/m], a is the radius of the particle [m], ξ the surface potential of the particle [V], K is the conductivity of the medium [w/K], H is a measure of separation betweeen particle surfaces [m]. K (conductivity) is proportional to ionic strength. It follows from Equation 2.22 that at very high ionic strengths ($I \to \infty$), the effects of the ZP are completely suppressed.

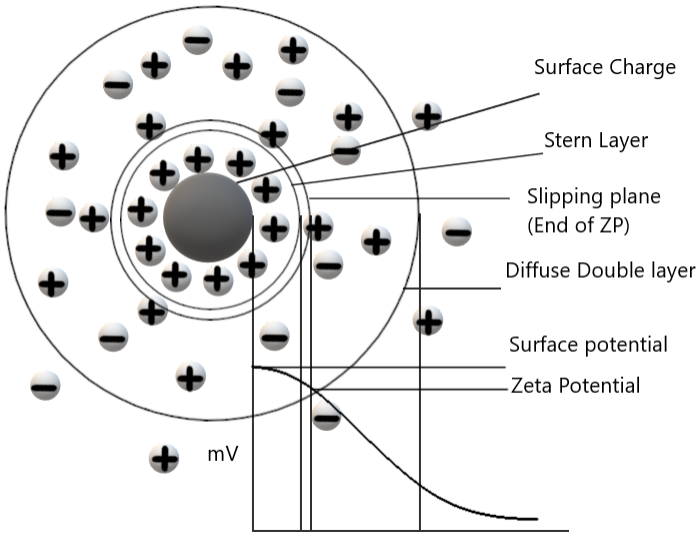

Figure 2.16: Schematic representation of the different layers around a ion in solution, the slippin plane indicates the boundary between ZP and the larger diffusive double layer. Additionally the energy curve [mV] over distance from the particle surface is displayed.

ZP is different from the potential at the outside (solution side) of the diffusive double layer and is divided from it by a slipping plane. The ZP is the potential at the slipping plane, which can be seen as enveloping the layer close to the surface where the ions are staying with the charged particle if it were to be moved through the liquid rapidly, whereas everything outside the slipping plane (but still within the diffuse double layer) would stay behind (Lin et al. (2003)). This is illustrated in Figure 2.16. ZP is not inherent to a particle, such as thermodynamic charge. It fundamentally originates from the conditions of the surface sites, mainly quantity and type, and is strongly influenced by solution parameters (Hunter (2013)). Ionisation of surface groups, by the dissociation of acidic groups, will produce a negative surface charge. Uptake of protons by dissociated surface sites leads to a positively charged surface (Liao et al. (2009)). Besides changes within attached surface groups, differential removal or addition of ions from/to the crystal surface also results in a charged crystal lattice, as for example shown for calcite (Cicerone et al. (1992) Wolthers et al. (2008)). Pre-existing impurities or adsorped charged species can also lead to a change in the surface charge (Fuerstenau et al. (1992) Hang et al. (2007)). The pH and

the electrolyte concentration of the dispersant determine the ultimate sign and magnitude of the effective double slip layer (Hunter (2013)). A particle with a positive ZP will become neutral due to alkali addition and will become increasingly positive by acid addition. The circumstances where the zetapotential is zero, is called the isoelectric point (Salgin et al. (2012)). Particles at their isoelectric point are at a minimum in terms of solubility (Whitaker (1993)). When an electrical field is applied, these particles will remain stationary. It is useful to make the distinction from a point of zero-charge, which can, besides referencing to a balanced charge, also refer to particles with no surface charge. These particles will not have a ZP under any conditions and are not electrochemically active. Consequently, a figure for ZP, without knowledge of the exact solution conditions holds no information on the actual particle. ZP can not be measured directly, but is an inferred characteristic (Fairhurst (2012)).

The goal within this research is not to measure the zetapotential, but to understand the charge at the particle surface. This can be achieved through Graham's approximation (Equation 2.23)

$$\zeta = \frac{\xi * k^{-1}}{\epsilon} \tag{2.23}$$

where ζ is the measured Zeta potential [V], k^{-1} is the inverse debey-length $= \frac{0.304}{\sqrt{I}}$ [m] and ϵ the permitivity of the medium [F/m]

2.3.3 Theoratical basis of zeta potential measurement

Zetapotential measurements are based on electrokinetic effects, in other words, the interaction of charged particles with an electric field (Kumar and Dixit (2017)). Two interactions are relevant for understanding zetapotential measurements. Electrophoresis (Zschörnig et al. (2003)) and electro-osmosis (Li] et al. (2013)), respectively the relative movement of a charged particle compared to the surrounding liquid and the movement of a liquid relative to a stationary charged surface under an applied electric field. Due to the opposite attraction (Figure 2.17) experienced by the diffuse double layer and the particle, a good measurement cannot be taken without understanding the ratio between them. Generally, the particle is much larger than its diffuse double layer and the Smoluchowski model (Sze et al. (2003); Somasundaran (2006)) can be applied. The theoretical basis of this model is that the movement of the diffuse double layer is negligible compared to the movement of the particle. The other option is that the diffuse double layer is comparatively large. In that case, the diffuse double layer moves in the opposite direction relative to the particle under the electric field. Thereby increasing the apparent velocity of the particle, introducing an error into the ZP measurement. In that case, Hückel's model applies (Somasundaran (2006)), which takes this relative movement into account. The particles elecrophoretic velocity is described by the following relationship (Piatt (2016)):

$$\upsilon_{el} = E(\mu_{el} * \mu_{eo})D \tag{2.24}$$

where υ_{el} is the particle elecrophoretic velocity $[m^2/s]$, E is the applied electric field strength [V/m], μ_{el} is the electrophoretic mobility $[m * m/(V * s)]$ and μ_{eo} is the electro-osmotic Mobility $[s/m]$ and D is the diffusion $[m^2/s]$

For a particle with a relatively small diffusive double layer, the electroosmotic contribution to the total measured particle velocity can be considered negligible (Besra and Liu (2007); Hanaor et al. (2011)). Due to the strength of the applied field, the contribution of the diffusion of the particle is also irrelevant. Through Henry's Equation (Equation 2.25), it is possible to relate the measured velocity to ZP.

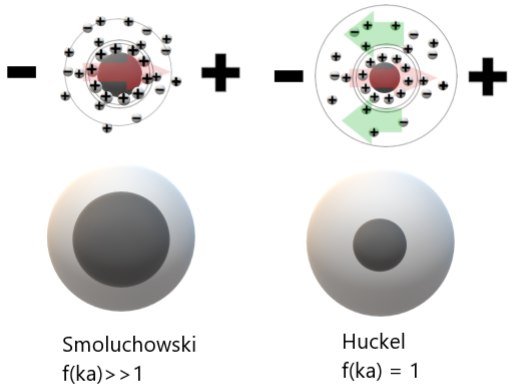

Figure 2.17: Schematic view of electrophoretic mobility, note the difference between a collapsed or expended diffuse double layer. The application of an electric field results in attraction of the particle, suspended in electrolyte. The immediate surrounding ions experience the opposite pull in case of an expanded diffuse double layer and only very limited interaction with the electric field in a collapsed double layer (Hunter (1993))

Mathematically, electrophoretic mobility is related to particle velocity in the following manner (Besra and Liu (2007); Hanaor et al. (2011))

$$\mu_{el} = \frac{2\varepsilon\zeta f(ka)}{3\eta} \tag{2.25}$$

Where ε represents the permitivity of the medium [-], ζ is the zeta potential [V], $f(ka)$ is Henry's function where k is inverse Debey length $[m^{-1}]$ & a is the particle radius [m] and η representing the viscosity of the medium $[m^2/s]$.

2.3.4 Limitations of measuring Zetapotential

Only the limitations relevant in light of nucleation experiments will be discussed here. A limitation arises from the strong dependence of zetapotential measurements on accurate knowledge of particle sizes. Strongly disperse samples or particles, which change size over the course of the measurement, are extremely difficult to measure accurately. Such samples create very broad ZP distribution curves. Polydisperse samples suffer additionally from stronger Brownian motion effects on the smaller particles, broadening the ZP distribution even more. The signal of larger particles or agglomerates will also be unproportionally large, further complicating accurate measurements of the different populations (Domingos et al. (2009); Doane et al. (2012)). The evolution of multiple populations is expected to suffer from both these problem. However, this broadening can often be counteracted to some degree by repeat measurements under different angles (Xu (2001); Xu (2008)). This provides a clearer picture of the sizes of the particle populations and which populations are present. For this to be a suitable method, it is important that the process is repeatable. Changing ionic strengths introduces another problem when measuring the ZP, as the diffusive double layer thickness will change when ionic strength changes. Due to crystal and ionic compound formation, ionic strength will decrease during the measurement. Consequently,

the diffusive double layer will expand. A potential solution is measuring at high ionic strength, so the influence of crystal formation on ionic strength is limited. Another potential problem is sedimentation of the largest particles, which reduces the size of the measured particles, even though the particles are in reality still growing. This sedimentation also negatively affects the signal-to-noise ratio and introduces additional movement into the system. It is possible to track sedimentation by tracking scattered light intensity and observing the autocorrelation function of additional DLS measurements. From thermodynamic considerations, material dissolution can often be disregarded. This means that a reduction of scattered light intensity is directly related to removal of material from the measured volume through sedimentation. The choice of model for the calculation is also not always straightforward and must be based on information regarding metal uptake/release, size distribution, agglomeration behaviour and ionic strength.

2.4 Small Angle X-ray Scattering

In many fields of science, high powered microscopes no longer suffice for the high demands in terms of resolution, low concentration measurements or specific time distribution of reactions. This development led to the emergence of highly specialised facilities, producing synchrotron radiation for experimental goals. Any electromagnetic wave passing through a material experiences some degree of scattering besides the expected absorbance. This property is utilized, comparable to the way it is in DLS, by the synchrotron. In the following chapter the principles of synchrotron radiation and a synchrotron are expounded, the relevant parameters explained and an introduction to the correction and analysis of the obtained synchrotron data is provided.

2.4.1 SAXS vs Microscopy

Microscopy is the traditional candidate to observe extremely small particles. It allows for visualisation of particles to near-atomic resolution. When considering microscopy in the context of observing continuous reactions, two problems emerge. Firstly, the sample preparation is cumbersome due to the rapidly evolving sample and creating statistically relevant data is nearly impossible, because only a small fraction of your sample can be observed at a given time. It is thus necessary to create many samples and observe different parts of them at the same time to understand the system under investigation. In the context of nucleation, this would require an enormous amount of samples, all observed at the crucial moments of nucleation. It is possible to circumvent this problem by employing a different measuring technique. With SAXS, it is possible to observe the sample through time with snap shots. The transition from the aqueous phase to the solid phase can be observed in a simple capillary cell and probed during its evolution. Another added benefit is that the photon beam probes the complete volume it transverses, significantly increasing the amount of data collected per experiment.

2.4.2 The synchrotron

A synchrotron essentially consists of six parts. An electron source, booster ring (inner-ring), storage ring (Outer ring), a radiofrequency cavities, optical hutches and experimental hutches. The inner ring increases the velocity to near light-speed levels. The electrons are subsequently transferred to the outer ring. This ring is not perfectly circular, but consists of straight sections, punctuated by bends. The electrons are, similar to other particle accelerators, kept in orbit by quadruple

and sextuple magnets. Due to the high speed of the electrons in the beam, the magnetic force term exceeds the electric term in the Lorentz force. Consequently, magnetic deflection exceeds the effects of electrostatic deflection. Due to this phenomenon, focussing the beam on the horizontal and vertical plane simultaneously becomes impossible. Placing magnets, with adequate spacing, in series solves this problem. Adjacent quadruples are subjected to Earshaw's theorem (Earnshaw (1842)), meaning that the electron can not be focussed in two direction simultaneously and the effects of the magnets would thus cancel out without spacing. Focussing the electron beam through quadruples introduces chromatic aberrations. These are corrected by the sextuples (Shenoy (2003); Balerna and Mobilio (2015); Willmott (2019)). Every bend can theoretically be connected to an optical hutch and, subsequently an experimental hutch. Radiation is released at the bends and this radiation slowly disperses electron groups and slowly but consistently, power is lost from the outer ring. Some synchrotrons circumvent this problem through the aptly named "Top-up" mode (Tanaka et al. (2006); Boland et al. (2007); Pont et al. (2014)). In this setup, batches of high speed electrons from the inner ring are injected into the outer ring at regular intervals. This gives a saw-tooth shaped fluctuation in intensity, compared to the continuous decrease in intensity which occurs in single injection mode. This relative and high constant power output provides more accurate data (Boland et al. (2007)). Nonetheless, a correction needs to be performed on the data in order to remove the saw-tooth pattern from it. The radiation produced by the electron, leaves the orbit tangentially and enters the optic hutch. This optic hutch provides the ability to tune the wavelength of the emitted energy. The emittance of electromagnetic waves causes a loss of energy from the electrons. If this loss is not compensated, it would be impossible to keep the electrons in a stable orbit within the storage ring. The electrons are accelerated by an electrical field in phase with the passage of the electrons.

2.4.3 Synchrotron radiation

Synchrotron radiation, also known as magnetobrehmsstrahlung (Ginzburg and Syrovatskii (1965)), is the aforementioned electromagnetic wave that is used to produce semi-characteristic scattering patterns. This radiation is released by the radial acceleration of relatively charged particles (e.g. electrons). When a highspeed electron is deflected by a charged surface, it loses kinetic energy which is transformed into electromagnetic radiation. Through this transformation, the law of conservation of energy is satisfied. At relativistic speeds, the produced radiation energy is folded forward into a narrow cone. When moving at low speed, electrons do not show this behaviour, instead producing emissions covering a broader angular range (emitting roughly in a cone of $cos^2\Theta$, akin to a radio antenna).

In the magnetic field of a bending magnet, electrons continuously emit radiation, and thus lose energy. To maintain relativistic velocities, energy is supplied to the electrons through radiofrequency cavities (RF cavity). This energy transfer occurs through an oscillating field. Consequently, the effect the oscillating field has on a passing electrons is intimately linked to the arrival time of the electrons. They are either unaffected, accelerated or decelerated. In this manner, electrons form neat rows of finite length, punctuated by vacuum. These electron rows are called bunches. As these bunches travel through the straight sections of the storage ring, they can be modulated by insertion devices (Shenoy (2003); Balerna and Mobilio (2015); Willmott (2019)). These insertion devices supply periodic magnetic fields to improve certain features of the beam, such as brightness or flux. There are two main types of insertion devices, a wiggler and an undulator (Motz (1951); Winick et al. (1981); Koch (2010)). The wiggler, as the name suggests, forces the electron to periodically divert from its path by producing a multipole magnetic field. The Lorentz force causes

the transverse movement. Since the wiggler, unlike the bending magnet, does not play a role in maintaining the correct trajectory of the electron, the magnetic field strength can be varied to create the desired emission peak. Additionally, it does not create a single radiation burst akin to the bending method, but a series of bursts, coinciding with the frequency of the induced wiggle. This wiggle can also be superimposed on a curve forced by a bending magnet, thereby increasing the total radial acceleration and thus the amount of synchrotron radiation. Enhancing the flux and the brilliance of the beam (Duke (2009)). An undulator follows the same principle as a wiggler, but the goal is to produce a pseudo-monochromatic beam by producing very small scale transverse oscillations. This avoids a continuous spectrum and instead creates a line spectrum (Winick et al. (1981)).

2.4.4 Scattering in the Synchrotron

X-ray radiation is described by elastic Thomson scattering (Glenzer and Redmer (2009)) and refers to the scattering of an unbound, unpolarizable particle (a free electron), whereas Rayleigh is the scattering of a polarizable entity through the creation of a dipole moment (Changizi et al. (2007)). In both Rayleigh and Thomson scattering, oscillation in electrons is induced with the same frequency as the incoming radiation Changizi et al. (2007)). This means that all electrons oscillate at the same frequency and they produce coherent waves (Schnablegger and Singh (2011)). Interference patterns between these waves carries the structural information of the particles.

Structure The aforementioned interference patterns can be constructive (in phase) or destructive (out of phase). Scattering at the atomic scale happens radially and is synchronized to the incident beam. The measured interference is thus only dependent on the location and orientation of the atoms relative to the other atoms in the structure. All distances within the sample are measured relative to the wavelength of the incident X-ray beam. The unit of measurement 'q' (the length of the scattering vector) will later (Section 2.4.8) be explained in order to remove the wavelength dependency, by putting distance in reciprocal space (1/distance) in contrast with particles, which are in real space with unites of length

2.4.5 The synchrotron detector

The detector is located behind the flight tube in the experimental hutch.

The sample also absorbs a part of the radiation (Paragraph 2.4.7 (The degree of extinction). A temperature increase due to this absorption is assumed to be negligible due to the results of the transmission correction. It is essential to correct for the degree of extinction and this needs to be individually determined for each sample. This is done by comparing the current supplied with the measurements taken by the beamstop-mounted diode. The factor between these is the transmission factor (T_{tm}). The absorption by the background electrolytes is separately quantified from the total absorption by blank measurements to follow the evolution of the absorption by formed particles. As the photon beam travels through a larger volume, it encounters more particles and thus is absorbed to a larger extent. This is corrected by normalizing to the thickness of the sample (Pauw (2013)).

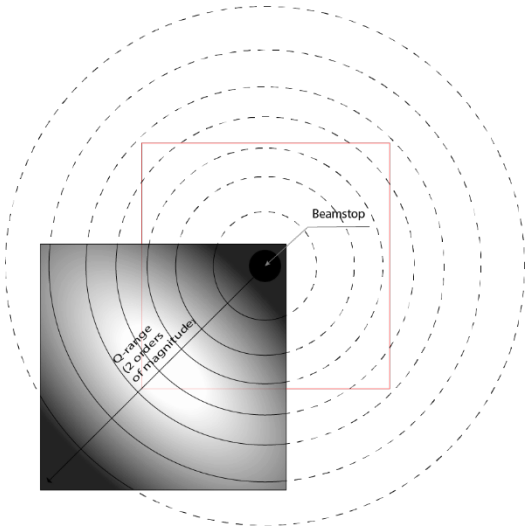

Figure 2.18: Schematic overview of the scattering pattern on the detector with the beamstop in the top right corner. The scattering pattern can be radially symmetric, meaning a larger q-range can be achieved by measuring only one quadrant. The gradient in the square is a measure of the amount of detector capacity dedicated to a specific size range. The detector has the highest accuracy for intermediate q-values.The advantages of focussing on one quadrant become self-evident, a clearly extended q-range.

2.4.6 The synchrotron detector

In order to produce countrates or intensity patterns, the production of free electrons due to oncoming x-ray radiation is used. Multiplications and amplifications turn these free electrons into electric pulses which are counted (Pauw (2011b)).

2.4.7 Inherent issues with scattering patterns and corrections

A perfect measurement is not possible. A dataset which has been perfectly postprocessed, has a hypothetical perfect background scatter pattern, with the correct uncertainties for every data point and the correct angular region, that can be subtracted. The detector is flawless in this hypothetical scenario and every experiment went perfectly. Interpreting the resulting curves is still not straightforward. Similarly to DLS, there is a loss of particle shape and problems originating from polydispersity. It is possible to retrieve this information with complementary techniques. If the particle shape is known, polydispersity can be found and *vice versa*. The perfect detector does not exist and tradeoffs are made. This introduces distortions regarding either intensity or geometry. In other words, the amount of measured intensity deviates from the real intensity or the location of the detected intensity is not accurate.

Intensity distortions Most detectors measure on a relative but proportional scale (Pauw (2011a)). The difference in measured intensity is proportional to the counted photons, but the actual photon count is not recorded. This introduces a loss of raw data which has implications for understanding errors in the data. The intensity is also distorted by the limited intensity window (Pauw (2011a)). If more or less photons than this detection limit reach the detector, they are respectively no longer accurately counted or the signal-to-noise ratio becomes exceedingly bad. Both these problems are, to some extent, alleviated by the use of a direct photon counting detector. An additional source of noise affecting any detector is the relatively constant background electronic floor noise. A control

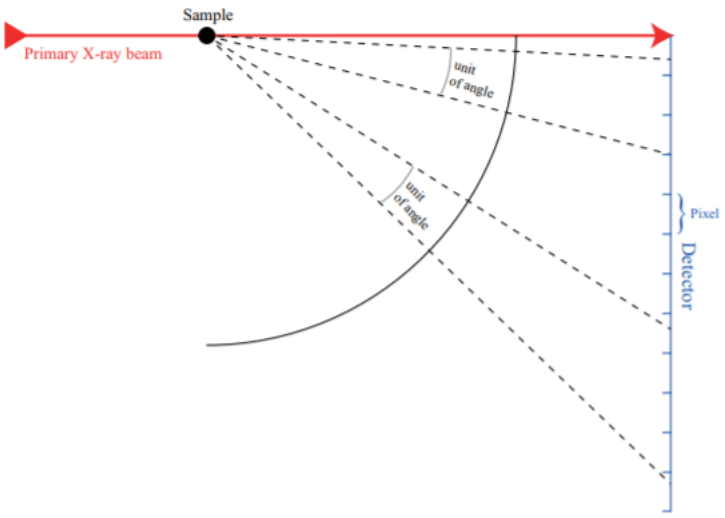

Figure 2.19: Illustration of the solid angle correction necessary for the SAXS-detector (Pauw (2011b))

on this noise is created by running a darkcurrent measurement. This entails a measurement of the detector signal without any X-rays (Barna et al. (1999)). In recent years, the development of new detectors (Eikenberry et al. (2003)) limit the aforementioned problems and state-of-the-art facilities ensure that any remaining issues are solved.

Transmission corrections Every sample absorbs a part of the radiation. This energy is transformed into an array of different forms of energy (e.g. fluorescence radiation or heat). Fluorescence radiation is the result of the dislodging of an electron by the incoming radiation, absorbing the photon and the subsequent rearranging of electrons to restore its original configuration (Lakowicz (2013)). This rearrangement releases energy in a different wavelength than the incident radiation. X-ray absorption is omnipresent, but is more efficient at the aptly named "absorption edges" (Kvick (1999)). These occur when the energy of the incoming photon approaches the energy of an electron in the outermost shell. This is dependent on the atomic species of the sample and its temperature. A calibration sample provides a solution to many of the aforementioned issues (Dreiss et al. (2006)). An intensity correction can be performed by measuring a sample from which the scattering in absolute intensities is known. This comparison yields, through a least-squares fit or linear regression, a calibration factor for the used detector and is used for subsequent measurements.

Angle corrections The detector itself is a flat surface with uniform pixels counting photons. Due to the measurement of data over a solid angle of an imagined sphere, not every pixels collects data over the same solid angle of this sphere. The amount of pixels covered by one unit angle differs depending on the distance from the point of normal incidence (Bösecke and Diat (1997)) As illustrated in Figure 2.19). A geometric correction is necessary for the different number of pixels covered by a single unit angle. (Bösecke and Diat (1997)). This and other geometric distortions has been largely solved by the PILATUS SAXS (Eikenberry et al. (2003)).

2.4.8 Reciprocal space 'q'

Scattering angle needs to be defined in an adequate way to conceptualize a synchrotron experiment and to process the data. This is done in reciprocal space, identical to DLS. SAXS data reduction is only possible with a definition of small angle scattering angle (q) that is independent of wavelength (Pauw (2011b)).

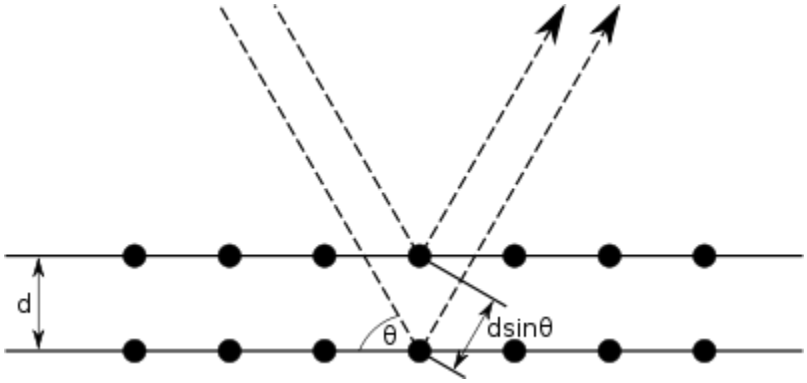

Figure 2.20: Bragg's law displaying the relationship between distance d and incoming radiation. Note that Bragg's law is using scalars, whereas X-rays should be represented by vectors

$$q = \frac{4\pi \sin \Theta}{\lambda} \tag{2.26}$$

$$\lambda = 2d \sin \Theta \tag{2.27}$$

$$q = \frac{2\pi}{d} \rightarrow \mid q \mid = \mid k_j - k_i \mid \tag{2.28}$$

It is preferable to work in reciprocal space, as this removes the assumption that that the atoms are in in parallel planes, for further reading see the Laue method (Amorós (2012)). Consequently, Θ is half the scattering angle (originating from diffraction defining the full scattering angle as 2Θ) and divided by the wavelength (λ) of the beam. This gives 'q' the unit of x^{-1}, where 'x' is the chosen length unit. The chosen 'q' is a direct result of the particle size that is targeted. This is a remnant of the fact that the SAXS detector can only measure in a limited angular region. Targeted particle size (r) needs to be decided beforehand, covering a maximum of two orders of magnitude. This can be transferred to q-space by ($q\Delta$) by (Pauw (2011b)):

$$q\Delta = \frac{\pi}{R} \tag{2.29}$$

A spherical particle with radius r gives a scattering pattern with a specific oscillation (Δq). To understand this, imagine that the target is a hypothetical particle with a size of 1 nm. The periodicity of the scattering oscillations is then $q\Delta = \frac{\pi}{1*10^{-7}}$. As previously stated, SAXS has a range of two orders of magnitude. This yields a q range of $\pi * 10^{-6} \leq q \leq \pi * 10^{-8}$. If the sample is polydisperse, 'q' should be skewed towards the larger particles (Pauw (2011a)).

2.4.9 Determining wavelength

The chosen wavelength has far reaching consequences for the quality of the data collected. The wavelength affects the penetration depth, sample to detector distance and the tolerance of collimation (Pauw (2011a)). Higher wavelengths, being lower energy, have reduced penetration depth, high detector efficiency, shorter sample-to-detector distance and higher collimation tolerance. The reduced penetration depth can be an issue, especially in samples with high concentrations or a strong absorption coefficient. In general, absorption should be less than 30% of the incoming radiation to ensure a good signal-to-noise ratio. This is the upper boundary for the chosen wavelength. The lower limit of the wavelength is often defined by limitations in detector-to-sample distance, leading to longer collimation, increasing the amount of parallel beams and thus photon loss (Pauw (2011b)).

2.4.10 Interpreting the Data

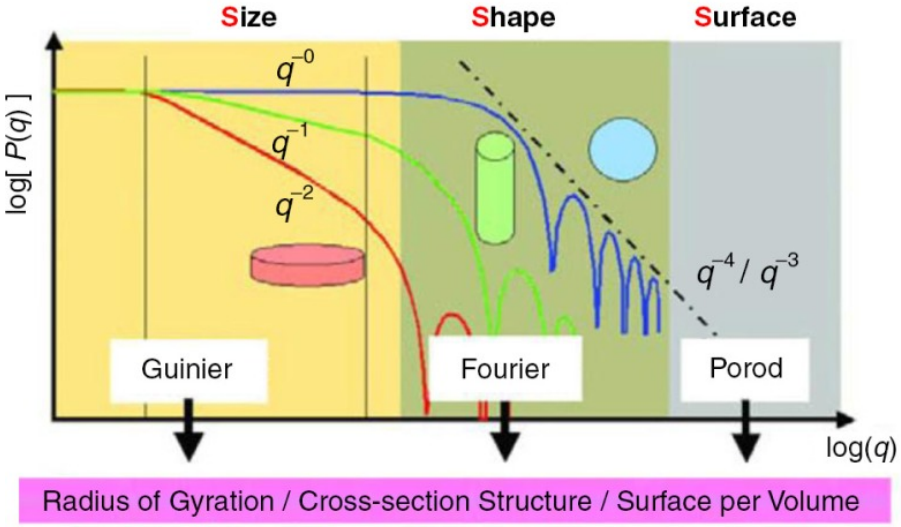

Figure 2.21: Three distinct regions of a SAXS profile with indication of the information that can be extracted, taken from (Boldon, Lauren et al 2015)

The Guinier, Fourier and Porod regions can respectively be used to extract information on the gyration radius, the form factor or particle size and on the surface to volume ratio (Figure 2.21). Within this study, a strong focus exists on the Guinier region.

When particle shape is assumed, scattering amplitude difference can be defined by the following Fourier transform:

$$A(q) = -r_0 \int \int \int_V \rho(r) exp(iqr) dV \tag{2.30}$$

where A(q) are the individual waves scattered by the electrons, r_0 is the Thompson scattering length, V is the measured volume, r is the location of the scattering centre, i is the intensity and ρ is the continuously changing electron cloud density. Note that $A(q)$ is the sum of all rays scattered by electrons, but due to the continuously changing electron cloud density, a Fourier transform needs to be applied (Pauw (2011a)). The measured intensity is equal to the squared absolute value of the amplitude A(q). This results in a square dependency of intensity on the volume of the particles in the measured volume (Pauw (2011a)).

2.4.11 Data post processing

The phase data of the Fourier transformation is lost, as only intensity is measured. The molecular mass can however be extracted from the invariant through the following generalized equation:

$$Q_{inv} = \int_0^\infty q^2 I(q) dq \tag{2.31}$$

The invariant is unchanged by the transformation and is calculated over the q-range. Further data processing was performed in a parallel Crystal Clear project (A. Baken et al., in prep.).

2.5 Scanning Electron Microscope

2.5.1 Theoretical basis

Visual information is gathered by the SEM through a focused beam of electrons interacting with a conductive layer on the sample. The interaction between the sample and the beam causes repeated random scattering (elastic and inelastic) and absorption. This leads to a large loss in energy from the original beam. This lost energy is transferred to high-energy electrons by elastic scattering (keeping the energy of the original electron beam) and to low energy electrons by inelastic scattering and electromagnetic radiation. These can all be harnessed to gather information on the sample. The most conventional technique is measuring the low-energy secondary electrons (Energy $<$ 50 eV). Due to their low energy, a focussing and accelerating stage is needed in order to excite the sensor. Interactions between angles and the incoming beam cause higher amounts of secondary electrons to escape at the edges of 3D-shapes making them appear brighter. This causes them to appear brighter than flat surfaces, creating well defined objects in a 3D-space. The probing depth of the beam depends on the energy of the incoming beam, the atomic number of the specimen and its density.

3

Materials and Method

This section is subdivided into 3 separate parts. First, the chosen salts are introduced and the theoretical calculations are explained, including the substantiation for the chosen chemical parameters. A section is dedicated to explaining the automation efforts for deriving the correct growth solution in Python. Secondly, the experimental setup and procedure is expounded. Lastly, a section is dedicated to the used method of the SEM and the Synchrotron experiments.

3.1 The salts and stock solutions

The stock solutions used to synthesise the growth solutions were produced from five different salts. Barium nitrate ($Ba(NO_3)_2$), sodium sulphate (Na_2SO_4), sodium nitrate ($NaNO_3$), Hydrochloric acid (HCl) and sodium hydroxide (NaOH) (Table 3.1; 3.1). The stock solutions were created by dissolving the appropriate amount of salt in 1 litre to create stock solutions between 0.25M and 1M which were subsequently diluted 10 and 100 times to create a range of stock solutions in order to ensure large volumes could be pipetted to increase accuracy. The stock solution were unfiltered, they were only filtered before injection into the cuvettes.

Salts	Weight dissolved (g)	Stock solution (M)	Diluted stock Solution (M)
$NaNO_3$	42.498	0.5	0.05
$Ba(NO_3)_2$	65.336	0.25	0.025
Na_2SO_4	71.023	0.5	0.05

Acid and Base	Concentration (M)	Stock solution (M)	Diluted stock Solution (M)
HCl	10.172	0.5	-
$NaOH$	4	0.5	0.010

3.1.1 Theoretical considerations

For the synthesis of growth solutions, theoretical calculations were made in Visual MINTEQ Software – a free equilibrium speciation model - version 3.1 (Gustafsson (2006)). These calculations were done to obtain the desired ionic strength, pH, saturation index and stoichiometry in a solution that could be practically achieved with stock solutions. (Table: 3.1, 3.2, 3.3 and 3.4).

r_{aq}	OH^- (mM)	Ba^{2+} (mM)	SO_4^{2-} (mM)	NO_3^- (mM)	Na^+ (mM)	pH	I	SI	Ω	$Conductivity(mS/Cm)$
0.01	0.089	0.045	3.700	195.326	202.723	7.00 (6.884)	0.1991	2.002	100.5	12.31
0.11	0.089	0.140	1.200	202.626	204.833	6.99 (6.747)	0.1999	2.008	101.9	10.38
1.00	0.089	0.408	0.408	203.716	204.746	7.00 (6.755)	0.1996	2.005	101.2	11.62
8.60	0.089	1.200	0.140	204.833	202.800	7.00 (6.755)	0.200	2.007	101.6	11.95
83.59	0.089	3.700	0.045	202.233	195.00	7.00 (6.778)	0.1987	2.003	100.7	10.22

Table 3.1: Chemical parameters of the used growth solutions for $\Omega = 100$, with the needed ion concentrations in mM. pH and electrical conductivity has been measured as a control on the growth solutions and is displayed between brackets.

$NaNO_3$ (uL)	$Ba(NO_3)_2$ (uL)	Na_2SO_4	$NaOH$ (uL)
97618	45	1850	43.5
101173	140	600	43.5
101921.5	408	204	43.5
101216.5	1200	70	43.5
97411.5	3700	22.5	43.5

Table 3.2: Used stock solution in uL to make 250mL of growth solution $\Omega = 100$. Note that not all displayed amounts can be accurately achieved through pipette and multiple dilutions of every stock solution existed for this problem. These are not displayed.

r_{aq}	OH^- (mM)	Ba^{2+} (mM)	SO_4^{2-} (mM)	NO_3^- (mM)	Na^+ (mM)	pH	I	SI	Ω	$Conductivity(mS/Cm)$
0.01	0.089	0.095	9.000	181.160	198.970	7.01 (6.761)	0.1987	2.701	502.0	10.22
0.11	0.089	0.300	2.800	199.910	205.0	7.01 (6.761)	0.2013	2.698	498.9	11.73
1.00	0.089	0.910	0.910	205.00	205.00	7.01 (6.724)	0.2018	2.697	496.6	13.27
9.93	0.089	2.850	0.290	205.300	200.0	7.01 (6.720)	0.2016	2.695	495.5	13.32
98.733	0.089	9.00	0.095	200.661	182.940	7.00 (6.746)	0.2003	2.700	501.6	10.01

Table 3.3: Chemical parameters of the used growth solutions for $\Omega = 500$, with the needed ion concentrations in mM. pH and electrical conductivity has been measured as a control on the growth solutions and is displayed between brackets.

$NaNO_3$ (uL)	$Ba(NO_3)_2$ (uL)	Na_2SO_4	$NaOH$ (uL)
90440.5	95	4500	43.5
99655	300	1400	43.5
101545	910	455	43.5
99665	2850	145	43.5
91330.5	9000	47.5	43.5

Table 3.4: Used stock solution in uL to make 250mL of growth solution $\Omega = 500$. Note that not all displayed amounts can be accurately achieved through pipette and multiple dilutions of every stock solution existed for this problem. These are not displayed.

Chemical parameters

Ionic strength All experiments were performed at an ionic strength of 0.2. This specific ionic strength was chosen due to four main arguments. The most important being to keep ionic strength constant throughout the batch experiment by limiting the effects of formation or dissolution of barite. Secondly, earlier experiments affiliated with the Crystal Clear project were also performed at this ionic strength (Sergej et al., in prep). Additionally, other earlier experiments involved with quantifying nucleation kinetics were also conducted under comparable circumstances (Ogino et al. (1987)). Thirdly, it facilitated the use of the Davies equation (Davies (1938)) to calculate ionic activity. Lastly, it suppressed the electric double layer and made the size measurements more accurate (Section 2.2).

Ionic strength is calculated through Davies equation:

$$\log(a) = A * Z_1 * Z_2 * (\frac{\sqrt{I}}{1+\sqrt{I}} - 0.30I) \tag{3.1}$$

where a is the molal activity of the coefficient of the ion [-], A is $1.82 * 10^6 * (\epsilon T)^{\frac{-3}{2}}$ $[M^{-0.5}]$, Z_1 & Z_2 are the charges of the electrolytes [-], ϵ is the relative permittivity of the medium with respect to space [-] and T is the absolute temperature [K]
The term 0.30I approaches 0 as ionic strength drops, reducing the equation to the original Debye-Hückel (Davies et al. (1962)). Limitation for this equation arose when electrolytes had charges different from +1 and -1 or when the formation of ion pairs occured. The Davies equation had a strong precedent in hydrochemistry, partly due to its wide applicability to natural systems and its mathematical simplicity (Eriksson (1985))

Atmosphere and temperature All experiments were done in contact with the atmosphere, with a constant atmospheric pressure (pCO_2) of 0.00038 atm and a temperature of 20 $°C$. As this research was performed partly to better understand surface water chemistry, these parameters where chosen, as they were easily translatable to natural systems. The exothermic effects of the barite growth process (Pina et al. (1998); Kowacz et al. (2010)) were counteracted by externally controlling the temperature with the Malvern Zetasizer Ultra.

pH The effects of pH on barite nucleation were limited by choosing pH 7 (Ruiz-Agudo et al. (2015)). pH 7 has the least effect on nucleation and structuring of the solvent by hydrogen and hydroxide ions was limited.

Obtaining the correct saturation index and proving reproducibility

The time frame of barite nucleation under the specified experimental conditions was underexamined. In order to perform sufficient experiments within the given time frame, bulk measurements (r_{aq}=1) were performed for a wide range of supersaturations, ranging from $\Omega = 30$ to $\Omega = 1000$. The aim was to find saturation indices with verifiable nucleation in 4 hours. This was done in conjuncture with additional measurements done in the lab for barite nucleation with $NaCl$ as a background electrolyte. Each of these measurements was repeated three times to qualify the stochastic nature of the nucleation process and show the reliability of the measurements. A supersaturation of $\Omega = 100$ and $\Omega = 500$ were chosen as most suitable. Additional experiments were also performed for $\Omega = 1000$ and $\Omega = 5000$ to visualize the nucleation.

3.1.2 Automation efforts

As additional research into nucleation of different minerals was expected in the Crystal Clear project. Considerable efforts were made to automatise the theoretical calculations with Python in conjuncture with Sergio Ruiz-Hernandez and Janou Koskamp (Code A). It allowed to user to input chemical boundary conditions (IS, R_aq, Ω and pH), with a allowed margin of error and it automatically calculated the ion concentrations necessary.

3.1.3 Experimental Set-up

Particle sizes were measured were done using the Zetasizer Ultra (DLS) and the chemical parameters of the batch-experiments were measured using a pH (SensoLyt 900-P) and an ec-electrode (TetraCon 925-P). Measurements with a barium electrode (DX337-Ba ISE half-cell electrode) were attempted, but it proved to be unreliable due to the background electrolyte interference with the barium electrode.

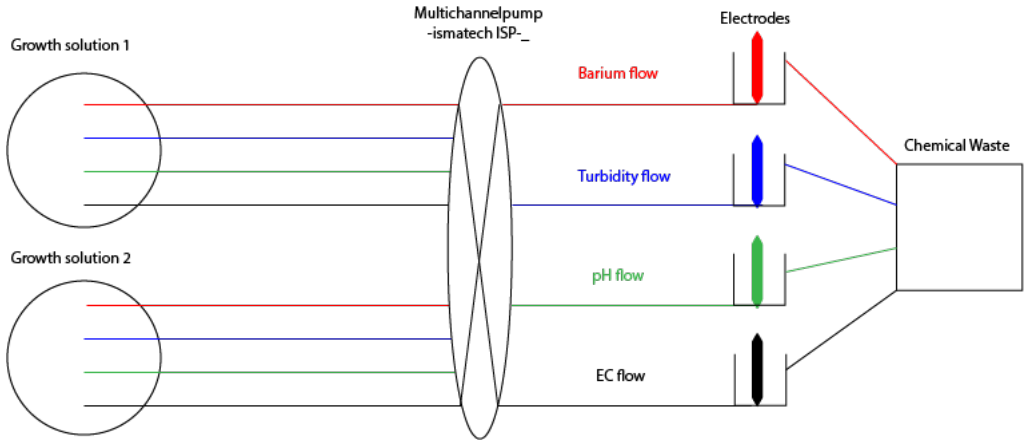

Figure 3.1: Set-up for the electrode measurements, desirable for future DLS measurements at lower ionic strength

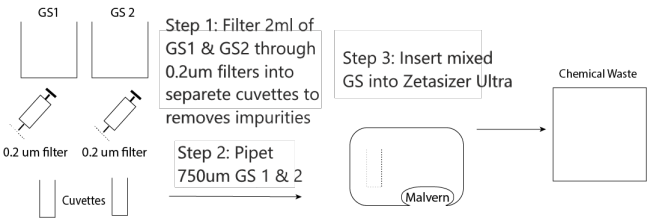

Figure 3.2: Schematic overview of the Malvern Zetasizer Ultra sample preparation workflow

For all growth solutions, ultra pure water (18 M Ohm) was the solvent. Growth solution one (GS1) always contained solely the dissolved $Ba(NO_3)_2$. Growth solution (GS2) consisted of $NaNO_3$, Na_2SO_4 and $NaOH$ (Table: 3.1, 3.2, 3.3 and 3.4).

GS1 was always pipetted into the cuvette first and GS2 was pipetted into the middle of the cuvette from 1 cm elevation. This was done meticulously in order to keep the effect of local very high supersaturation as constant as possible between different runs and samples. The samples were flipped 3 times to achieve a homogeneous sample and subsequently transported upright and quickly into the Zetaziser to prevent any potential additional shaking (introducing random kinetic energy) and additional nucleation outside the measuring window. Syringes were reused, but were

specific to one growth solution. They were washed three times after use with deionised water and another three times prior to reuse. Filters, 0.2 μm, (As described in step 1 Figure 3.2) were singular use, as were the cuvettes.

Measuring angle The measurements were performed under three distinct angles. Non-Invasive Backscatter (NIBS 17°), sidescatter (90°) and forward scatter (13°) (Figure 3.3). A theoretical explanation can be found in Section 2.2. All three angles, plus MADLS were used. This was due to the exploratory nature of the research. Suitability of all three angles and the MADLS algorithm was tested for potentially quickly evolving systems. Subsequently, rapid forwardscatter measurements were done (Appendices A.11 and A.12), because this provided a higher time resolution. Forward scatter was chosen, because larger particles were more strongly expressed and the multi-angle measurements revealed that back-and-side scatter showed mostly random patterns in the sub-10nm sizerange, not providing any information on potential growth of the larger size fraction. Heterodyne detection was not considered due to the low amount of material produced and the highest supersaturation occurring the middle of the cuvette, Equation 2.18 was employed.

Suitability of a sample for MADLS

MADLS was the most accurate DLS method available. Due to the low solubility (0.0002448 g/100 mL at 20°) of barite, supersaturation became very high even at low concentrations of barium and sulphate. This caused potential problems due to the small quantity of material made, 30 sub-runs were of 1.68 seconds were performed to improve statistical validity at low concentrations.. This was not true for measurements of an evolving system such as forming and growing barite crystals. MADLS was chosen to due its ability to simultaneously record the developments of different populations in the sample and greatly improving the statistics of a very dilute system.

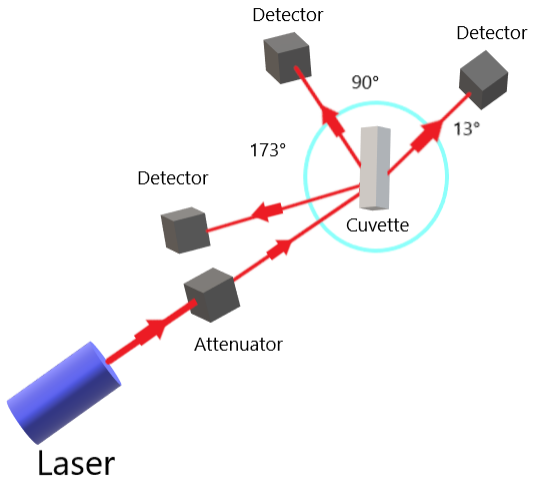

Figure 3.3: Schematic view of different scattering angles available with the Malvern Zetasizer Ultra. Laser is HeNe with $\lambda = 632.8$

Inversion method As a consequence of the arguments provided in 2.3.2, general purpose mode was chosen as inversion method for the calculation of particle sizes.

3.2 SEM

3.2.1 Sample preparation

The samples for the SEM were produced identically to the solutions for the DLS, except that the growth solutions were not filtered beforehand. The volume prepared was 50ml and it was incubated at 21.4 C° for 3 hours. After incubation, it was filtered through a 0.2 μm (Merck Millipore) filter and the water was driven out with isopropanol (90%) (Merck Millipore). The filters were dried for five days at room conditions and protected from dust influences by their protective cover. The filters were cut to the size of the stubs(Microtonano, SEM pin stub Ø12.7 diameter top, standard pin, aluminium) and were stuck on a double-sided conductive carbon sticker (Microtonano, EM-Tec CT12). Because of the non-conductive nature of the target barite crystals, a conductive palladium layer (8nm) was sputtered on top of the sample. An electron beam at 15 KeV was used and the size measurements were done directly in the SEM software.

3.3 Synchrotron

The Synchrotron experiments were performed together with the University of Grenoble and all growth solutions were prepared there beforehand. The initial (t=0) situation was 50mL x 1M KCl in the 150mL teflon reactor. Subsequently, potassium sulfate (K_2SO_4) and barium chloride ($BaCL_2$) were added in varying concentrations during multiple experiments to continuously increase oversaturation (Ω) in the reactor. The 905 metronohm was used as the titrando and was controlled with Tiamo software. The reactant was continuously stirred at a constant rate of 500 rpm. The titration set-up additionally had an 856 Conductivity Module and two 807 Dosing Units of 20 mL. A Metrohm optrode and electrode were placed in the reactor vessel. A thermo-stated liquid cell was used in combination with a peristaltic pump, the sample was kept at 20°. Tubing was silicon and connections were made with epoxy glue. This sample was irradiated by the x-ray originating from the optics hutch. This setup ensured that it was possible to follow the development of particle size distribution and reaction progress simultaneously.

NCD-SWEET beamline The employed beamline had a wavelength range of 0.62 - 1.90 , the photon energy range was 12 keV, the spot size 100x100 Micrometers x Micrometers (FWHM) Horizontal x Vertical, the q-range in nm^{-1} 0.02 to 2 nm^{-1} The flux at the sample position was > 1.510^{12} ph/s and the bandpass ($\frac{\Delta E}{E}$) 2.710^{-4} at 10.0 keV.

3.3.1 Potential 2D-nucleation sites and solutions

The potential problem sites for 2D-nucleation were ubiquitous. 2D-nucleation potentially caused a decrease in Gibbs free energy, which was not thermodynamically involved in the formation of 3D-nuclei. Additionally, it potentially transferred crystals or seeds between experiments. The two expected problem sites were the stirring bars, due to their hydrodynamic and kinetic environment, both promoting nucleation and subsequent detachment of crystals and the diameter changes within the tubing, which provided ample surface irregularities for attachment. Due to increasing evidence that at high supersaturations with respect to the mineral of interest, homogeneous nucleation becomes dominant (Kügler et al. (2016)), these potential issues were accepted. During the experiments, great care was taken to avoid cross-contamination between experiments. Therefore

all reactor vessels, stirring magnets and tubing were cleaned with 10% EDTA for 24 hours before reuse. They were extensively flushed with UPW water before the subsequent experiment.

3.3.2 Data post processing

The phase data of the Fourier transformation (Glatter (1980)) was lost during the experiments, as only intensity was measured. The invariant was related to the molecular mass of scattering particles through the following relationship:

$$Q_{inv} = \int_0^\infty q^2 I(q) dq \tag{3.2}$$

For this study, the invariant was calculated over the complete q-range targeted, from lowest to highest. Induction time of nucleation was measured with the optrode and validated with the invariant becoming nonzero. Quantitatively, this meant that the data was fitted with a sigmoid curve and induction time was defined as the time until the curve deviated 1.5% from its starting value due to density contrast. Averaging multiple time steps was attempted in order to improve the statistical validity of the data, but was eventually disregarded due to the loss of significant features in the data. In order to calculate particle size, spherical particles were assumed and the data was fitted in Python, according to Equation 3.3. Incorporating the sphere form factor (Guinier et al. (1955)), with the q-range chosen so that the form factor was dependent on intensity and the structure factor was disregarded as the particles were assumed to be arranged completely randomly.

$$I(q,r) = (\frac{4}{3}\pi r^3)^2 \, (\rho_1 - \rho_2)^2 \, 3(\frac{\sin qr - qr\cos qr}{(qr)^3})^2 \tag{3.3}$$

where $I(q,r)$ is the intensity, $\rho_1 - \rho_2$ is the density difference between the particles and the solute, r is the radius of the assumed spheres. By integrating this formula and multiplying it with a lognormal distribution of sphere radius r (Deschamps and De Geuser (2011)), the fitting formula was obtained (Equation 3.4). Lognormal radii distribution is the general case for crystal nucleation (Bergmann and Bill (2008)). Lognormal distribution was normalized to one (Equation 3.5), resulting the area to be equal to N (particle number density). In Equation 3.5, μ is the mean of the logarithmic values and s is related to the polydispersity, representing the width of the distribution.

$$I(q) = \int_0^\infty I(q,R) Lognorm(R) dR \tag{3.4}$$

where:

$$Lognorm(R) = NR^{-p} exp(-\frac{(\ln R - \ln \mu)^2}{2s^2}) \tag{3.5}$$

In python, Equation 3.4 was applied as an incremental summation over an arbitrary range of r and a defined range of q. q was defined by the experimental set-up. The equation was subsequently solved through non-linear least squares. This provided a potential solution for the equation parameters. Special care was taken, as non linear least squares was heavily biased by the 'initial guessed set of parameter values', resulting in a local minimum, which was potentially not the optimal solution for the fit. The detector had higher accuracy at intermediate q-values then at the extreme values due to the larger detector area available. Only one dataset was analysed ($r_{aq} = 10$ with a titration velocity of speed of 0.6 mL/s), due to the large difference between the experimental set-up of the SAXS experiment and the performed DLS and SEM experiments.

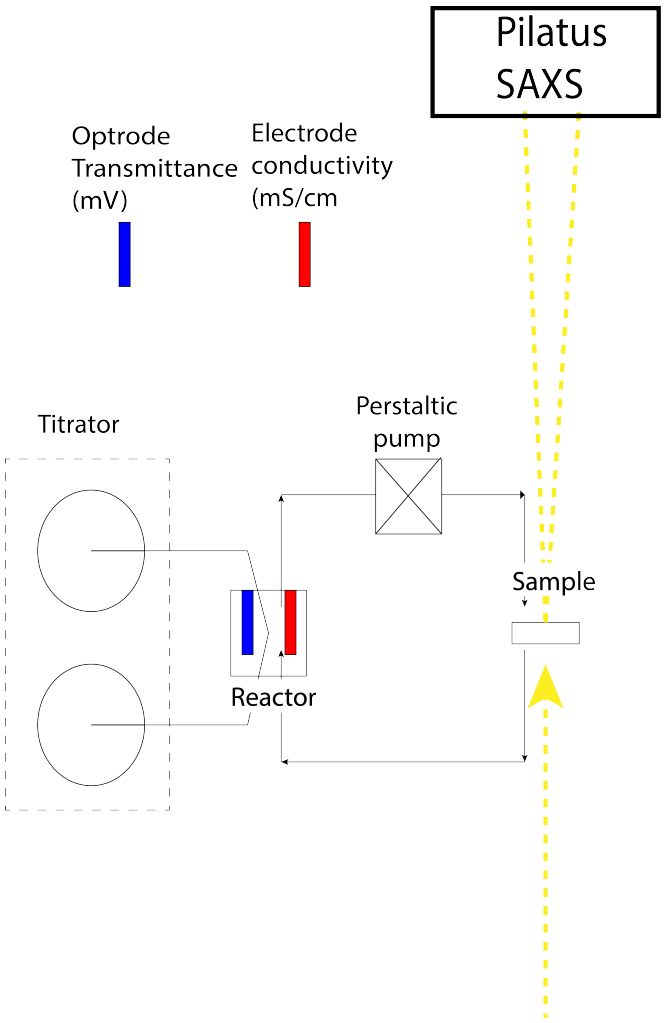

Figure 3.4: Schematic overview of the experimental setup for the Synchrotron (ALBA) in Cerdanyola del Vallès

3.4 Substantiation of the chosen methodology

The synergistic approach of DLS, SEM and SAXS was used to create a more complete picture of barite nucleation and it provided detailed results which allowed for subsequent comparison with models. Through this, hypothesized mechanisms could be checked. MADLS was the most optimal technique available which allowed for in-situ measurements of particle sizes during incubation with adequate statistical validity. Single angle DLS measurements did not suffice due to the high polydispersity of the sample. Each of these individual DLS runs consisted of 30 subruns that had been averaged to obtain the data for one time step. The averaging of five individual runs resulted in minimalization of noise and more accurate results. The SEM allowed for the visualisation of particles outside the analytical window and insight into the effects of stoichiometry on crystal shape. This allowed for better interpretation of the size measurements and trends. The SAXS measurements provided the possibility to track the particle size evolution and to provide a control on the DLS measurements. The inception of the SAXS experiment was done in conjuction with the Univeristy of Grenoble and deviating methods (Background ion, experimental set-up, evolution of supersaturation) led to lowered applicability in this research.

4

Results

The results presented here were obtained using SEM and DLS batch experiments at $\Omega = 100$ and $\Omega = 500$ at stoichiometries of $r_{aq} = 0.01, 0.1, 1, 10$ and 100, an ionic strength of 0.2M and pH 6.7 +- 0.2. SAXS experiments were titration experiments performed in flow at 20° at the same stoichiometries, pH and ionic strength. Results are subdivided in four parts. First, an overview of the formed particles is given through SEM images and size measurements obtained from the measured SEM particles (Appendix A.1). Secondly, crystal size measurements, taken from MADLS of the first and last timestep of the incubation. Thirdly, MADLS-intensity evolution through time, forward-scatter number of particles evolution through time and particle size evolution of sub-10nm particles. Lastly, SAXS data is provided for $r_{aq} = 10$.

4.1 SEM Results

4.1.1 Particle shape and size variation with varying stoichiometry

Crystal shapes at $\Omega = 500$ The shapes of the crystals formed at $\Omega = 500$ vary with stoichiometry (Figure 4.1 second column). Table 4.1 describes the crystal shapes that were identified. At $r_{aq} = 0.01$ (Figure 4.1 D) the crystals were all orthorombic with rounded edges and were euhedral. Crystal A-E on the righthand side of the image had an appendage on its long side. At $r_{aq} = 0.1$ (Figure 4.1 E) the shape variation was higher with orthorombic (A), cubic (B), rhombus (C) and oval shaped (G) crystals. With 36 % of the crystals euhedral and the rest subhedral. Orthorombic (A) and cubic (B) crystals were the most abundant (72% of all crystals) and they were euhedral. The crystals were less elongated than at $r_{aq} = 0.01$ (Figure 4.1 D). With a stoichiometry of $r_{aq} = 1$ (Figure 4.1 F), the crystals were all orthorombic (A). At $r_{aq} = 10$ (Figure 4.1 G), polyhedrons (I) were the most common crystal shape assemblage (30 %) and they were generally anhedral. The variety at $r_{aq} = 10$ was higher than at other stoichiometries with 22 unique shapes, many qualified as undefined (E) (Figure 4.1 G). At $r_{aq} = 100$ (Figure 4.1 H), the crystals were all orthorombic (A) with small deviations and were euhedral. Due to the portrusion on the Z-axis, the whole crystal had a pillowshape.

Crystal shapes at $\Omega = 100$ Strong variation in crystal shape was observed at $\Omega = 100$ (Figure 4.1) between different stoichiometries. At $r_{aq} = 0.1$, no collections of crystals were present, only singular euhedral crystals with an elongated hexagonal shape (D). At $r_{aq} = 1$, the shape diversity was much higher (14 unique shapes), both euhedral and subhedral crystals were present. The most dominant shapes were orthorombic (A), rhombus (C) and polyhedrons (I) (Figure 4.1). At

$r_{aq} = 10$, the crystals were euhedral and were elongated. The assemblage consisted mostly of needle shaped (F) crystals and orthorombic (A) crystals. More crystals were present at $r_{aq} = 10$ than at $r_{aq} = 0.1$, but less than at $r_{aq} = 1$.

Crystal faces At $\Omega = 100$ and $r_{aq} = 0.1$ (Figure 4.1 A) the (001) surface was clearly visible. The length of the crystal, along the b-axis was 3.2 μm and along the a-axis it was 1.8, leading to a ratio of 1.8. The (100) surface was 1um and (210) surface was 1.2μm long. At $r_{aq} = 1$ (Figure 4.1 B) the (210) surface was not visible in many crystals. The (001) surface was visible, bound by the (100) surface. The ratio between the surface area of these faces was variable at this stoichiometry. In Figure 4.1 C, the (100) or the (210) surface was often not expressed or could not be identified in the images, the crystals were either rhomboidal or elongated rods. At $\Omega = 500$ and $r_{aq} = 0.01$, Figure 4.1 D, the crystal faces were unrecognizable. The crystals were longer in the b-axis then a-axis (Figure in introduction). At $r_{aq} = 0.1$ (Figure 4.1 E), the (100) surface was not observed in most crystals. This differs from $r_{aq} = 1$, where the (210) surface is not visible and the (001) surface is bound by the (100) surface. At $r_{aq} = 10$, the crystal faces are not clearly definable, but the (001) surface was bound more often by the (210) surface then the (100) surface. At $r_{aq} = 100$, a line is visible along the middle of the crystals. The (210) surface was not observed in the SEM imagery. At the sides of the crystal, a depression occurs in the middle.

Size information Different (average) sizes were observed at different stoichiometries. At $r_{aq} = 1$ and $\Omega = 500$ the crystals were much larger than at $r_{aq} \neq 1$ (Figure 4.2). At $r_{aq} = 0.1$ the crystals were smallest (318666 nm^2, at $r_{aq} = 0.01$ they were approximately twice as large (762300 nm^2). Increasing the deviation from $r_{aq} = 1$ did not lead to increasingly small crystals. At $\Omega = 100$, the largest particles were observed at $r_{aq} = 10$ (Figure 4.2). They were still significantly smaller than the largest particles at $\Omega = 500$ (40% smaller). At $r_{aq} = 1$ and $\Omega = 100$, the particles were smaller than at the same stoichiometry at $\Omega = 500$ (30x smaller).

Table 4.1: Shape specification of crystals

Shapes		
Orthorombic: A Fig:4.1 H	Cubic: B Fig:4.1 B	Rhombus: C Fig:4.1 B
Elongated Hexagon: D Fig:4.1 A	Undefined: E Fig:4.1 E	Needle shaped: F Fig:4.1 C
Oval: G Fig:4.1 E	Polyhedron : I Fig:4.1 G	

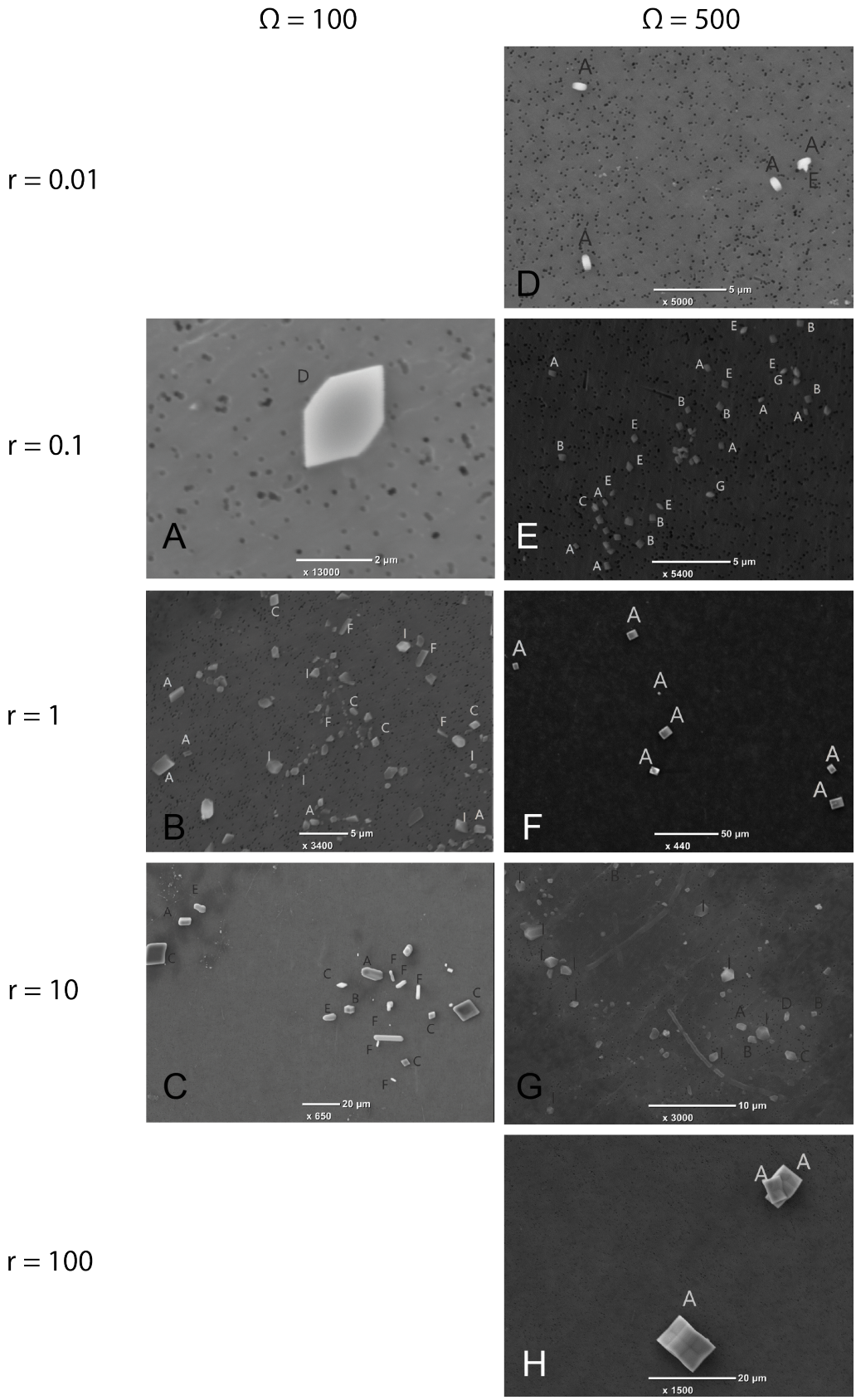

Figure 4.1: SEM results of Omega = 100 and 500 over the complete measured r_{aq} range

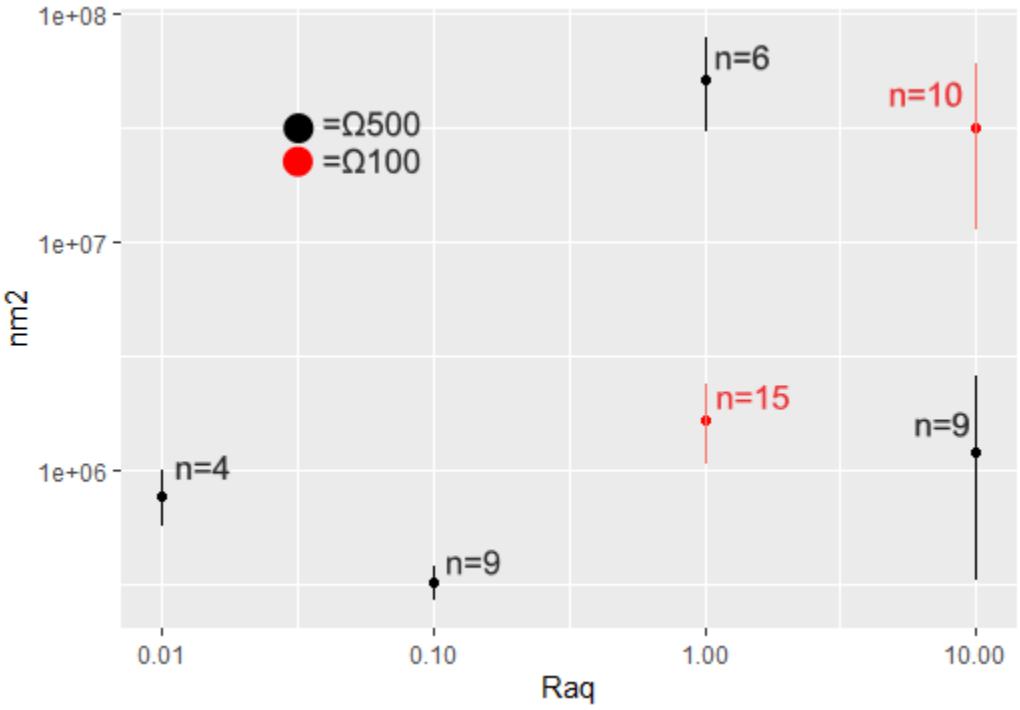

Figure 4.2: Average sizes of crystal size measurements based on Figure A.1

4.2 DLS results

All presented graphs are an average of five individual runs. The standard deviation, assuming a Gaussian distribution, is given in Appendix A.3, A.4, A.5, A.6, A.7, A.8, A.9, A.10.

4.2.1 Crystal population over time

Limited size differences in the most dominantly scattering particles were observed between the first measurement and the last measurement of the incubation (Figure 4.3). All size measurements were between 375 and 425nm of equivalent sphere at all stoichiometries except $r_{aq} = 10$ at timestep 1. At this stoichiometry the initial measurement was of particles of 225 nm.

4.2.2 MADLS Results for $\Omega = 500$

A distinct intensity peak between 370 and 430 nm was observed at all stoichiometries (Figure 4.4 K-O). This peak was continuously observed throughout the whole incubation. Varying stoichiometry did no affect its width or decrease its continuity except at $r_{aq} = 100$, where particles of this sizeclass were less frequently observed. When stoichiometry deviated from $r_{aq} = 1$, the relative intensity decreased, on average, of light scattered by particles in this size range throughout the incubation period. This effect was most pronounced at both $r_{aq} = 0.01$ and $r_{aq} = 100$ (Figure 4.4 K and O). The intensity of these peaks fluctuated between 10% and 35% of total scattered intensity at all stoichiometries. Particles between 214 and 300 nm were very rare at all stoichiometries and between 10 and 200 nm, particles were present at all stoichiometries and times during the experiments. The scattering intensity was largest between 1 and 10 nm at all stoichiometries. The largest scattering intensity was measured between 2 and 5nm in the sub-10nm range. The scattering intensity of particles in the $\leq 10nm$ was higher at $r_{aq} = 100$ (Figure 4.4 O) than at the other stoichiometries

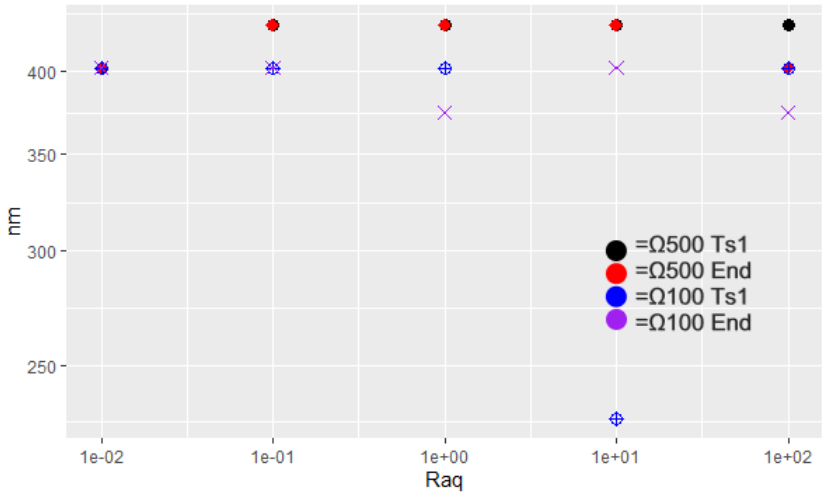

Figure 4.3: Crystal size with the highest scattering intensity in the MADLs measurement at the beginning and end of the incubation period. Where TS1 is the initial measurement and End the final measurement of the incubation.

(Figure 4.4 K-N). Particles larger than 10nm, excluding 370 - 430 nm, scattered less light than particles within the 2-5 nm range. Some particles below 1nm were present at all stoichiometries (Figure 4.4 K-O), they were measured at random intervals. Sometimes particles larger than 430 nm were observed. In general, these particles varied in size with time and stoichiometry. After 4500 seconds (75 minutes), there was an increase of particles between 4000 and 5000 nm at all stoichiometries. At both $r_{aq} = 0.1$ (Figure 4.4 L) and $r_{aq} = 10$ (Figure 4.4 N) the largest size fraction was between 2000 and 2300 nm. At $r_{aq} = 0.01$ and $r_{aq} = 100$ (Figure 4.4 A and E), this population also existed, but to a lesser extent. The standard deviation (Figure A.3, A.4) was very large in all runs and encompassed all observed trends.

4.2.3 Forward Scatter Results $\Omega = 500$

Measurements taken in the forward scattering angle are part of the MADLS results but are also presented separately here (Figure 4.4 P-T). A conversion to percentage of number of particles was performed in contrast to the MADLS plots (Figure 4.4 P-T), where intensity was plotted. A continuous population of particle sizes was visible between 30 and 100 nm at all stochiometries. Higher numbers of particles with this size range was observed at $r_{aq} = 1$ (Figure 4.4 R) than at other r_{aq} values. When deviating from $r_{aq} = 1$ (Figure 4.4 P,Q,S and T), the scattered intensity and therefore number of particles of this size, relative to other particles, decreased, especially at $r_{aq} > 1$ (Figure 4.4 S and T). At these stoichiometries, there was an increased number of measurements where this size fraction was not observed. At all stoichiometries a second size fraction was observed besides 30-100 nm that was relatively constant. At $r_{aq} = 0.01$ (Figure 4.4 P), between 0 and 4500 seconds (0 and 75 minutes), a size fraction between 300 and 600 nm was observed. This population had a slightly lower relative number of particles than the population between 30 and 100 nm. After 4500 seconds (75 minutes) this fraction slowly increased in size up to 1000 nm. Sporadically, particles of around 8000 nm were measured; these occurred more towards the end of the incubation period. The size increase of the 300 to 600 nm population was unique for $r_{aq} = 0.01$ at $\Omega = 500$ (Figure 4.4 P). At $r_{aq} = 0.1$ (Figure 4.4 Q) this population was around 800 nm at the first measurement (Time 0) and slightly increased in size until 4500 seconds. After 6000

seconds, this population was temporarily underrepresented. The largest fraction, around 8000 nm, was present more than at $r_{aq} = 0.01$ (Figure 4.4 P). At $r_{aq} = 1$ (Figure 4.4 R), a population centered around 800 nm was also present at the start of the experiment and existed throughout the incubation period. During the incubation, its size slowly decreased to 200 nm. After 3500 seconds (58 minutes), larger particles of around 8000nm were measured. This was very similar to $r_{aq} = 10$ (Figure 4.4 S). At $r_{aq} = 100$, the population between 100-1000nm (Figure 4.4 T) was very stable and increased from 400 nm to 800 nm. At all measured stoichiometries, except $r_{aq} = 100$ (Figure 4.4 T), there was a population between 0.55 and 0.74 nm. This population was represented more strongly at more extreme stoichiometries. All compound graphs had a large standard deviation (Figure A.5, A.6), enclosing all described data.

4.2.4 MADLS Results $\Omega = 100$

At all stochiometries except $r_{aq} = 100$ (Figure 4.4 A-E), there was a clear population centered around 400nm (380 - 420 nm). This population changed very little through time at all tested stoichiometries. Most scattering occurred due to particles between 1 and 10nm at all stoichiometries with the highest scattering intensity produced by particles between 3 and 6 nm. Above 10nm till 150nm, the relative scattering intensity of particles decreased the larger particles were. The scattering intensity between 150 and 300 nm was very limited at all stoichiometries. A second, less abundant population between 2100 and 2300 nm was present in all samples. It was most abundant at $r_{aq} = 1$ (Figure 4.4 C) and $r_{aq} = 10$ (Figure 4.4 D). At $r_{aq} = 0.1$ (Figure 4.4 B) and $r_{aq} = 10$ (Figure 4.4 D), even larger particles were sporadically present, between 4300 and 4900 nm. These were absent at other stoichiometries, except for two instances at $r_{aq} = 0.01$ (Figure 4.4 E). The difference between individual runs was very high (Figure A.7, A.8).

4.2.5 Forward scatter results $\Omega = 100$

The scattering patterns at stoichiometries $r_{aq} = 0.01$ and $r_{aq} = 0.1$ were very similar (Figure 4.4 F and J), both having the largest percentage of particles around 60nm and a second group at 4000nm. Additionally, sub-nanometer particles were measured at both stochiometries. The size variety was largest at $r_{aq} = 0.01$ (Figure 4.4 F) during the first 1500 seconds (25 minutes) of development and between 7500 and 10000 seconds (125 - 167 minutes). The largest size fraction appeared after 1000 seconds (17 minutes). At $r_{aq} = 0.1$ (Figure 4.4 G), particles between 100 and 1000 nm appeared and disappear throughout the measured time period. The 60 nm population increased in size diversity and absolute size after 7300 seconds (122 minutes). The largest population was continuously present throughout the experiment. At $r_{aq} = 1$ (Figure 4.4 H) a similar population was observed with a size of 60 nm in the initial stages of the experiment, until 3500 seconds (58 minutes). Subsequently, the diversity and absolute size was generally increasing. There was a strong signal of sub-nm particles. Sporadically, a population of particles centered around 5500nm was observed. At $r_{aq} = 10$ (Figure 4.4 I), the largest diversity in particles sizes was measured. Its main population was centered around 380 nm. The size fractions present at the other stoichiometries were observed at $r_{aq} = 10$ as well. The largest size fraction, however, covered a larger size range than at the other stoichiometries. The fraction between 60 and 90 nm was most abundant between 3000 and 7500 seconds (50 - 125 minutes), besides being present at the beginning of the incubation. The sub-100 nm fraction was measured throughout most of the sample. At $r_{aq} = 100$ (Figure 4.4 J), the scattering was dominated by the largest size fraction, between 3500 and 6300 nm, skewed towards the upper end of the fraction. Particles with a size between 300 and 450 nm became

more abundant and smaller throughout the experiment. Occasionally, particles of approximately 60 nm were measured. Particles of sub-nanometer were measured, similar to the measurement at other stoichiometries. The missing data after 9000 seconds (Figure 4.4 A, B, C, N and O) was the result of excessively large time differences between the measuring moments of individual runs. By integrating the time steps of the individual measurements, a gap was created. All experiments had a large spread of data points and large variability between runs (Figure A.9, A.10).

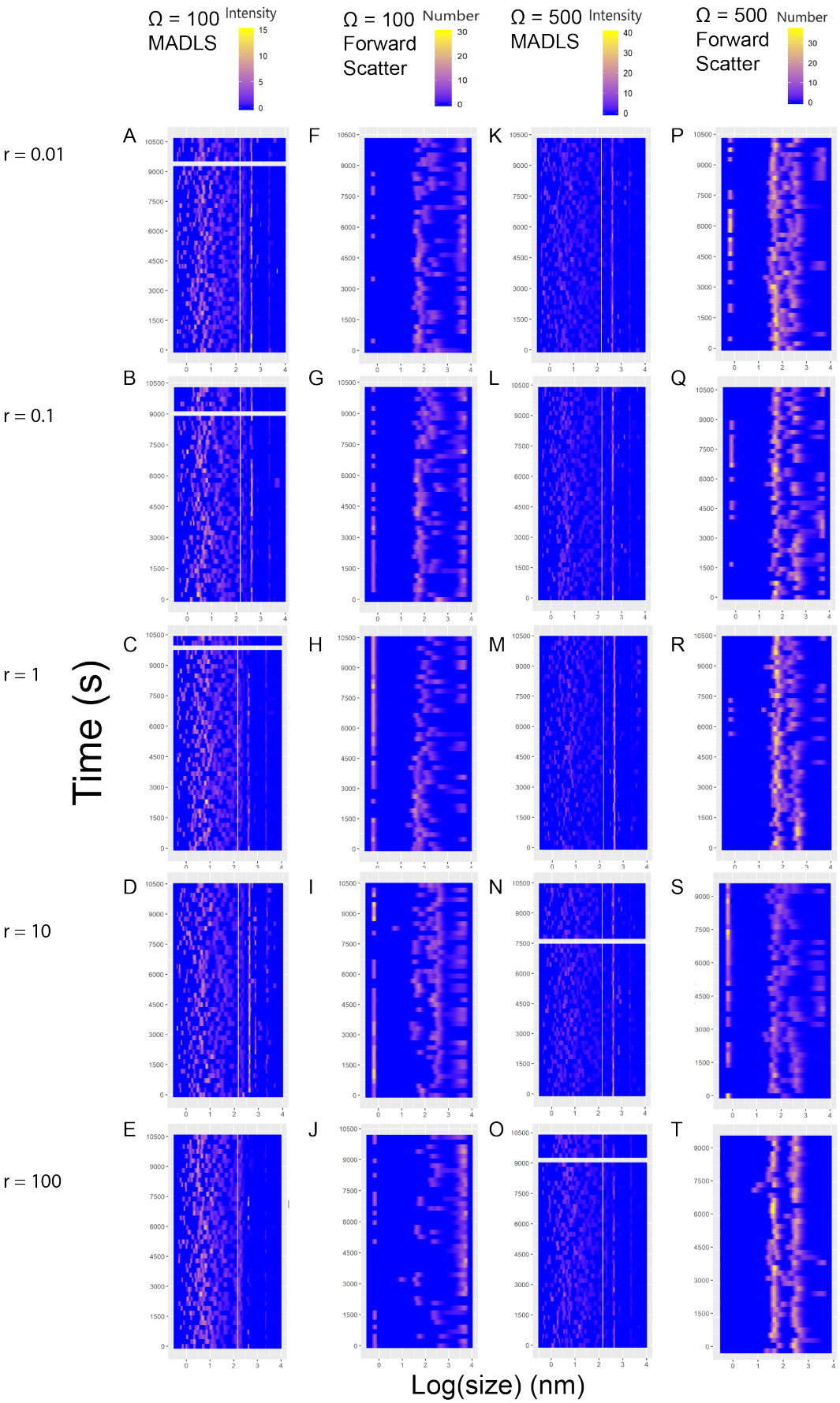

Figure 4.4: Compound MADLS results of $\Omega = 100$ and $\Omega = 500$ over the full measured r_{aq} range

4.2.6 Sub-10nm particles

Figure 4.5 A-J and Figure 4.6 A-J show the development of the 2 smallest populations during the first 3000 seconds (50 minutes) at different stoichiometries. A linear regression is given in red and the confidence interval of this regression in green. The smallest size fraction at $r_{aq} = 0.01$ (Figure 4.5 A and Figure 4.6 A) decreased in size over the course of the experiment at both stoichiometries. In terms of absolute size it was bigger at $\Omega = 100$. The larger size fraction decreased in size at $\Omega = 100$ (Figure 4.5 F) and increased in size at $\Omega = 500$ (Figure 4.6 F). It was smaller (between 1.5 and 2nm) than at $\Omega = 100$. The small size fraction at a stoichiometry of $r_{aq} = 0.1$ (Figure 4.5 B and Figure 4.6 B) showed a decreasing linear trend at both stoichiometries. The linear regression did however not fit the data very well, it displayed a large margin of error. In terms of absolute size, the particles at $\Omega = 500$ were slightly larger (0.6nm larger). The larger size fraction at this stoichiometry showed very similar behaviour for both $\Omega's$ (Figure 4.5 G and Figure 4.6 G). Both slightly increased in size (0.3 nm and 0.6nm respectively). The particles were slightly larger at $\Omega = 500$ (0.4nm). At $r_{aq} = 1$, there was a slight downward trend at $\Omega = 100$ (Figure 4.5 C) and a clear downward trend at $\Omega = 500$ (Figure 4.6 C). After 3000 seconds (60 minutes) the particles were approximately the same size (1.5nm). At the start of the incubation, the particles at $\Omega = 500$ were larger (0.76nm). The larger size fraction at $r_{aq} = 1$ did also decrease in size over time at both $\Omega's$. 0.25nm at $\Omega = 100$ (Figure 4.5 H) and 2nm at $\Omega = 500$ (Figure 4.6 H). The larger size fraction was 2.65nm bigger at the start of the incubation (5nm *versus* 2.35nm). The smaller size fraction at $r_{aq} = 10$ was very similar in size at both $\Omega's$ (1.5nm) (Figure 4.5 D and Figure 4.6 D) and did not show a clear increase or decrease in size. The spread in sizes was also similar. The larger sizes fraction did grow at both stoichiometries (Figure 4.5 I and Figure 4.6 I) and was more pronounced at $\Omega = 500$. With an increase in size of 2nm over 3000 seconds and 0.25 nm at $\Omega = 100$. The size of this this fraction was very similar at both $\Omega's$ (2.3 nm). At $\Omega = 100$ and $r_{aq} = 100$ (Figure 4.5 E), the spread of particle sizes was very large and no clear trend was discernible. The particles were slightly smaller than at $\Omega = 500$ (Figure 4.6 E) (0.15nm). At $\Omega = 500$ the particle size evolution did not show a clear trend and the particles were between 1.05 and 2.12 nm large. The larger size fraction at $r_{aq} = 100$ (Figure 4.5 J and Figure 4.6 J), there was no clear linear trend. The particles were, on average, larger (1.1 nm) at $\Omega = 500$ than at $\Omega = 100$. The smaller and larger size fraction were generally bigger at $\Omega = 500$, with the notable exception of $r_{aq} = 0.01$, where it was inverse for the larger fraction and $r_{aq} = 10$. Where the smaller size fraction was equally sized at both $\Omega's$. At both $\Omega's$, increasing concentrations of barium led to, on average, smaller particles in both size fractions. The effect was however more strongly present in the smaller fraction.

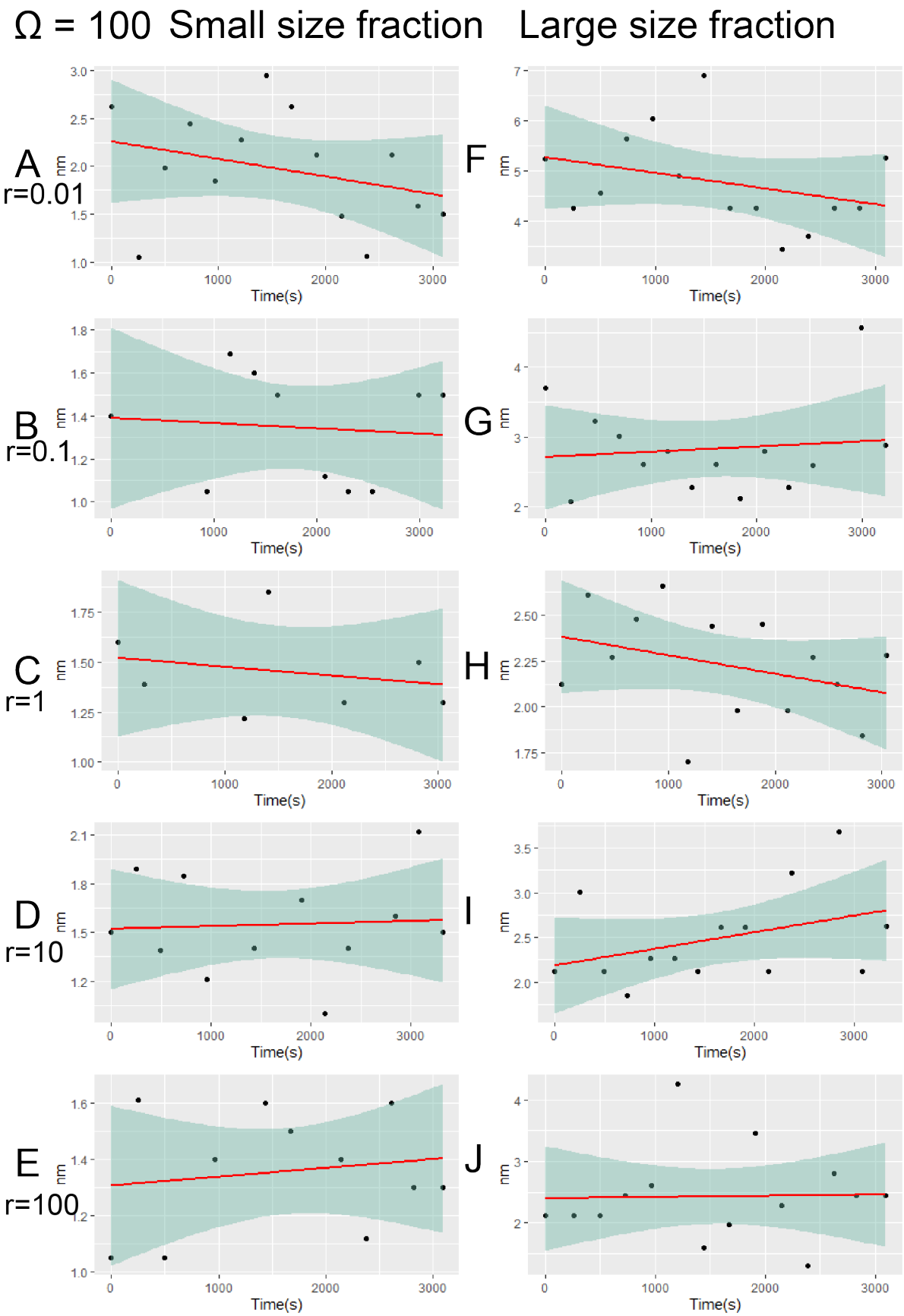

Figure 4.5: Evolution of sub-10nm particles over time at $\Omega = 100$ and all measured stoichiometries

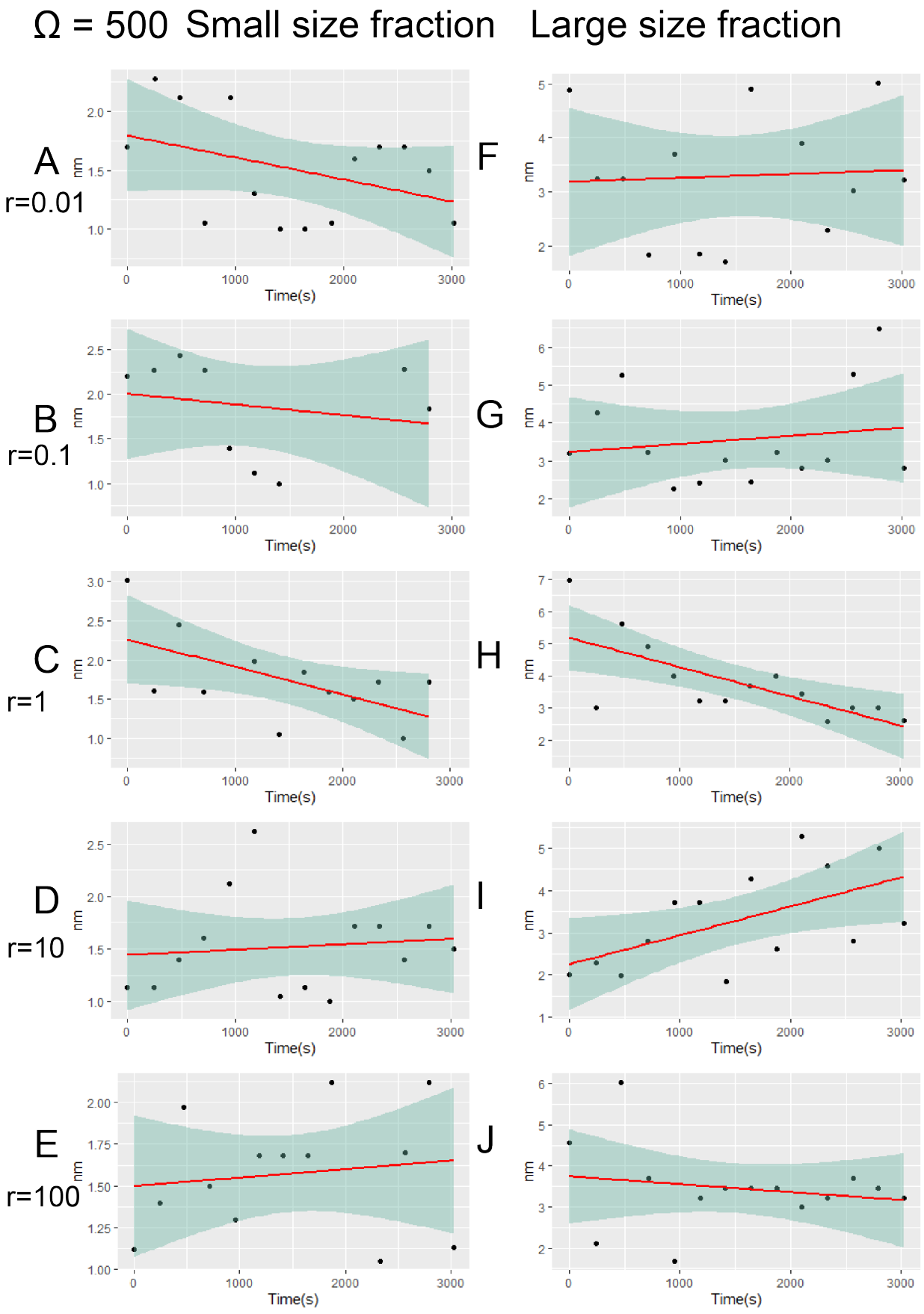

Figure 4.6: Evolution of sub-10nm particles over time at $\Omega = 500$ and all measured stoichiometries

4.3 SAXS data

The data of the $r_{aq} = 10$ titration SAXS experiment is presented here. The rest of the data can be accessed in Baken (2020). The data presented here is subdivided into 3 separate parts. Firstly, Figure 4.8 A, a Guinier plot (I(q) vs q^{-1}), with all the processed time steps. Secondly, the invariant curve for this dataset is plotted in Figure 4.8 B, validated with SAXS and optrode data. Lastly, Figure 4.8 C-F are the curves fitted through measured data for a limited q-range (I(q) vs q^{-1} graphs). The fitted time steps were chosen to coincide with a deviation of 1.5% of the invariant in regard to its background value. This value was reached after 66 minutes and coincides with the first measured frames (Figure 4.8 C).

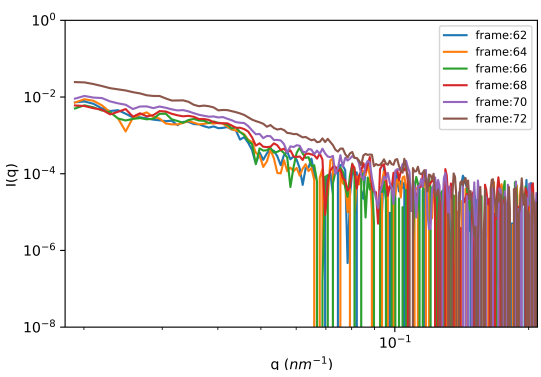

(a) Multiplot of SAXS experiment $r_{aq} = 10$

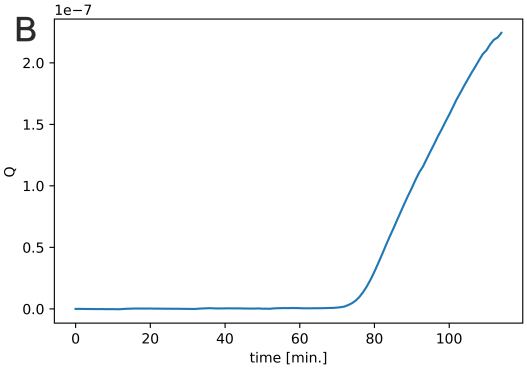

(b) Invariant of SAXS experiment $r_{aq} = 10$

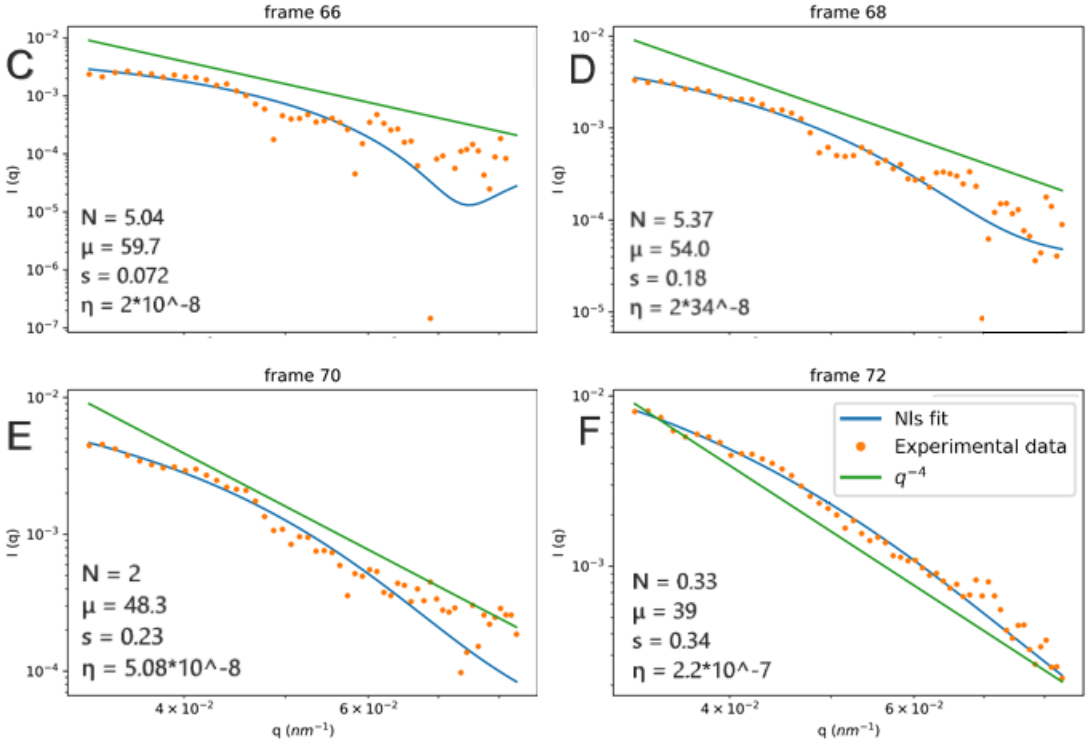

Figure 4.8: NLLS fitted SAXS data of timestep 66 till 72 at $r_{aq} = 10$ and a titration speed of 0.6 ml/s, dt = 2 min

The particle number density N was relatively stable between frame 66 and 68 (5.04 to 5.37) and rapidly decreasing after, reaching a value of 0.33. The mean of the logarithmic values μ steadily decreased through time (59.7 to 39). The width of the size distribution s increased with time and the electron scattering length (η) increased.

5

Discussion

The discussion is subdivided into five segments. The first section describes how the data can be viewed in order to be relevant for the research questions. These research questions will be subsequently discussed in order, exploring the processes causing variation in particle size due to stoichiometry, the relationship between critical nucleus size and stoichiometry and the change in crystal morphology due to varying stoichiometry . Subsequently, recommendations for future research into crystal nucleation are given and the societal relevance of the research is provided. Lastly, a section is dedicated to the limitations of the study.

5.1 Reducing the DLS data

To distill useful and factual information from the DLS graphs, a number of data points need to be discussed first. The sub-nm particles are not the goal of this research. This population is most likely a combination of different ion-pairs. This derives from the fact that it is present in every experiment when no other particles are measured and we know that these pairs form and dissolve continuously (Denisov et al. (2003)). Proper differentiation can not be made with high confidence between any kind of ion pair at the sub-nm scale due to the large mix and the rapidly changing ion-pair combinations. Additionally, they are close to the minimum size detection limit of the Zetasizer Ultra. The effect of different stoichiometry on particle size evolution can not be seen separately from the effects of different amounts of background salts at the sub-nm scale. With stoichiometry, the total concentrations of background salts varies, and this will be part of the variability seen in peak intensity at the sub-nm level. More importantly, since the critical nucleus size is generally above 1 nm (De Yoreo and Vekilov (2003)), the population observed below 1 nm can be disregarded in further discussion.
It is vital to note that the MADLS plots are all relative intensity plots whereas the forward scatter plots are number of particles. When larger particles appear or become more numerous, this will decrease the relative intensity of the peaks created by smaller particles, while they may not be decreasing in numbers. So discussing variability in intensity in the MADLS plots should not be disconnected from changes in the other peaks in the same MADLS plot. Evaluating both the MADLS data and the forward scattering data is done in order to highlight different populations. The MADLS plots are used to gain insight into the smaller size populations whereas the forward scatter plots highlight the larger populations. The calculation to number was made in order to show the full range of particle sizes in the forward scattering plots (otherwise, the high scattering intensity of the largest particles obscures the other particles). Caution should be exercised when

discussing particle sizes that are measured infrequently. Due to the stochastic nature of the measured particles (Section 5.7.1) and the complex behaviour of relative scattering intensity over the particle size range investigated, it is impossible to differentiate between particles that have recently formed and particles that are there continuously or for longer periods, but in too low numbers to result in detectable scattering. For the same reason, the fact that they are not measured at a different stoichiometry does not ensure their absence: they might simply not be measured due to their low abundance.Therefore, only particle sizes that are measured consistently for at least 12 minutes (3 timesteps for MADLS) and trends within them can be discussed adequately and compared between measurements.
The effects of shape on the size measurement (Section 2.2) is a concern for the DLS measurements. Growth or dissolution on needle shaped crystals (Figure 4.1 C), is not recorded accurately. Growth in the crystals preferred direction, along the length of the needle, will increase the measured size as this influences the translational diffusion coefficient (Equation 2.10). An increase in width, due to for example 2D-nucleation or growth on the (100) surface, will not be recorded equally because the effect on the translational diffusion coefficient is very limited. At $r_{aq} > 1$ and $\Omega = 100$ (Figure 4.1 C), particles are more elongated than at $\Omega = 500$. Making comparisons between sizes and growth rates more inaccurate. Due to this, a population calculated to have an equivalent sphere radius of 380nm belongs to the same populations as another particle measured at 430 nm. They are likely similar in terms of volume.

5.2 Processes causing variations in particle size

At $\Omega = 100$ and $\Omega = 500$ (MADLS) the dominant crystal size is centered around 400nm for all stoichiometries, except at $r_{aq} = 100$ at $\Omega = 100$. At extreme stoichiometries, depletion of one specific ion is more likely as the concentration of one ion will be very low. Over the course of the experiment, the concentration of the limited ion will continue to decrease. Potentially even more rapidly than the abundant ion, due to the abundance of open attachment sites for the depleted ion. The depletion of this ion also decreases the supersaturation more rapidly than the decrease in the abundant ion. The 400-nm population exists at $\Omega = 100$ and $r_{aq} = 100$ but is it significantly less abundant than at $\Omega = 500$. A possible explanation is a method related problem. In the forward scatter measurements (Figure 4.4 J), the relative intensity of the larger particles is bigger than at other stoichiometries at $\Omega = 100$. This decreases the relative measured intensity of the smaller size fractions. This would also explain the difference with $\Omega = 500$ (Figure 4.4 O), as this large size fraction is not visible in Figure 4.4 T and consequently does not lower the relative intensity of the 400nm populations. Another potential, process related, explanation is the depletion of sulphate ions at $\Omega = 100$ and $r_{aq} = 100$. Lower barium concentration, $\Omega = 100$ and $r_{aq} = 0.01$, does not have the same effect. Sulphate does not preferentially form other ion-pairs compared to barite (Appendix A.13), making it curious that this effect is not similar at both extreme stoichiometries. The underlying reason could be that the water exchange kinetics (Section 2.1.5) is more rapid for sulphate than for barium (Kowacz et al. (2007)). This means that effective contact between ions is more likely and the sulphate is removed from the system more rapidly than barium at the inverse stoichiometry. If sulphate is incorporated more easily, and sedimentation removes material from the system, then the higher water exchange frequency around sulphate would explain the more rapid depletion. Sedimentation at $\Omega = 100$ could happen more quickly than at $\Omega = 500$ because at higher supersaturation ($\Omega = 500$), 3D-nucleation is favoured, because the energy barrier in Equation 2.3 is quickly surpassed throughout the solution. This, almost instantaneously, creates a

large and relatively homogeneous populations, rapidly reducing the material available for growth. These particles do not settle and thus, do not remove the sulphate from the system. This could be tested by modifying the pH; lowering the pH at $r_{aq} = 0.01$ should increase the water exchange frequency around barium (Tomson et al. (2004b)) and, consequently, result in similar populations as at a stoichiometry of $r_{aq} = 100$ at $r_{aq} = 0.01$ (Kowacz and Putnis (2008)). An alternative explanation would be that the surface conditions of the sub-100nm particles are more favourable for larger aggregates at this stoichiometry. Preventing a stable population of 400nm particles by rapidly forming areas of increased density or true aggregates of a much larger size. This idea is substantiated by the forward scatter results, which clearly show a much higher relative presence of very large particles ($> 1000nm$) at $\Omega = 100$ and $r_{aq} = 100$ than for the other stochiometries and $\Omega's$. This preference can most likely not be explained by ZP, as the ionic strength of the solution is high enough to suppress the ZP to a large degree, and thus limit its effect on the stability of the system. The most likely explanation for the difference in presence of large particles is a dependency of growth on solution stoichiometry (Kowacz et al. (2007) Hellevang et al. (2014) Hellevang et al. (2016)). As the SEM images show increasing size with increasing barium concentrations (Figure 4.1 C).

The largest, in terms of size, population at all stoichiometries, mostly visible in the forward scattering angle, shows some disparity in size. Quantitative statements regarding the variability in populations with the largest size at different experimental conditions is difficult for various reasons. Firstly, the subdivisions of size classes becomes larger towards the higher sizes, decreasing the accuracy of the measurement. Secondly, sedimentation of larger particles can not be discounted. In the exemplary correlation diagram (Appendix A.14), signs of sedimentation are observed as shown in (Figure 2.15). Under the SEM, particles of sufficient size for sedimentation are observed. It is however clear that at $\Omega = 100$ (Figure 4.4 F-J), the largest particles are much more strongly represented and larger than at $\Omega = 500$ (Figure 4.4 P-T). This seems counter intuitive, as more material is available at $\Omega = 500$ than at $\Omega = 100$, thus, more material is technically available for larger and more large particles. Yet, there is a multitude of possible explanations for this observation. The occasional appearance of very large particles at $\Omega = 500$ (Figure 4.4 P-T) and it being likely sedimentation occurs, could mean that at $\Omega = 500$, the largest population rapidly increases to a size outside the measuring window. This is supported by the SEM images, which show particles significantly too large to be measured in the DLS (Figure 4.1 H). Consequently, it seems like the formation of larger particles is inhibited, whereas it potentially increased. As mentioned previously, the potential preference for 3D-nucleation of a strongly oversaturated solution could also lead to a rapid loss in crystal building ions. Significantly limiting the potential to grow crystals near the upper limit of the DLS, as they are either too small or have coalesced into large particles which sediment.

Deviating from $r_{aq} = 1$ at $\Omega = 500$ makes the measurements of large particles more common except at the most extreme stoichiometries in the DLS measurements(Figure 4.4 P-T). Previous work has shown that a stoichiometry where barium activity (Ba^{2+}) exceeds sulphate activity (SO_4^{2-}) leads to increased growth rates (Kowacz et al. (2007)). At higher $\Omega's$, increasing amounts of barium are needed for maximum growthrate. This work is however, performed at significantly lower Ω. The trend that more barium is needed at higher stoichiometries seems to continue in our data at $\Omega = 100$ with the largest particles measured at $r_{aq} = 100$. At $\Omega = 500$ there could be a break with this trend, the increased Ω could cause more 3D-nucleation in favour of 2D-nucleation, preexisting cleavage step advancement and ion-addition growth, as the energy barrier for 3D-nucleation is surpassed. Making a stoichiometry of $r_{aq} = 10$ more suitable than $r_{aq} = 100$ for crystal growth. The desolvation of specific surface sites can be aided by anion (SO_4^{2-}) adhesion

(Piana et al. (2006)). This potentially makes the barium (Ba^{2+}) that is present more likely to grow than form new nucleii. Leading to larger particles. This hypothesis is further supported by the large size fraction of Figure 4.5 I and Figure 4.6 I. Where $r_{aq} = 10$ has the highest growth rate. It could also be, that due to the aided desolvation of the surface (Piana et al. (2006)), larger aggregates are formed. These aggregates can not be recognized on the SEM, as the resolution is too small but can form an important part of crystal growth (Penn and Soltis (2014)). The SEM imagery shows the largest particles at $r_{aq} = 1$ (Figure 4.1 F), followed by $r_{aq} = 100$ (Figure 4.1 H) and $r_{aq} = 10$ (Figure 4.1 G). This disconnect can be explained, as these particles fall outside the measurement range of the DLS. It could be that the abundance of sulphate leads to preexisting cleavage step advancement and ion-addition growth whereas abundant barium leads to coalesence of particles, rapidly exceeding the measurement window.

The forward scattering angle reveals a second population at all stoichiometries between 60 and 100 nm. This population is not as visible in the MADLS plot as its scattering is surpressed by other populations at different scattering angles. This population is very stable at $r_{aq} = 1$ for $\Omega = 500$, but slowly increases in size at $\Omega = 100$ and $r_{aq} = 1$. It is interesting to note that the increase in size seems to be linear on a logarithmic scale under these conditions. This indicates increasingly rapid growth. During the incubation, the supersaturation, Ω in Equation 2.4 decreases. This makes 2D-nucleation more prominent while decreasing the amount of 3D-nucleation, as the free energy barrier for 3D-nucleation is larger than for 2D-nucleation. This growth is also visible to some extent in $r_{aq} = 0.01$ and $r_{aq} = 0.1$, not clearly in $r_{aq} = 10$ and potentially in $r_{aq} = 100$. At $r_{aq} = 100$, it can not be decisively stated due to the low number of measurements. That the switch from 3D-nucleation to 2D-nucleation plays a role is supported by the fact that growth is more strongly represented at $\Omega = 100$ than at $\Omega = 500$, as the free energy barrier for 3D-nucleation is less likely to be reached.

Figure 4.3 shows deviating behaviour for the first size measurement at $\Omega = 100$ and $r_{aq} = 10$. Observing Figure 4.4 N shows that this difference with the other measured parameters is only a single deviating measurement and does not seem to indicate anything related to different behaviour.

Higher sulphate activity seems to result in preexisting cleavage step advancement and ion-addition growth, slowly increasing the size of populations (Figure 2.4), whereas higher barium activity leads to more distinct population sizes with very few occurrences between these distinct size classes. This means that multiple particles potentially coalesce into a larger particle. This coalescing is made more likely by the previous mentioned surpression of the ZP. If this is the case, there is a stoichiometric dependency of growth mode. This is supported by the fact that the dominant size class is centered around 400 nm at all stoichiometries in MADLS but more large particles are observed at $r_{aq} > 1$ than at $r_{aq} < 1$ in the forward scatter. Pointing towards coalesence of particles at $\Omega = 100$ (Hellevang et al. (2014); Hellevang et al. (2016)). The same effect can be observed to some extent at $\Omega = 500$, with the highest growth rate at $r_{aq} = 10$ (Figure 4.4 S). The effect can be observed much clearer at $\Omega = 100$. The SEM imaging does not provide sufficient resolution to reject this hypothesis.

5.2.1 Inferences from SAXS

The SAXS data set is not extensive enough to make any quantative statements. Very clear trends can however be seen for the individual parameters (Figure 4.8). Particle number density stayed stable around the nucleation and subsequently rapidly decreased after nucleation started occuring, this may be explained by the formation of a large population of nucleii and subsequent coalescing. This hypothesis is supported by an increase in size width distribution (s) (Figure 4.8). At the

moment of nucleation (4.8 C), the particles should all be approximately the same size (critical nucleus size) and consequently have a low (s). Subsequent increase in (s) over all time frames points, as hypothesised in Section 5.3, to near random coalescing between differently sized particles combined with growth. The electron scattering (η) length arises from the electron density, the increase observed here is related to an increase in scattering power of the volume. Ordered crystals scatter more strongly than unordered precursors or higher ion density regions, as proposed in Figure 2.5. It is expected that after nucleation occurred, surface fractal structures increase (Chattopadhyay et al. (2005)), pushing X-ray scattering to increasingly small values, outside the q-range of this experiment and thus becoming invisible. This has been documented before for aggregates (Bale and Schmidt (1984); Keefer and Schaefer (1986)), due to an aggregate being a self repeating structure formed by a near-random process. The effects of background electrolytes on nucleation has been extensively documented (Piana et al. (2006); Kowacz et al. (2007);Jones et al. (2008)) hindering comparisons with the DLS and SEM datasets. Limitations of the SAXS data set additionally arise from the fact that no comparison can be made between different stoichiometries due to the limited amount of processed data and the aformentioned difference in background electrolyte ($NaNO_3$ in the DLS and KCl in the SAXS experiments). Additionally, no standard deviation can be calculated because only one experiment was explored. Despite the preliminary nature of the presented SAXS data, it is interesting to see that coalesence of particles likely occurs at $r_{aq} = 10$. This is in line with the observations made it in the DLS and further supports the hypothesis that growth is dominated by aggregation and potentially 2D-nucleation at higher stoichiometry ($r_{aq} > 1$). The SAXS fits are however not completely satisfactory as the fitting was performed with non-linear least squares instead of the more appropriate Monte Carlo fit.

5.3 Relationship between critical nucleus size and stoichiometry

Although the sub-100nm particles are very polydisperse at all stoichiometries. There is a predominance of particles between 1 and 10nm (Figure 4.4). The two most dominant size fractions within this sizerange are plotted in Figure 4.5 and 4.6. It is likely that the smallest stable population is the critical nucleus size. As this is the first almost continuously existing population. As previously discussed, the critical nucleus size is the smallest size at which it is thermodynamically favourable to form a new phase. Prior research indicates that generally critical nucleus size falls between 1 and 10 nm (De Yoreo and Vekilov (2003)), which is in line with our findings. Ω is identified as the main driver of variation in critical nucleus size at constant temperature, pressure and medium. With higher supersaturation leading to smaller particles. This holds only for $r = 0.01$ in the performed experiments. At higher stoichiometries, the critical nucleus size is either higher (Figure 4.6 B) or similar (Figure 4.6 C, D and E). A possible explanation is that the critical nucleus size at $\Omega = 500$ lies under 1nm and falls outside the analysed size range. These measurements were however disregarded, as it is impossible to differentiate from ion aggregates. Another alternative is that the small size fraction at $\Omega = 100$ is still sub-critical. This is supported by the fact that the size measurements fluctuate strongly, the particles are occasionally not present at all and that the particle size seems to decrease in some measurements (4.5 A, B and C). During the experiment, supersaturation decreases and consequently, critical nucleus size should increase. This trend in particle size might be explained by dissolution of small particles in favour of larger particles, which are even more thermodynamically stable as their ratio between phase boundary and bulk material is more beneficial (Equation 2.6).

The average particle size of the smaller size fraction decreases at higher stoichiometries (Higher Ba^{2+}). This leads to a very similar pattern as identified in Kowacz et al. (2007), with higher barium activity provides more favourable conditions for crystal growth. This data indicates that it also makes the conditions for nucleation more favourable. This could again be a consequence of the slower water exchange kinetics around barium (Kowacz et al. (2007)). They hypothesize that the energy barrier for 2D-nucleation can not only be overcome thermodynamically but also kinetically. These observations suggest that the energy barrier for 3D-nucleation can also be overcome kinetically.

At $\Omega = 100$ and $r_{aq} = 0.1$ has a smaller average particle size than $r_{aq} = 1$ and $r_{aq} = 10$ for the small size fraction. This goes against the earlier described trend, of higher barium activity creating smaller critical nucleii and creating more favourable conditions for growth. A possible process related explanation is that the supersaturation at $\Omega = 100$ and $r_{aq} = 0.1$ is slightly higher (Table 3.1). The effect of supersaturation seems to be limited however, as the smaller size fraction is not smaller at $\Omega = 500$ than at $\Omega = 100$. The size measurements are highly diverse at $r_{aq} = 0.1$ (Figure 4.5 B), and the trend falls withing the margin of error. So the trend may not be invalidated by this measurement.

The high variety and discontinuity of the particles above the 1-10 nm range can explained by the random, continuous coagulation of critical particles, with other (sub)critical particles of all sizes. This also explains the high standard deviation in this size range (Appendix Figures A.7, A.8, A.3 and A.4), because the combinations of particles are made is different in every run. Short term coagulation is very likely due to the suppression of the ZP by the high ionic strength (Section 2.3.2).

5.4 Crystal morphology and size in relation to stoichiometry

The main objective of the SEM imagery is to identify the deviation from the equivalent sphere, to understand how many of these very large particles have formed and to measure the size of the largest particles in the solution. Due to the low resolution of the images, it is hard to differentiate precisely between the different crystal faces. There is difference in crystal morphology as a result of varying stoichiometry. At $\Omega = 100$ and $r_{aq} = 0.1$ (Figure 4.1 A) the length/width ratio is 1.8, which is close to the ratio of a barite crystal (1.627) (Klein and Hurlbut (1985)). The ratio is very diverse at $r_{aq} = 1$ (Figure 4.1 B) and the (001) surface is bound by a well developed (100) surface and a poorly developed (210) face in most crystals. When the (210) face is expressed, see rhomboidal crystals, the plane angles are on average 104.73, closely following Klein and Hurlbut (1985). The same effects can be seen at $r_{aq} = 10$. The crystals identified as C (Rhombus) have a completely suppressed (100) surface and the (001) surface is only bound by the (210) face. When the (210) face is expressed, the angles vary between 95.6° and 105.3°, approximating the values cited in literature (Klein and Hurlbut (1985)). The other extreme is also observed, the elongated crystals (F) (Figure 4.1 C) have grown more strongly along the [010] (b-axis in Figure 2.11), with potential growth on {210} faces bound by {100} surfaces, leading to a ratio of $\frac{b}{a}$ (Figure 2.11) of 4.8 in the most extreme case, deviating from the expected 1.627 ratio. These differences in crystals shape are to be expected as it has been extensively reported that differences in background electrolyte concentration can change growth rates of different crystal planes due to specific interaction between surface sites and background electrolyte (Risthaus et al. (2001)), that ions in solution can affect desolvation kinetics of crystal building ions (Kowacz and Putnis

(2008)) and that growth rates on specific surfaces are modified by the ions in solution Godinho and Stack (2015)). At $\Omega = 500$, there is no clear expression of the (210) surface at $r_{aq} = 0.01$. The crystals are elongated along the [010] (b-axis in Figure 2.11). The resolution is very low, but they seem to be tapered crystals. At $r_{aq} = 0.1$, the (100) face is not observed in most crystals. This is in contrast with the observations at $r_{aq} = 1$, where the (210) side is often absent. Growth is mostly expressed along the [010] direction and some growth along the [100] direction. The shape variety at $r_{aq} = 10$ is much higher. The crystals strongly diverge from an standard barite crystal (Figure 2.11). At a stoichiometry of $r_{aq} = 100$, there is evidence of twinning along the middle of the crystal. This could be a sign of incorporation of NO_3^- ions during growth into the crystal lattice which were replaced at a later moment in time (Klassen-Neklyudova (2012)). Growth is mostly expressed in the [010] direction and some growth in the [100] direction.
If growth kinetics are the underlying reason for changes in morphology, two main factors that can play a role are the diffusion of crystal building ions to the existing crystal and the incorporation, related to adsorption and hydration kinetics, of those ions into the existing crystal. At higher sulphate activities, sulphate assisted desolvation of the barite crystal surface is possible (Piana et al. (2006)), making the incorporation of ions easier. The desolvation of barium is slower than that of sulphate potentially resulting in a very rapid incorperation of the abundant sulphate and a limited incorperation of the sparse barium. At $r_{aq} = 0.01$ and $\Omega = 500$, this maybe leads to very slow growth, resulting in small crystals and would lead to the polar (100) surface to grow as long as it consists of sulphate ions and the (010) surface to grow more quickly than the non-polar (210) surface, which consists of both types of ions. At $r_{aq} = 0.1$ and $\Omega = 500$, the aided desolvation and the slightly higher abundance of barium leads to slightly quicker growth and to the expression of the mixed (210) surface in favor of the (100) surface. This leads to pseudo-rhombohedral crystals. At $r_{aq} = 1$, both ions are similarly likely to be near the surface of the crystal. The incorperation of sulphate is more rapid than of barium, leading to the expression of the (100) surface, consisting of sulphate most likely and growth on the (010) face. This is very different at $r_{aq} = 10$. The growth seems to be almost random. At this stoichiometry, the concentration of sulphate might be too low to assist in the desolvation of the (010) surface, resulting in decreased growth in that direction and thus limiting the elongation along the [010] (b-axis in Figure 2.11). At the (001) surface, barium desolvation might be aided by other anions, promoting a range of growth surfaces, leading to the high variety in crystal shape. An alternative would be, that due to the low concentration of sulphate at $r_{aq} = 10$, other anions are incorporated into the crystal lattice. Depending on the frequency and location of the incorperation, the shape of the final crystal will vary. It has been shown that background ions can greatly influence crystal growth and morphology, varying from attaching to preexisting growth islands to start a new growth row or the formation of stabilized chains, which are less polar than the sulphate and barium bound terraces (Risthaus et al. (2001)). If the lack of sulphate allows more nitrate to attach to preexisting growth islands, this can alter the shape of the final crystal and increase the growth rate. Additionally, barium bound terraces might be bound by stabilized chains before a sulphate was able to bond.
As previously mentioned, there is also the possibility of extensive aggregation at higher barium activity. Aggregation of paticles with different growth histories might be responsible for the large morphological variety observed. This aggregation would be in line with the observations from the DLS, where at $\Omega = 100$ and $r_{aq} = 100$ almost only very large particles were observed in the forward scatter (Figure 4.4 J). There seems to be some hopper crystal formation, as the middle of (100) surface has decreased growth compared to the edges of this plane (Figure 4.4 H). This is likely due to a diffusion limitation of crystal building ions to this surface. Creating a concentration gradient leading to more rapid growth on the edges. This suggests that barium desolvation is

not limiting at this stoichiometry as the crystal building ions do not arrive simultaneously at the surface. This is logical considering the very high stoichiometry and the associated abundance of barium. On the [001], this is very different. The middle seems to grow more rapidly, possible due to desolvation being assisted by other ions here (Piana et al. (2006)) or even incorporation of non-sulphate anions, similar to $r_{aq} = 10$. A potential diffusion limitation is observed at this resolution at $r_{aq} = 100$, due the formation of hopper crystals, and may play a less dominant role at less extreme stoichiometries. This might have an influence on the growth of standard faces at $r_{aq} = 10$. Similar processes to those observed at $\Omega = 500$ might also play a role at $\Omega = 100$. The neutral {210} surfaces consist of alternating barium and sulphate ions whereas the polar {100} planes are either completely composed of barium ions or sulphate ions (Risthaus et al. (2001)). At $r_{aq} = 0.1$, excess sulphate, with rapid desolvation kinetics, potentially increases growth on the (100) surface. The aided desolvation of barium by sulphate, makes the expression of the mixed {210} planes possible, leading to a very standard barium crystal. At $r_{aq} = 1$, many different growth mechanisms seem to occur at this stoichiometry, more akin to what is observed at $\Omega = 500$ and $r_{aq} = 10$. The (210) surface and the (100) surface are never expressed well in the same crystal, indicating that the early stages of crytal formation create a preference. In general, growth occurs more on the (010) surface in favour of the (210), possibly due to promotion of barium desolvation by sulphate, this may be the cause of the greater shape variety. Excess barium has been shown to lead to more rapid growth rates on the (001) surface Kowacz et al. (2007). The step spreading velocity at the (210) surface might also increase, increasing its growth rate and thereby elongating the crystal along the [010] (b-axis in Figure 2.11) as the (210) surface now has the highest growth rate. As barium is present in excess, it is more likely that the (100) plane is composed of barium ions, this could limit its growth due to a limitation in desolvation kinetics and thereby lead to a prismatic crystal with pyramidal points. At the rhomboid crystals, the {100} faces have not developed. This means the {210} planes can freely grow and it not cause the same elongation along the [010] (b-axis in Figure 2.11) and instead also increases the width of the crystal.

At both measured $\Omega's$, higher barium activity leads to larger crystals than higher sulphate activity (Figure 4.1). At $\Omega = 100$, the largest crystals are formed at a stoichiometry of $r_{aq} = 10$ (Figure 4.1 C). This is different at $\Omega = 500$, where the largest crystals are formed at $r_{aq} = 1$. The results from $\Omega = 100$ are in line with earlier research (Kowacz et al. (2007)), also having a growth optimum at slightly higher stoichiometries, and with the data from DLS (Figure 4.4). The DLS data also shows the largest particles at the higher barium activity (Figure 4.4 J). The oversaturation is however much higher than at the experiments of Kowacz et al. (2007). The growth optimum also seems to be at even more extreme stoichiometries than was observed by them. With the largest crystals being observed in the DLS at $r_{aq} = 100$. At $\Omega = 500$, higher barium activity leads to larger crystals than increased sulphate activity but $r_{aq} = 1$ seems to be most optimal for growth (Figure 4.1 F). This means that at $\Omega = 500$, there is a possible break with the earlier trend. From Kowacz et al. (2007), it seems that at higher supersaturations, higher stoichiometry is needed for optimum growth. This trend does not seem to continue to $\Omega = 500$. The supersaturation may be sufficiently high that when the growth solutions are mixed, many critical nucleii form instantaneous. At deviating stoichiometries, these may be charged. This charge, which is either negative when sulphate is abundant or positive when barium is abundant reduces the rate of aggregation and thus decreases final crystal size. Higher barium activity still leads to larger crystals than higher sulphate activity due to the same processes than at $\Omega = 100$ (e.g. higher step edge velocity and increased 2D-nucleation (Kowacz et al. (2007)).

5.5 Recommendations

The exploratory nature of this research leads to a large amount of recommendations. They are divided into chemical parameters variation, experimental set-up and data processing. The ionic strength should be greatly reduced and the background ions should be chosen that they do not interfere with the barium electrode. Additionally, measuring with different background electrolytes would provide insight into the effects of varying background salts. This makes it possible to track the reaction and to measure zeta potential. From this potential, the surface charge of the particles can be calculated. Momentarily, it is unknown if the particles are charged at different stoichiometries and how this affects their behaviour. The second parameter recommendation is to work at higher supersaturations. The large error margin provides an incentive to decrease the time resolution of processes to some extent in favour of higher reproducibility. The reproducibility is expected to increase if the measured volume is more representative. It is more representative due to the higher amount of measured particles. A downside is the potential for even more rapid precipitation. For the experimental set-up, automation is possible, this will increase the amount of measurements that can be performed by and reduces human error. Due to the high data production, critical moments (e.g. changes in growth mode, nucleation speed, nuclei size) can be accurately identified and in flow experiments are recommended for those moments. This will allow for high resolution and statistically valid data of these critical moments. For future studies, faulty measurements should be removed based on expert knowledge and not suppressed by compound graphs, all measurement angles should be presented separately and the transfer from translational diffusion coefficient (D_{trans}) should be made with a custom function for the shapes identified in the SEM experiments. The translation with the equivalent sphere model introduces a margin of error that is undesirable. A titration set-up for the DLS would also be very valuable, as SAXS data for the titration experiment has already been collected. This could lead to a more synergistic approach.

5.6 Societal relevance

The fundamental nature of the research prevents direct applications in society or industry. It does however support coming research in a variety of ways. The lessons learned (Section 5.5) provide vital information for successfully reaching the goals of the Crystal Clear project. The novel synergistic approach of the Crystal Clear project, with the chemical parameters framed by this research and the effectiveness for modifying crystal growth by altering stoichiometry illustrated, will potentially help understanding nucleation in abundant settings such as the ocean (Church and Wolgemuth (1972), Martínez-Ruiz et al. (2019)) and hydrocarbon reservoirs (Sorbie and Mackay (2000)). Additionally it might create understanding of primary production in the oceans of the past (Paytan and Griffith (2007)). This increased understanding might create and array of geo-engineering options to control crystal formation by modifying ionic ratio's instead of adding, potentially harmful, additives. The effects of modifying ionic ratio's are on display in this research and further experimentation, considering the recommendations, may enhance our understanding of crystal nucleation.

5.7 Limitations of the study

The largest limitation is the high degree of uncertainty due to the very high error margin of all results. The averaging of multiple DLS measurements give a robust idea of the trends but increased the standard deviation and removed detail. Additionally, the transfer function used to convert translational diffusive coefficient to size introduces an additional error. The potential effects of local supersaturation cannot be discerned from other processes and the highly dynamic system makes the MADLS calculations problematic. It it not possible to have very high confidence in specific hypotheses put forward in regards to particle population distribution, as no reaction pathways, concentration gradients or energy fluctuations in the system can be discerned from this data. Initial nucleation also occurs outside the timeframe of the DLS measurements, limiting the information that can be obtained regarding the moment of nucleation.

5.7.1 The refractive index and solubility of barite

The size measurements exhibit an additional error from varying refractive index. Different directions through the barite crystal have different refractive indices (ranging between $n_x = 1.6481$ and $n_z = 1.6361$ Vedam (1951)). Because the particle spins randomly in the solution, its refractive index changes. The translation from translational diffusion coefficient to particle size takes refractive index into account. Consequently, the changing refractive index leads to different particle sizes. The effect is however expected to be limited, because the effects average out as long as the particles are relatively symmetrical, due to their random spinning motion and because the difference in refractive index in different directions are limited. The amount of barite particles produced is very low due to the low solubility of barite ($P_{ksp} = 9.97$ Ball and Nordstrom (1991)). This makes the measurement more variable, depending on what is in the analysed volume during the measurement time. At higher particle concentrations, the representativeness of the measurements would have improved, but, the growth processes or changes in population would have been recorded less accurately due to the low time resolution of the MADLS measurements.

Due to the relative nature of the intensity plots, it is unclear if the total amount of particles increases over time. This is however to be expected as the solution is supersaturated in regards to barite and during exploratory measurements, the solution became visibly turbid at very high supersaturations ($\Omega = 5000$) during incubation.

5.7.2 Compound graphs

The compound graphs, where five runs were averaged into one graph, greatly increases the statistical validity of the results but also introduces some key issues. Firstly, it is assumed that all experiments produce exactly the same amount of particles, 15 % of scattered intensity is taken to be the same across experiments for the compound graphs. The key assumption underlying this, is that every repetition of the same experiment produces exactly the same amount of material. This is not true. Secondly, time steps are taken to be simultaneous, the first time-step of experiment one is averaged with the first time step of all other experiments even though the real timing differs (max 1 minute). If more than two measurements were missing, the datapoints were excluded. Trends within one experiment, such as a general increase in size of a highly disperse population might be obscured by a different experiment, which was started slightly later and was potentially coagulating, decreasing the prominence of a certain population at a certain number of time steps. Filtering the data by hand for faulty data is the most accurate way to increase the quality of

the data. In this research however, a simpler approach was followed. Faulty measurements were greatly reduced in their prominence by presenting compound graphs. An important assumption is made when calculating the standard deviation of the graphs. It is assumed the data points are distributed in a Gaussian way. An additional margin of error is introduced into the measurements by MADLS algorithm (Equation 2.13), which assumes that the measurements at all angles are of an unchanging sample and can be treated as simultaneous.

5.7.3 Agreement

There is however an agreement between DLS and SAXS on growth mode at $r_{aq} = 10$. The effects of higher barium activity at $\Omega = 100$ lead to increased growth (SEM) and are in line with earlier research (Kowacz et al. (2007)), this agreement is partially absent at $\Omega = 500$. A stoichiometry of $r_{aq} < 1$ does however still lead to smaller particles at all $\Omega's$, similar to Kowacz et al. (2007)). The agreement between increased growth at higher stoichiometries can also be observed in the DLS measurements at $\Omega = 100$. The same agreement is not observed at $\Omega = 500$. A potential increase of nucleation rate due to a smaller critical nucleus size, possibly related to overcoming the energy barrier for nucleation via kinetics, is also observed. The synergistic approach between DLS, SAXS and SEM points towards nucleation and growth which is aided by more abundant barium. That all the utilized techniques have similar results which are in line with earlier research make the approach promising.

6

Conclusion

The different populations of crystals are established before the DLS measurements start. Only some minor variation due to stoichiometry exist between the established populations. The dominant crystal population is centered around 400nm at all stoichiometries. Particle size evolution suggests that the water exchange kinetics around sulphate are more rapid than around barium, leading to more rapid ion-depletion and decrease of supersaturation. Higher barium than sulphate activity leads to larger crystals at both supersaturations. Possibly due to the slower water exchange kinetics around barium and due to a switch to 2D-nucleation. Overcoming the thermodynamic energy barrier to growth by a kinetic effect. The critical nucleus size is most likely affected by stochiometric variations, with higher stoichiometry leading to lower nucleii size, potentially due to the same kinetic effect. A modification of effective supersaturation in regards nucleation occurs. These observations are similar in most experiments and are in line with previous literature. Crystal shape is strongly affected by stoichiometry. Higher stoichiometry leading to more elongation at $\Omega = 100$ and slight deviations from $r_{aq} = 1$ at $\Omega = 500$ lead to higher variation in particle shape, whereas strong deviations lead to rectangular crystals, similar to $r_{aq} = 1$. The modification of crystal populations potentially has wide ranging consequences for understanding natural and anthropogenic systems. Providing possible, environmentally friendly, solutions to geo-engineering challenges in the hydrocarbon industry and might increase our understanding of ancient ocean productivity.

References

Abraham, F. F. (1974). *Homogeneous nucleation theory*, volume 263. Elsevier.

Ahsan, S. N. and Mallick, K. A. (1999). Geology and genesis of barite deposits of Lasbela and Khuzdar Districts, Balochistan, Pakistan. *Resource Geology*, 49(2):105–111.

Akkurt, I., Akyıldırım, H., Mavi, B., Kilincarslan, S., and Basyigit, C. (2010). Photon attenuation coefficients of concrete includes barite in different rate. *Annals of Nuclear Energy*, 37(7):910–914.

Akkurt, I. and El-Khayatt, A. M. (2013). The effect of barite proportion on neutron and gamma-ray shielding. *Annals of nuclear energy*, 51:5–9.

Albers, W. and Overbeek, J. T. G. (1959). Stability of emulsions of water in oil: Ii. charge as a factor of stabilization against flocculation. *Journal of Colloid Science*, 14(5):510–518.

Alkholidi, A. (2014). *Free Space Optical Communications — Theory and Practices*.

Amorós, J. L. (2012). *The Laue Method*. Elsevier.

Arndt, S., Hetzel, A., and Brumsack, H.-J. (2009). Evolution of organic matter degradation in Cretaceous black shales inferred from authigenic barite: A reaction-transport model. *Geochimica et Cosmochimica Acta*, 73(7):2000–2022.

Baken, A. (2020). Msc. thesis.

Bale, H. D. and Schmidt, P. W. (1984). Small-angle X-ray-scattering investigation of submicroscopic porosity with fractal properties. *Physical Review Letters*, 53(6):596.

Balerna, A. and Mobilio, S. (2015). Introduction to synchrotron radiation. In *Synchrotron radiation*, pages 3–28. Springer.

Ball, J. W. and Nordstrom, D. K. (1991). User's manual for WATEQ4F, with revised thermodynamic data base and test cases for calculating speciation of major, trace, and redox elements in natural waters.

Barna, S. L., Tate, M. W., Gruner, S. M., and Eikenberry, E. F. (1999). Calibration procedures for charge-coupled device x-ray detectors. *Review of Scientific Instruments*, 70(7):2927–2934.

Bergmann, R. B. and Bill, A. (2008). On the origin of logarithmic-normal distributions: An analytical derivation, and its application to nucleation and growth processes. *Journal of Crystal Growth*, 310(13):3135–3138.

Besra, L. and Liu, M. (2007). A review on fundamentals and applications of electrophoretic deposition (epd). *Progress in materials science*, 52(1):1–61.

Bhattacharjee, S. (2016). Dls and zeta potential–what they are and what they are not? *Journal of Controlled Release*, 235:337–351.

BinMerdhah, A. B., Yassin, A. A. M., and Muherei, M. A. (2010). Laboratory and prediction of barium sulfate scaling at high-barium formation water. *Journal of Petroleum Science and Engineering*, 70(1-2):79–88.

Boland, M., LeBlanc, G., Peake, D., and Rassool, R. (2007). Preliminary studies for top-up operations at the australian synchrotron. In *2007 IEEE Particle Accelerator Conference (PAC)*, pages 3856–3858. IEEE.

Born, M. and Wolf, E. (2013). *Principles of optics: electromagnetic theory of propagation, interference and diffraction of light*. Elsevier.

Bösecke, P. and Diat, O. (1997). Small-angle X-ray scattering at the ESRF high-brilliance beamline. *Journal of Applied Crystallography*, 30(5):867–871.

Bracco, J. N., Grantham, M. C., and Stack, A. G. (2012). Calcite growth rates as a function of aqueous calcium-to-carbonate ratio, saturation index, and inhibitor concentration: Insight into the mechanism of reaction and poisoning by strontium. *Crystal growth & design*, 12(7):3540–3548.

Bryant, G. and Thomas, J. C. (1995). Improved particle size distribution measurements using multiangle dynamic light scattering. *Langmuir*, 11(7):2480–2485.

Burton, W.-K., Cabrera, N., and Frank, F. C. (1951). The growth of crystals and the equilibrium structure of their surfaces. *Philosophical Transactions of the Royal Society of London. Series A, Mathematical and Physical Sciences*, 243(866):299–358.

Chaikin, P. M., Lubensky, T. C., and Witten, T. A. (1995). *Principles of condensed matter physics*, volume 10. Cambridge university press Cambridge.

Changizi, V., Kheradmand, A. A., and Oghabian, M. (2007). Application of small angle x-ray scattering in differentiation among beast tumors. In *World Congress on Medical Physics and Biomedical Engineering 2006*, pages 1357–1358. Springer.

Chattopadhyay, S., Erdemir, D., Evans, J. M. B., Ilavsky, J., Amenitsch, H., Segre, C. U., and Myerson, A. S. (2005). SAXS study of the nucleation of glycine crystals from a supersaturated solution. *Crystal growth & design*, 5(2):523–527.

Chernov, A. (2004). Notes on interface growth kinetics 50 years after burton, cabrera and frank. *Journal of Crystal Growth*, 264(4):499–518.

Chernov, A., Petrova, E., and Rashkovich, L. (2006). Dependence of the caox and mgox growth rate on solution stoichiometry. non-kossel crystal growth. *Journal of crystal growth*, 289(1):245–254.

Chernov, A. A. (1961). The spiral growth of crystals. *Soviet Physics Uspekhi*, 4(1):116.

Chong, S.-H. and Hirata, F. (1997). Ion hydration: Thermodynamic and structural analysis with an integral equation theory of liquids. *The Journal of Physical Chemistry B*, 101(16):3209–3220.

Christy, A. G. and Putnis, A. (1993). The kinetics of barite dissolution and precipitation in water and sodium chloride brines at 44–85 c. *Geochimica et Cosmochimica Acta*, 57(10):2161–2168.

Church, T. M. and Wolgemuth, K. (1972). Marine barite saturation. *Earth and Planetary Science Letters*, 15(1):35–44.

Cicerone, D. S., Regazzoni, A. E., and Blesa, M. A. (1992). Electrokinetic properties of the calcite/water interface in the presence of magnesium and organic matter. *Journal of Colloid and Interface Science*, 154(2):423–433.

Cölfen, H. (2010). A crystal-clear view. *Nature materials*, 9(12):960–961.

Cölfen, H. and Mann, S. (2003). Higher-order organization by mesoscale self-assembly and transformation of hybrid nanostructures. *Angewandte Chemie International Edition*, 42(21):2350–2365.

Collins, I. R. (2005). Predicting the location of barium sulfate scale formation in production systems. In *SPE International Symposium on Oilfield Scale*. Society of Petroleum Engineers.

Corsi, R. (1986). Scaling and corrosion in geothermal equipment: problems and preventive measures. *Geothermics*, 15(5-6):839–856.

Crabtree, M., Eslinger, D., Fletcher, P., Miller, M., Johnson, A., and King, G. (1999). Fighting scale—removal and prevention. *Oilfield review*, 11(3):30–45.

Cummins, P. G. and Staples, E. J. (1987). Particle size distributions determined by a" multiangle" analysis of photon correlation spectroscopy data. *Langmuir*, 3(6):1109–1113.

Davies, C., Association, I., et al. (1962). pp. 37–53.

Davies, C. and Jones, A. (1949). The precipitation of silver chloride from aqueous solutions. part i. *Discussions of the Faraday Society*, 5:103–111.

Davies, C. W. (1938). 397. the extent of dissociation of salts in water. part viii. an equation for the mean ionic activity coefficient of an electrolyte in water, and a revision of the dissociation constants of some sulphates. *Journal of the Chemical Society (Resumed)*, pages 2093–2098.

de Boer, G. B., de Weerd, C., Thoenes, D., and Goossens, H. W. (1987). Laser diffraction spectrometry: Fraunhofer diffraction versus mie scattering. *Particle & Particle Systems Characterization*, 4(1-4):14–19.

De Yoreo, J. J. and Vekilov, P. G. (2003). Principles of crystal nucleation and growth. *Reviews in mineralogy and geochemistry*, 54(1):57–93.

Delshad, M., Pope, G. A., et al. (2003). Effect of dispersion on transport and precipitation of barium and sulfate in oil reservoirs. In *International Symposium on Oilfield Chemistry*. Society of Petroleum Engineers.

Denisov, E., Sarkisov, O., and Likhtenshtein, G. (2003). Chapter 8 - reactions of ions and radical ions. In Denisov, E., Sarkisov, O., and Likhtenshtein, G., editors, *Chemical Kinetics*, pages 250 – 304. Elsevier Science, Amsterdam.

Deschamps, A. and De Geuser, F. (2011). On the validity of simple precipitate size measurements by small-angle scattering in metallic systems. *Journal of Applied Crystallography*, 44(2):343–352.

Deshler, T. (2015). Chemistry of the atmosphere — observations for chemistry (in situ): Particles. In North, G. R., Pyle, J., and Zhang, F., editors, *Encyclopedia of Atmospheric Sciences (Second Edition)*, pages 379 – 386. Academic Press, Oxford, second edition edition.

Di Tommaso, D. and De Leeuw, N. H. (2010). First principles simulations of the structural and dynamical properties of hydrated metal ions Me2+ and solvated metal carbonates (Me = Ca, Mg, and Sr). *Crystal Growth and Design*, 10(10):4292–4302.

Doane, T. L., Chuang, C.-H., Hill, R. J., and Burda, C. (2012). Nanoparticle ζ-potentials. *Accounts of chemical research*, 45(3):317–326.

Domingos, R. F., Baalousha, M. A., Ju-Nam, Y., Reid, M. M., Tufenkji, N., Lead, J. R., Leppard, G. G., and Wilkinson, K. J. (2009). Characterizing manufactured nanoparticles in the environment: multimethod determination of particle sizes. *Environmental science & technology*, 43(19):7277–7284.

DOOLEY, C. P., LARSON, A. W., STACE, N. H., RENNER, I. A. N. G., VALENZUELA, J. E., ELIASOPH, J., COLLETTI, P. M., HALLS, J. M., and WEINER, J. M. (1984). Double-contrast barium meal and upper gastrointestinal endoscopy: a comparative study. *Annals of internal medicine*, 101(4):538–545.

Dove, P. M. and Czank, C. A. (1995). Crystal chemical controls on the dissolution kinetics of the isostructural sulfates: Celestite, anglesite, and barite. *Geochimica et Cosmochimica Acta*, 59(10):1907–1915.

Dreiss, C. A., Jack, K. S., and Parker, A. P. (2006). On the absolute calibration of bench-top small-angle X-ray scattering instruments: a comparison of different standard methods. *Journal of applied crystallography*, 39(1):32–38.

Duke, P. (2009). *Synchrotron radiation: production and properties*, volume 3. Oxford University Press.

Dyer, S. J. and Graham, G. M. (2002). The effect of temperature and pressure on oilfield scale formation. *Journal of Petroleum Science and Engineering*, 35(1-2):95–107.

Eagle, M., Paytan, A., Arrigo, K. R., van Dijken, G., and Murray, R. W. (2003). A comparison between excess barium and barite as indicators of carbon export. *Paleoceanography*, 18(1).

Earnshaw, S. (1842). On the nature of the molecular forces. In *Cambridge Philosophical Society*, volume 7, pages 97–112.

Eikenberry, E. F., Brönnimann, C., Hülsen, G., Toyokawa, H., Horisberger, R., Schmitt, B., Schulze-Briese, C., and Tomizaki, T. (2003). PILATUS: a two-dimensional X-ray detector for macromolecular crystallography. *Nuclear Instruments and Methods in Physics Research Section A: Accelerators, Spectrometers, Detectors and Associated Equipment*, 501(1):260–266.

Einstein, A. et al. (1905). On the motion of small particles suspended in liquids at rest required by the molecular-kinetic theory of heat. *Annalen der physik*, 17(549-560):208.

Eriksson, E. (1985). *Principles and applications of hydrochemistry*, volume 187. Springer.

Fairhurst, D. (2012). Overview of zeta potential concept, measurement use, and applications.

Farkas, L. (1927). The velocity of nucleus formation in supersaturated vapors. *Z. Phys. Chemie*, 125:236.

Fernandez-Diaz, L., Putnis, A., and Cumberbatch, T. J. (1990). Barite nucleation kinetics and the effect of additives. *European Journal of Mineralogy*, pages 495–502.

Filobelo, L. F., Galkin, O., and Vekilov, P. G. (2005). Spinodal for the solution-to-crystal phase transformation. *The Journal of chemical physics*, 123(1):14904.

Fokin, V. M. and Zanotto, E. D. (2000). Crystal nucleation in silicate glasses: the temperature and size dependence of crystal/liquid surface energy. *Journal of Non-Crystalline Solids*, 265(1-2):105–112.

Forchhammer, G. (1865). Iv. on the composition of sea-water in the different parts of the ocean. *Philosophical Transactions of the Royal Society of London*, (155):203–262.

Fritts, C. E. (1962). *The barite mines of Cheshire*. Cheshire Historical Society.

Fuerstenau, D., Herrera-Urbina, R., et al. (1992). The surface chemistry of bastnaesite, barite and calcite in aqueous carbonate solutions. *Colloids and surfaces*, 68(1-2):95–102.

García-Ruiz, J. M. and Otálora, F. (2015). Crystal growth in geology: patterns on the rocks. In *Handbook of crystal growth*, pages 1–43. Elsevier.

Gebauer, D., Völkel, A., and Cölfen, H. (2008). Stable prenucleation calcium carbonate clusters. *Science*, 322(5909):1819–1822.

Georgalis, Y., Umbach, P., Raptis, J., and Saenger, W. (1997). Lysozyme aggregation studied by light scattering. I. Influence of concentration and nature of electrolytes. *Acta Crystallographica Section D: Biological Crystallography*, 53(6):691–702.

Gibbs, J. W. (1878). On the equilibrium of heterogeneous substances. *American Journal of Science*, (96):441–458.

Gillikin, D. P., Dehairs, F., Lorrain, A., Steenmans, D., Baeyens, W., and André, L. (2006). Barium uptake into the shells of the common mussel (Mytilus edulis) and the potential for estuarine paleo-chemistry reconstruction. *Geochimica et Cosmochimica Acta*, 70(2):395–407.

Gingele, F. and Dahmke, A. (1994). Discrete barite particles and barium as tracers of paleoproductivity in South Atlantic sediments. *Paleoceanography*, 9(1):151–168.

Ginzburg, V. and Syrovatskii, S. (1965). Cosmic magnetobremsstrahlung (synchrotron radiation). *Annual Review of Astronomy and Astrophysics*, 3(1):297–350.

Glatter, O. (1980). Determination of particle-size distribution functions from small-angle scattering data by means of the indirect transformation method. *Journal of Applied Crystallography*, 13(1):7–11.

Glenzer, S. H. and Redmer, R. (2009). X-ray thomson scattering in high energy density plasmas. *Reviews of Modern Physics*, 81(4):1625.

Godinho, J. R. and Stack, A. G. (2015). Growth kinetics and morphology of barite crystals derived from face-specific growth rates. *Crystal Growth & Design*, 15(5):2064–2071.

Gruen, D. W. and Marčelja, S. (1983). Spatially varying polarization in water. a model for the electric double layer and the hydration force. *Journal of the Chemical Society, Faraday Transactions 2: Molecular and Chemical Physics*, 79(2):225–242.

Guinier, A. (1939). Diffraction of x-rays of very small angles-application of ultramicroscopic phenomenon. *Ann. Phys.*, 12:161.

Guinier, A., Fournet, G., and Yudowitch, K. L. (1955). Small-angle scattering of X-rays.

Gustafsson, P. (2006). Visual minteq version 3.0. department of land and water resources engineering, stockholm, sweden.

Haas, C. and Drenth, J. (2000). The interface between a protein crystal and an aqueous solution and its effects on nucleation and crystal growth. *The Journal of Physical Chemistry B*, 104(2):368–377.

Hackley, V. and Clogston, J. (2007). Measuring the size of nanoparticles in aqueous media using batch-mode dynamic light scattering. *NIST special publication*, 1200:6.

Hallett, F. R. (1999). *Scattering and Particle Sizing, Applications*. Elsevier, Oxford.

Hanaor, D., Michelazzi, M., Veronesi, P., Leonelli, C., Romagnoli, M., and Sorrell, C. (2011). Anodic aqueous electrophoretic deposition of titanium dioxide using carboxylic acids as dispersing agents. *Journal of the European Ceramic Society*, 31(6):1041–1047.

Hang, J. Z., Zhang, Y. F., Shi, L. Y., and Feng, X. (2007). Electrokinetic properties of barite nanoparticles suspensions in different electrolyte media. *Journal of Materials Science*, 42(23):9611–9616.

Hanor, J. S. (2000). Barite–celestine geochemistry and environments of formation. *Reviews in Mineralogy and Geochemistry*, 40(1):193–275.

Haranas, I., Gkigkitzis, I., and Zouganelis, G. D. (2012). g dependent particle concentration due to sedimentation. *Astrophysics and Space Science*, 342(1):31–43.

Hellevang, H., Haile, B. G., and Miri, R. (2016). A Statistical Approach To Explain the Solution Stoichiometry Effect on Crystal Growth Rates. *Crystal Growth & Design*, 16(3):1337–1348.

Hellevang, H., Miri, R., and Haile, B. G. (2014). New insights into the mechanisms controlling the rate of crystal growth. *Crystal growth & design*, 14(12):6451–6458.

Hillner, P., Manne, S., Gratz, A., and Hansma, P. (1992). AFM images of dissolution and growth on a calcite crystal. *Ultramicroscopy*, 42-44:1387–1393.

Hohenberg, P. C. and Halperin, B. I. (1977). Theory of dynamic critical phenomena. *Reviews of Modern Physics*, 49(3):435.

Hosse, M. and Wilkinson, K. J. (2001). Determination of electrophoretic mobilities and hydrodynamic radii of three humic substances as a function of ph and ionic strength. *Environmental science & technology*, 35(21):4301–4306.

Hribar, B., Southall, N. T., Vlachy, V., and Dill, K. A. (2002). How ions affect the structure of water. *Journal of the American Chemical Society*, 124(41):12302–12311.

Hübschen, G., Altpeter, I., Tschuncky, R., and Herrmann, H.-G. (2016). *Materials characterization using nondestructive evaluation (NDE) methods*. Woodhead Publishing.

Hulst, H. C. and van de Hulst, H. C. (1981). *Light scattering by small particles*. Courier Corporation.

Hunter, R. J. (1993). *Introduction to modern colloid science*, volume 7. Oxford University Press Oxford.

Hunter, R. J. (2013). *Zeta potential in colloid science: principles and applications*, volume 2. Academic press.

Jewell, P. W. and Stallard, R. F. (1991). Geochemistry and paleoceanographic setting of central Nevada bedded barites. *The Journal of Geology*, 99(2):151–170.

Jones, F., Piana, S., and Gale, J. (2008). Understanding the kinetics of barium sulfate precipitation from water and water–methanol solutions. *Crystal Growth and Design*, 8(3):817–822.

Jordan, M. M., Sjuraether, K., Collins, I. R., Feasey, N. D., and Emmons, D. (2001). Life cycle management of scale control within subsea fields and its impact on flow assurance, Gulf of Mexico and the North Sea basin. *SPE Annual Technical Conference and Exhibition*.

Kalikmanov, V. I. (2013). Classical nucleation theory. In *Nucleation theory*, pages 17–41. Springer.

Kalyanaraman, R. (2008). Nucleation energetics during homogeneous solidification in elemental metallic liquids. *Journal of Applied Physics*, 104(3):033506.

Karatzas, I. and Shreve, S. E. (1998). Brownian motion. In *Brownian Motion and Stochastic Calculus*, pages 47–127. Springer.

Kashchiev, D. (2000). *Nucleation*. Elsevier.

Keefer, K. D. and Schaefer, D. W. (1986). Growth of fractally rough colloids. *Physical review letters*, 56(22):2376.

Kitamura, M. (2002). Controlling factor of polymorphism in crystallization process. *Journal of Crystal Growth*, 237:2205–2214.

Klassen-Neklyudova, M. V. (2012). *Mechanical twinning of crystals*. Springer Science & Business Media.

Klein, C. and Hurlbut, C. (1985). Jr, manual of mineralogy, 20" ed.

Klimchitskaya, G. L. and Mostepanenko, V. M. (2015). Casimir and van der waals forces: Advances and problems. *arXiv preprint arXiv:1507.02393*.

Koch, M. H. J. (2010). SAXS Instrumentation for Synchrotron Radiation then and now. In *Journal of Physics: Conference Series*, volume 247, page 12001. IOP Publishing.

Koneshan, S., Rasaiah, J. C., Lynden-Bell, R. M., and Lee, S. H. (1998). Solvent structure, dynamics, and ion mobility in aqueous solutions at 25 °C. *Journal of Physical Chemistry B*, 102(21):4193–4204.

Koskamp, J. A., Ruiz-Hernandez, S. E., Di Tommaso, D., Elena, A. M., De Leeuw, N. H., and Wolthers, M. (2019). Reconsidering calcium dehydration as the rate-determining step in calcium mineral growth. *The Journal of Physical Chemistry C*, 123(44):26895–26903.

Kowacz, M., Prieto, M., and Putnis, A. (2010). Kinetics of crystal nucleation in ionic solutions: Electrostatics and hydration forces. *Geochimica et Cosmochimica Acta*, 74(2):469–481.

Kowacz, M. and Putnis, A. (2008). The effect of specific background electrolytes on water structure and solute hydration: Consequences for crystal dissolution and growth. *Geochimica et Cosmochimica Acta*, 72(18):4476–4487.

Kowacz, M., Putnis, C. V., and Putnis, A. (2007). The effect of cation: anion ratio in solution on the mechanism of barite growth at constant supersaturation: role of the desolvation process on the growth kinetics. *Geochimica et cosmochimica acta*, 71(21):5168–5179.

Kresse, R., Baudis, U., Jäger, P., Riechers, H. H., Wagner, H., Winkler, J., and Wolf, H. U. (2000). Barium and barium compounds. *Ullmann's encyclopedia of industrial chemistry*.

Kügler, R. T., Beißert, K., and Kind, M. (2016). On heterogeneous nucleation during the precipitation of barium sulfate. *Chemical Engineering Research and Design*, 114:30–38.

Kuipers, B. (2020a). Detailed knowledge of correlation.

Kuipers, B. (2020b). Introduction dynamic light scattering theory.

Kuipers, B. (2020c). Model-independent particle size distribution (psd) from light scattering.

Kumar, A. and Dixit, C. K. (2017). 3 - methods for characterization of nanoparticles. In Nimesh, S., Chandra, R., and Gupta, N., editors, *Advances in Nanomedicine for the Delivery of Therapeutic Nucleic Acids*, pages 43 – 58. Woodhead Publishing.

Kvick, Å. (1999). Materials Science Applications of X-ray diffraction.

Laaksonen, A. and Napari, I. (2001). Breakdown of the capillarity approximation in binary nucleation: a density functional study. *The Journal of Physical Chemistry B*, 105(47):11678–11682.

Lakowicz, J. R. (2013). *Principles of fluorescence spectroscopy*. Springer Science & Business Media.

Larsen, K., Bechgaard, K., and Stipp, S. L. S. (2010). The effect of the ca2+ to co32-activity ratio on spiral growth at the calcite {101¯ 4} surface. *Geochimica et Cosmochimica Acta*, 74(7):2099–2109.

Lawson, C. L. and Hanson, R. J. (1995). *Solving least squares problems*, volume 15. Siam.

Lee, S. H. and Rasaiah, J. C. (1994). Molecular dynamics simulation of ionic mobility. i. alkali metal cations in water at 25 c. *The Journal of chemical physics*, 101(8):6964–6974.

Letterman, R. D., Association, A. W. W., et al. (1999). *Water quality and treatment*. McGraw-Hill,.

Li], S. K., Hao, J., and Liddell, M. (2013). *Chapter 11 - Electrotransport Across Membranes in Biological Media: Electrokinetic Theories and Applications in Drug Delivery*. Elsevier, Boston.

Li, Y. and Ishigaki, T. (2002). Thermodynamic analysis of nucleation of anatase and rutile from tio2 melt. *Journal of Crystal Growth*, 242(3-4):511–516.

Liao, D., Wu, G., and Liao, B. (2009). Zeta potential of shape-controlled tio2 nanoparticles with surfactants. *Colloids and Surfaces A: Physicochemical and Engineering Aspects*, 348(1-3):270–275.

Lin, D.-Q., Brixius, P. J., Hubbuch, J. J., Thömmes, J., and Kula, M.-R. (2003). Biomass/adsorbent electrostatic interactions in expanded bed adsorption: a zeta potential study. *Biotechnology and bioengineering*, 83(2):149–157.

Liu, J., Nicholson, C. E., and Cooper, S. J. (2007). Direct measurement of critical nucleus size in confined volumes. *Langmuir*, 23(13):7286–7292.

Lynden-Bell, R., Rasaiah, J., and Noworyta, J. (2001). Using simulation to study solvation in water. *Pure and applied chemistry*, 73(11):1721–1731.

Martínez-Ruiz, F., Paytan, A., Gonzalez-Muñoz, M., Jroundi, F., Abad, M. d. M., Lam, P. J., Bishop, J., Horner, T., Morton, P. L., and Kastner, M. (2019). Barite formation in the ocean: Origin of amorphous and crystalline precipitates. *Chemical Geology*, 511:441–451.

Matynia, A., Piotrowski, K., Koralewska, J., and Wierzbowska, B. (2004). Barium sulfate crystallization kinetics in the used quenching salts treatment process. *Chemical Engineering and Technology*, 27(5):559–568.

Mavredaki, E., Neville, A., and Sorbie, K. S. (2011). Initial stages of barium sulfate formation at surfaces in the presence of inhibitors. *Crystal growth & design*, 11(11):4751–4758.

Meldrum, F. C. and Sear, R. P. (2008). Now you see them. *Science*, 322(5909):1802–1803.

Merdhah, A. B. B. and Yassin, A. A. M. (2007). Barium sulfate scale formation in oil reservoir during water injection at high-barium formation water. *J. Appl. Sci*, 7(17):2393–2403.

Mitchell, R. F., Ravi, K., and Pgs, H. (2006). Volume II: Drilling Engineering. *Petroleum Engineering Handbook; Lake, LW, Ed.; Society of Petroleum Engineers: Richardson, TX*.

Motz, H. (1951). Applications of the radiation from fast electron beams. *Journal of Applied Physics*, 22(5):527–535.

Murthy, N. S. (2013). Scattering techniques for structural analysis of biomaterials. In *Characterization of Biomaterials*, pages 34–72. Elsevier.

Nehrke, G. (2007). *Calcite precipitation from aqueous solution: transformation from vaterite and role of solution stoichiometry*. PhD thesis, UU Dept. of Earth Sciences.

Nehrke, G., Reichart, G.-J., Van Cappellen, P., Meile, C., and Bijma, J. (2007). Dependence of calcite growth rate and Sr partitioning on solution stoichiometry: non-Kossel crystal growth. *Geochimica et Cosmochimica Acta*, 71(9):2240–2249.

Nielsen, A. E. (1964). *Kinetics of precipitation*, volume 18. Pergamon.

Nielsen, A. E. (1984). Electrolyte crystal growth mechanisms. *Journal of Crystal Growth*, 67(2):289–310.

Ogino, T., Suzuki, T., and Sawada, K. (1987). The formation and transformation mechanism of calcium carbonate in water. *Geochimica et Cosmochimica Acta*, 51(10):2757–2767.

Pauw, B. R. (2011a). How to do a perfect SAXS measurement.

Pauw, B. R. (2011b). The impossible project" - how to do a perfect saxs measurement.

Pauw, B. R. (2013). Everything saxs: small-angle scattering pattern collection and correction. *Journal of Physics: Condensed Matter*, 25(38):383201.

Paytan, A. and Griffith, E. M. (2007). Marine barite: Recorder of variations in ocean export productivity. *Deep Sea Research Part II: Topical Studies in Oceanography*, 54(5-7):687–705.

Paytan, A., Kastner, M., and Chavez, F. P. (1996). Glacial to interglacial fluctuations in productivity in the equatorial Pacific as indicated by marine barite. *Science*, 274(5291):1355–1357.

Paytan, A., Kastner, M., Martin, E. E., MacDougall, J. D., and Herbert, T. (1993). Marine barite as a monitor of seawater strontium isotope composition. *Nature*, 366(6454):445–449.

Pecora, R. (2000). Dynamic light scattering measurement of nanometer particles in liquids. *Journal of nanoparticle research*, 2(2):123–131.

Penn, R. L. and Soltis, J. A. (2014). Characterizing crystal growth by oriented aggregation. *CrystEngComm*, 16(8):1409–1418.

Perdikouri, C., Putnis, C. V., Kasioptas, A., and Putnis, A. (2009). An atomic force microscopy study of the growth of a calcite surface as a function of calcium/total carbonate concentration ratio in solution at constant supersaturation. *Crystal growth & design*, 9(10):4344–4350.

Petsev, D. N., Chen, K., Gliko, O., and Vekilov, P. G. (2003). Diffusion-limited kinetics of the solution–solid phase transition of molecular substances. *Proceedings of the National Academy of Sciences*, 100(3):792–796.

Peyvandi, K., Haghtalab, A., and Omidkhah, M. R. (2012). Using an electrochemical technique to study the effective variables on morphology and deposition of CaCO3 and BaSO4 at the metal surface. *Journal of crystal growth*, 354(1):109–118.

Piana, S., Jones, F., and Gale, J. (2007). Aspartic acid as a crystal growth catalyst. *CrystEngComm*, 9(12):1187–1191.

Piana, S., Jones, F., and Gale, J. D. (2006). Assisted desolvation as a key kinetic step for crystal growth. *Journal of the American Chemical Society*, 128(41):13568–13574.

Piatt, M. (2016). Single-particle zeta potential - is it more than just a number?

Pina, C. M., Becker, U., Risthaus, P., Bosbach, D., and Putnis, A. (1998). Molecular-scale mechanisms of crystal growth in barite. *Nature*, 395(6701):483–486.

Pont, M., Moldes, J., Benedetti, G., Pérez, F., Muñoz Horta, R., and Olmos, A. (2014). Top-up operation at alba synchrotron light source.

Pontoni, D., Narayanan, T., and Rennie, A. R. (2004). *Nucleation and growth kinetics of colloidal silica*. Springer Berlin Heidelberg, Berlin, Heidelberg.

Porter, D. A., Easterling, K. E., and Sherif, M. (2009). *Phase transformations in metals and alloys (Revised Reprint)*. CRC press.

Provencher, S. W. (1982). A constrained regularization method for inverting data represented by linear algebraic or integral equations. *Computer Physics Communications*, 27(3):213–227.

Rabia, H. (1985). *Oilwell drilling engineering: principles and practice*. Springer.

Raghu, V. (2001). Accumulation of elements in plants and soils in and around mangampeta and vemula barite mining areas, cuddapah district, andhra pradesh, india. *Environmental Geology*, 40(10):1265–1277.

Read, P. A., Ringen, J. K., et al. (1982). The use of laboratory tests to evaluate scaling problems during water injection. In *SPE Oilfield and Geothermal Chemistry Symposium*. Society of Petroleum Engineers.

Reintjes, J. (2012). *Nonlinear optical parametric processes in liquids and gases*. Elsevier.

Reklaitis, G. V., Seymour, C., and García-Munoz, S. (2017). *Comprehensive Quality by Design for Pharmaceutical Product Development and Manufacture*. John Wiley & Sons.

Risthaus, P., Bosbach, D., Becker, U., and Putnis, A. (2001). Barite scale formation and dissolution at high ionic strength studied with atomic force microscopy. *Colloids and Surfaces A: Physicochemical and Engineering Aspects*, 191(3):201–214.

Rugar, D. and Hansma, P. (1990). Atomic force microscopy. *Physics today*, 43(10):23–30.

Ruiz-Agudo, C., Putnis, C. V., Ruiz-Agudo, E., and Putnis, A. (2015). The influence of ph on barite nucleation and growth. *Chemical Geology*, 391:7–18.

Ruseva, V., Lyons, M., Powell, J., Austin, J., Malm, A., and Corbett, J. (2018). Capillary dynamic light scattering: Continuous hydrodynamic particle size from the nano to the microscale. *Colloids and Surfaces A: Physicochemical and Engineering Aspects*, 558:504–511.

Salgin, S., Salgin, U., and Bahadir, S. (2012). Zeta potentials and isoelectric points of biomolecules: the effects of ion types and ionic strengths. *Int. J. Electrochem. Sci*, 7(12):12404–12414.

Schnablegger, H. and Singh, Y. (2011). The SAXS guide: getting acquainted with the principles. *Austria: Anton Paar GmbH*, pages 1–124.

Seinfeld, J. H. and Pandis, S. N. (2016). *Atmospheric chemistry and physics: from air pollution to climate change*. John Wiley & Sons.

Sharaf, M. A. and Dobbins, R. A. (1982). A comparison of measured nucleation rates with the predictions of several theories of homogeneous nucleation. *The Journal of chemical physics*, 77(3):1517–1526.

Shenoy, G. (2003). Basic characteristics of synchrotron radiation. *Structural Chemistry*, 14(1):3–14.

Söhnel, O. (1982). Electrolyte crystal-aqueous solution interfacial tensions from crystallization data. *Journal of Crystal Growth*, 57(1):101–108.

Somasundaran, P. (2006). *Encyclopedia of surface and colloid science*, volume 2. CRC press.

Sorbie, K. and Mackay, E. (2000). Mixing of injected, connate and aquifer brines in waterflooding and its relevance to oilfield scaling. *Journal of Petroleum Science and Engineering*, 27(1-2):85–106.

Sosa, R. D., Geng, X., Reynolds, M. A., Rimer, J. D., and Conrad, J. C. (2019). A microfluidic approach for probing hydrodynamic effects in barite scale formation. *Lab on a Chip*, 19(9):1534–1544.

Stack, A. G., Raiteri, P., and Gale, J. D. (2012). Accurate rates of the complex mechanisms for growth and dissolution of minerals using a combination of rare-event theories. *Journal of the American Chemical Society*, 134(1):11–14.

Stanton, M. R. (1996). *Dissolved radon and uranium, and ground-water geochemistry in an area near Hylas, Virginia*, volume 2070. US Government Printing Office.

Stetefeld, J., McKenna, S. A., and Patel, T. R. (2016). Dynamic light scattering: a practical guide and applications in biomedical sciences. *Biophysical reviews*, 8(4):409–427.

Strey, R., Wagner, P., and Viisanen, Y. (1994). The problem of measuring homogeneous nucleation rates and the molecular contents of nuclei: progress in the form of nucleation pulse measurements. *The Journal of Physical Chemistry*, 98(32):7748–7758.

Stroobants, N., Dehairs, F., Goeyens, L., Vanderheijden, N., and Van Grieken, R. (1991). Barite formation in the Southern Ocean water column. *Marine Chemistry*, 35(1-4):411–421.

Stuckey, J. L. and Davis, H. T. (1933). *Barite deposits in North Carolina*. American Institute of Mining and Metallurgical Engineers, Incorporated.

Sun, A. C. and Seider, W. D. (1995). Homotopy-continuation method for stability analysis in the global minimization of the gibbs free energy. *Fluid Phase Equilibria*, 103(2):213–249.

Sunagawa, I. (2007). *Crystals: growth, morphology, & perfection*. Cambridge University Press.

Sze, A., Erickson, D., Ren, L., and Li, D. (2003). Zeta-potential measurement using the smoluchowski equation and the slope of the current–time relationship in electroosmotic flow. *Journal of colloid and interface science*, 261(2):402–410.

Talanquer, V. and Oxtoby, D. W. (1998). Crystal nucleation in the presence of a metastable critical point. *The Journal of chemical physics*, 109(1):223–227.

Tanaka, H., Adachi, M., Aoki, T., Asaka, T., Baron, A., Fukami, K., Furukawa, Y., Hanaki, H., Hosoda, N., Ishikawa, T., et al. (2006). Stable top-up operation at spring-8. *Journal of synchrotron radiation*, 13(5):378–391.

ten Wolde, P. R. and Frenkel, D. (2016). Enhancement of Protein Crystal Nucleation by Critical Density Fluctuations Author (s): Pieter Rein ten Wolde and Daan Frenkel Published by : American Association for the Advancement of Science Stable URL : http://www.jstor.org/stable/2893889 REFERENCES. *Science*, 277(5334):1975–1978.

Teng, H. H., Dove, P. M., and De Yoreo, J. J. (2000). Kinetics of calcite growth: surface processes and relationships to macroscopic rate laws. *Geochimica et Cosmochimica Acta*, 64(13):2255–2266.

Tomson, M. B., Kan, A. T., and Fu, G. (2004a). Inhibition of barite scale in the presence of hydrate inhibitors. In *SPE International Symposium on Oilfield Scale*. Society of Petroleum Engineers.

Tomson, M. B., Kan, A. T., Fu, G., et al. (2004b). Inhibition of barite scale in the presence of hydrate inhibitors. In *SPE International Symposium on Oilfield Scale*. Society of Petroleum Engineers.

Tuckerman, M., Laasonen, K., Sprik, M., and Parrinello, M. (1995). Ab initio molecular dynamics simulation of the solvation and transport of hydronium and hydroxyl ions in water. *The Journal of chemical physics*, 103(1):150–161.

Uemura, Y., Fujimura, M., Hashimoto, T., and Kawai, H. (1978). Application of light scattering from dielectric cylinder based upon mie and rayleigh—gans—born theories to polymer systems. i. scattering from a glass fiber. *Polymer Journal*, 10(3):341–351.

Van Der Weijden, C. and Van Der Weijden, R. (2014). Calcite growth: Rate dependence on saturation, on ratios of dissolved calcium and (bi) carbonate and on their complexes. *Journal of crystal growth*, 394:137–144.

Vazirian, M. M., Charpentier, T. V., de Oliveira Penna, M., and Neville, A. (2016). Surface inorganic scale formation in oil and gas industry: As adhesion and deposition processes. *Journal of Petroleum Science and Engineering*, 137:22–32.

Vedam, K. (1951). Photoelastic properties of barite. In *Proceedings of the Indian Academy of Sciences-Section A*, volume 34, page 161. Springer India.

Volmer, M. and Weber, A. (1926). Keimbildung in übersättigten gebilden. *Zeitschrift für physikalische Chemie*, 119(1):277–301.

Weiner, B. B. (1971). Particle and spray sizing using laser diffraction. In *Optics in Quality Assurance II*, volume 170, pages 53–63. International Society for Optics and Photonics.

Whitaker, J. R. (1993). *Principles of enzymology for the food sciences*, volume 61. CRC Press.

Willmott, P. (2019). *An introduction to synchrotron radiation: techniques and applications*. John Wiley & Sons.

Winick, H., Brown, G., Halbach, K., and Harris, J. (1981). Wiggler and undulator magnets. *Physics Today*, 34(5):50–63.

Witkamp, G., Van der Eerden, J., and Van Rosmalen, G. (1990). Growth of gypsum: I. kinetics. *Journal of Crystal Growth*, 102(1-2):281–289.

Wittenberger, G. and Šofranko, M. (2015). Formation and protection against incrustation on the geothermal pipe by utilizing of geothermal water in the area of ďurkov (eastern slovakia). *Acta Montanistica Slovaca*, 20(1):10–15.

Wolthers, M., Charlet, L., and Van Cappellen, P. (2008). The surface chemistry of divalent metal carbonate minerals; a critical assessment of surface charge and potential data using the charge distribution multi-site ion complexation model. *American Journal of Science*, 308(8):905–941.

Wolthers, M., Nehrke, G., Gustafsson, J. P., and Van Cappellen, P. (2012). Calcite growth kinetics: Modeling the effect of solution stoichiometry. *Geochimica et Cosmochimica Acta*, 77:121–134.

Wyslouzil, B. E. and Wölk, J. (2016). Overview: Homogeneous nucleation from the vapor phase—the experimental science. *The Journal of chemical physics*, 145(21):211702.

Xu, R. (2001). *Particle characterization: light scattering methods*, volume 13. Springer Science & Business Media.

Xu, R. (2008). Progress in nanoparticles characterization: Sizing and zeta potential measurement. *Particuology*, 6(2):112–115.

Yguerabide, J. and Yguerabide, E. E. (1998). Light-scattering submicroscopic particles as highly fluorescent analogs and their use as tracer labels in clinical and biological applications: I. theory. *Analytical Biochemistry*, 262(2):137 – 156.

Yu, J., Lei, M., Cheng, B., and Zhao, X. (2004). Facile preparation of calcium carbonate particles with unusual morphologies by precipitation reaction. *Journal of crystal growth*, 261(4):566–570.

Yuan, B. and Wood, D. A. (2018). Overview of formation damage during improved and enhanced oil recovery. In *Formation Damage During Improved Oil Recovery*, pages 1–20. Elsevier.

Yuan, M., Todd, A. C., and Sorbie, K. S. (1994). Sulphate scale precipitation arising from seawater injection: a prediction study. *Marine and Petroleum Geology*, 11(1):24–30.

Zettlemoyer, A. C. (1969). Nucleation.

Zhang, F., Dai, Z., Yan, C., Bhandari, N., Yan, F., Liu, Y., Zhang, Z., Ruan, G., Kan, A. T., and Tomson, M. B. (2017). Barite-Scaling Risk and Inhibition at High Temperature. *SPE Journal*, 22(01):69–79.

Zhang, J. and Nancollas, G. (1992). Influence of calcium/sulfate molar ratio on the growth rate of calcium sulfate dihydrate at constant supersaturation. *Journal of crystal growth*, 118(3-4):287–294.

Zhang, J. and Nancollas, G. H. (1998). Kink Density and Rate of Step Movement during Growth and Dissolution of anABCrystal in a Nonstoichiometric Solution. *Journal of Colloid and Interface Science*, 200(1):131–145.

Zschörnig, O., Opitz, F., and Pittler, J. (2003). Interaction of proteins with liposomes as detected by microelectrophoresis and fluorescence. In *Liposomes, Part B*, volume 372 of *Methods in Enzymology*, pages 48 – 64. Academic Press.

Appendix A

(Appendix)

Crystal size measurements based on Figure A.1.

Table A.1: Crystal size measurements, based on SEM images, after 3 hours of incubation at $\Omega = 500$ *and* $r_{aq} = 0.01$

Width (nm)	Length (nm)	Ratio (Width/Length)
552	964	0.57
631	1060	0.60
629	1160	0.54
988	1170	0.84
Av:700 St.Dev:144	Av:1089 St.Dev:77	Av:0.64 St.Dev:0.1

Table A.2: Crystal size measurements, based on SEM images, after 3 hours of incubation at $\Omega = 500$ *and* $r_{aq} = 0.1$

Width (nm)	Length (nm)	Ratio (Width/Length)
515	562	0.92
562	674	0.83
602	688	0.88
535	581	0.92
532	561	0.94
463	546	0.85
543	584	0.93
476	727	0.65
439	607	0.72
Av:519 St.Dev:40.3	Av:614 St.Dev:55	Av:0.85 St.Dev:0.08

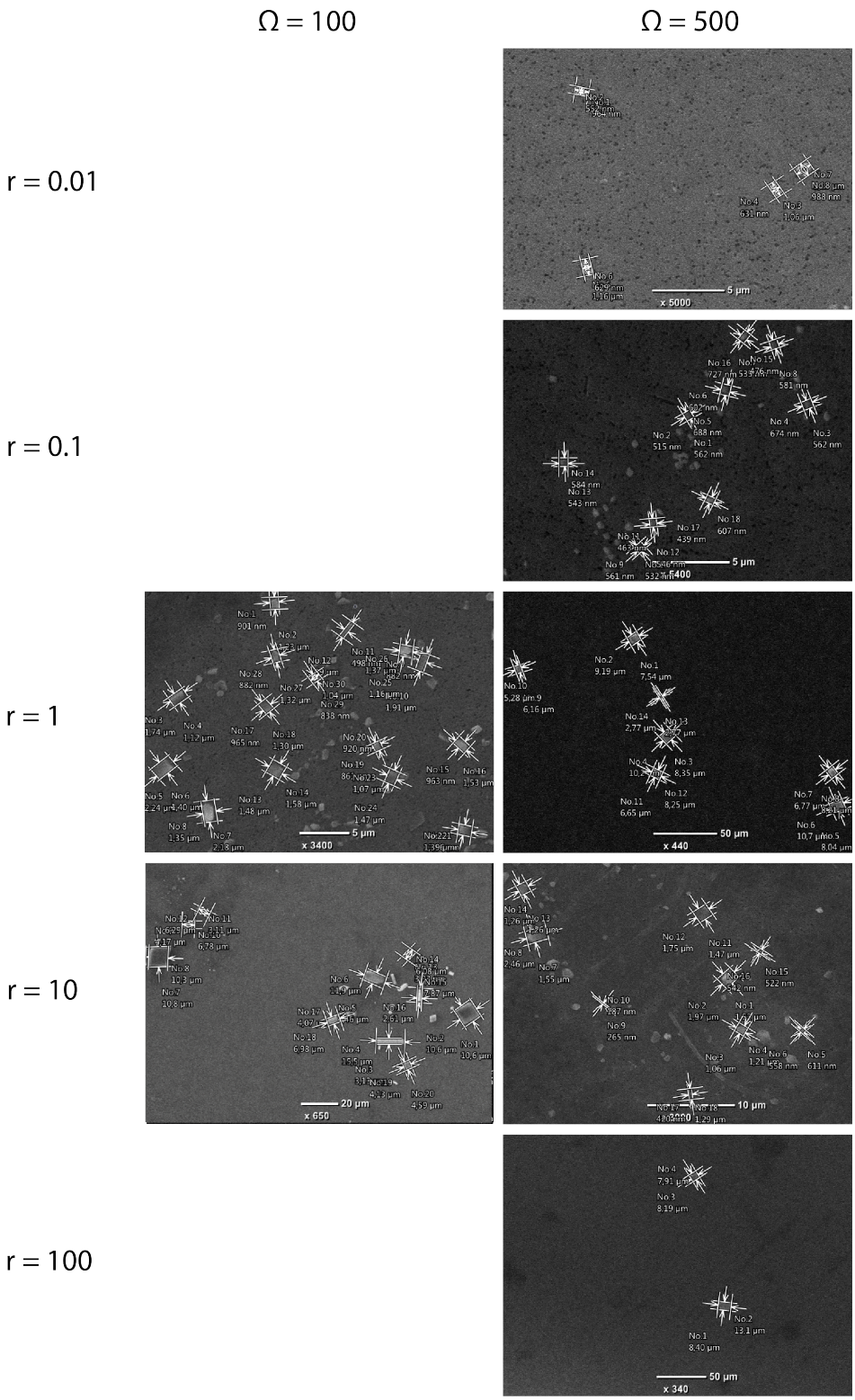

Figure A.1: Crystal size measurements, based on SEM images, $\Omega = 100$ *and* $\Omega = 500$

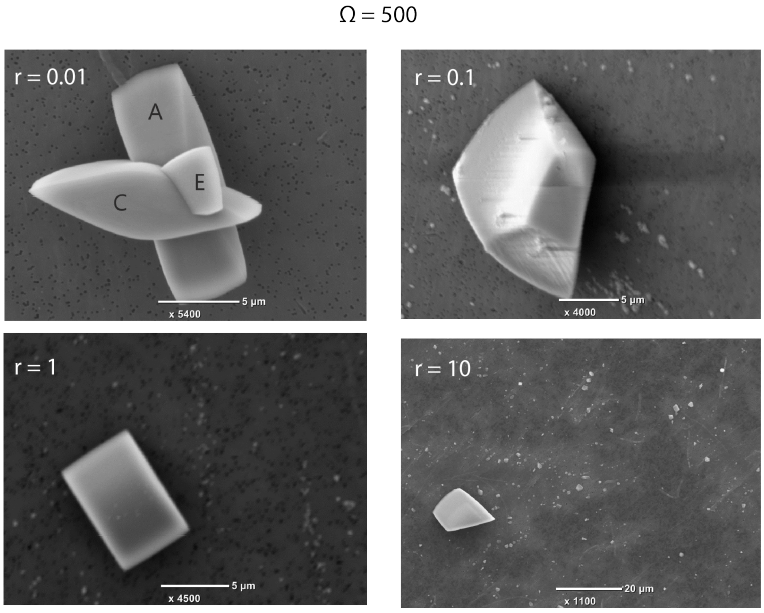

Figure A.2: Crystals observed in the SEM at $\Omega = 500$. Signs of 2D-nucleation visible on the surface of the crystal ($r_{aq} = 0.1$)

Table A.3: Crystal size measurements, based on SEM images, after 3 hours of incubation at $\Omega = 500$ and $r_{aq} = 1$

Width (nm)	Length (nm)	Ratio (Width/Length)
7540	9190	0.82
8350	10210	0.82
8040	10700	0.75
6770	8210	0.82
5280	6160	0.86
6650	8250	0.81
2770	2770	1
Av:6486 St.Dev:1406	Av:7927 St.Dev:1978	Av:0.84 St.Dev:0.05

Table A.4: Crystal size measurements, based on SEM images, after 3 hours of incubation at $\Omega = 500$ and $r_{aq} = 10$

Width (nm)	Length (nm)	Ratio (Width/Length)
1520	1970	0.77
1060	1210	0.87
558	611	0.91
1550	2460	0.63
187	265	0.71
1470	1750	0.84
1260	1260	1
522	542	0.96
420	1290	0.33
Av:950 St.Dev:470	Av:1262 St.Dev:538	Av:0.78 St.Dev:0.15

Table A.5: Crystal size measurements, based on SEM images, after 3 hours of incubation at $\Omega = 100$ *and* $r_{aq} = 1$

Width (nm)	Length (nm)	Ratio (Width/Length)
901	1230	0.73
1120	1740	0.64
1400	2240	0.63
1350	2180	0.62
882	1910	0.46
498	1390	0.36
1480	1580	0.94
963	1530	0.63
965	1300	0.74
861	920	0.94
1390	1580	0.88
1070	1470	0.73
1160	1910	0.61
882	1320	0.67
838	1040	0.81
Av:1051 St.Dev:215	Av:1556 St.Dev:300	Av:0.69 St.Dev:0.12

Table A.6: Crystal size measurements, based on SEM images, after 3 hours of incubation at $\Omega = 100$ *and* $r_{aq} = 10$

Width (nm)	Length (nm)	Ratio (Width/Length)
10600	10600	1
1550	3130	0.50
1190	5460	0.22
10300	10800	0.95
4170	6780	0.62
3110	6290	0.50
3920	6080	0.64
2610	7870	0.33
4070	6980	0.58
4130	4590	0.90
Av:4565 St.Dev:2354	Av:6858 St.Dev:1764	Av:0.67 St.Dev:0.20

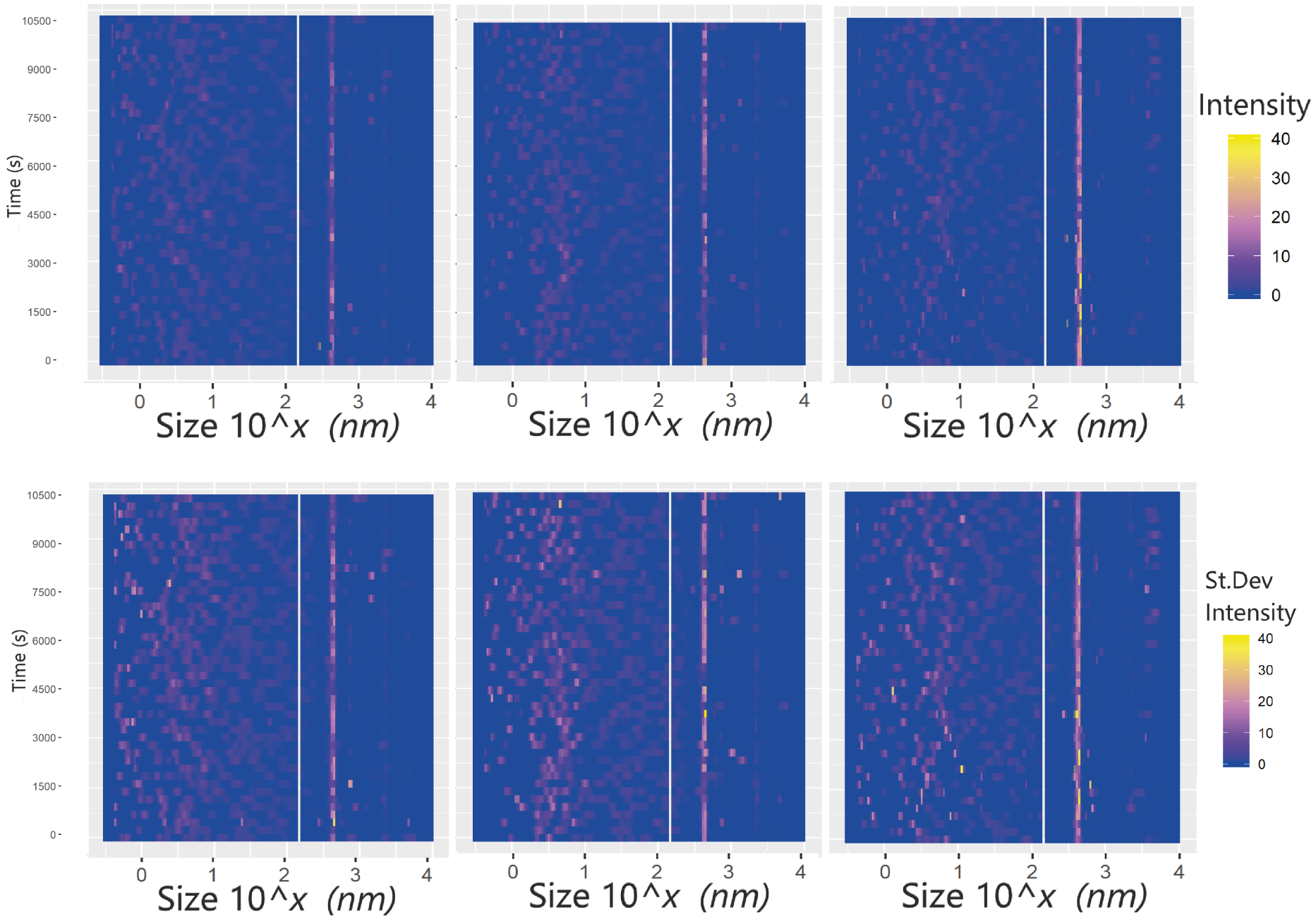

Figure A.3: Compound MADLS results of $\Omega = 500$ *(left to right -* $r_{aq} = 0.01$*,* $r_{aq} = 0.1$ *and* $r_{aq} = 1$*, with standard deviation plotted underneath*

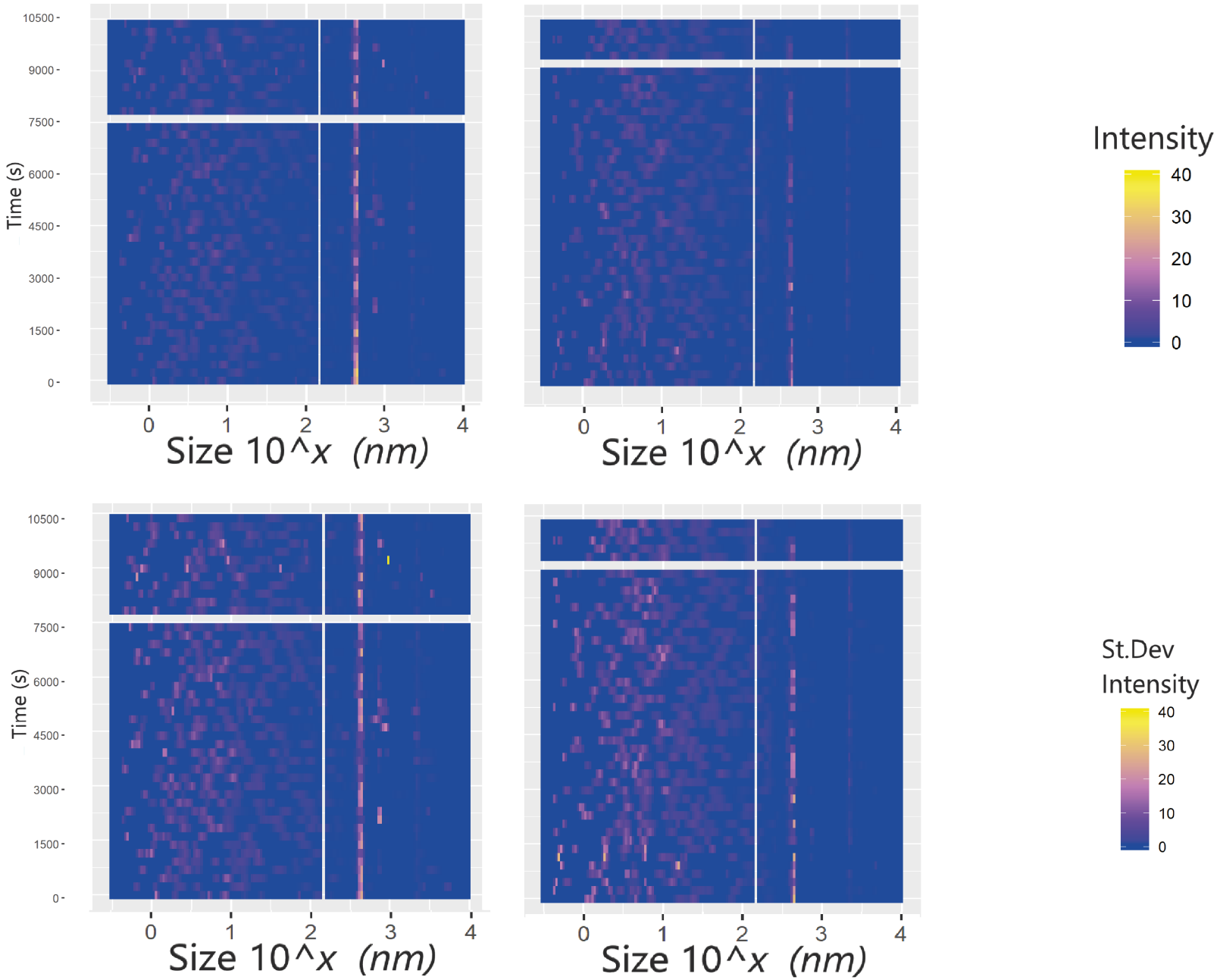

Figure A.4: Compound MADLS results of $\Omega = 500$ *(left to right -* $r_{aq} = 10$ *and* $r_{aq} = 100$*, with standard deviation plotted underneath*

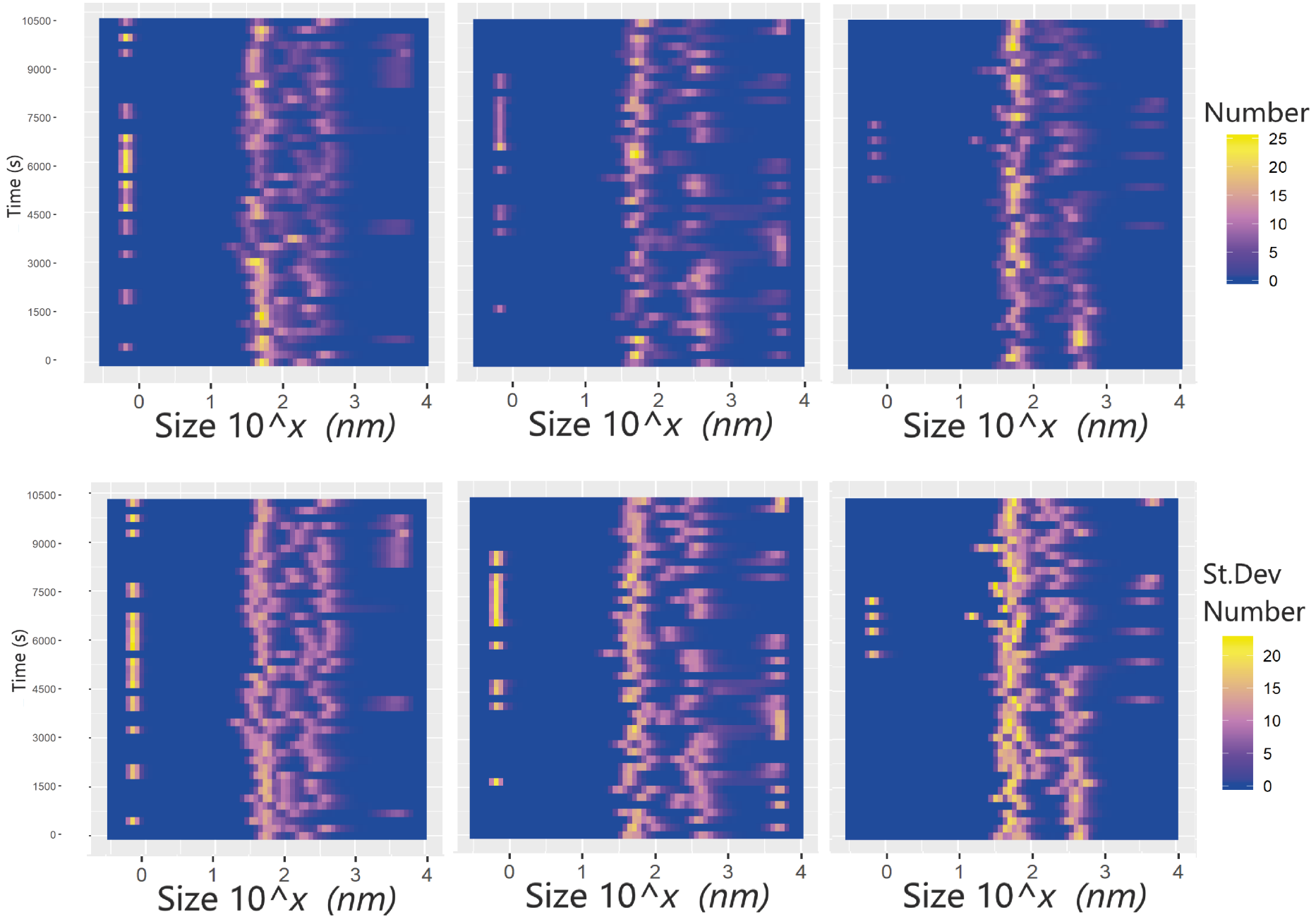

Figure A.5: Compound forward scatter results of $\Omega = 500$ *(left to right -* $r_{aq} = 0.01$, $r_{aq} = 0.1$ *and* $r_{aq} = 1$, *with standard deviation plotted underneath*

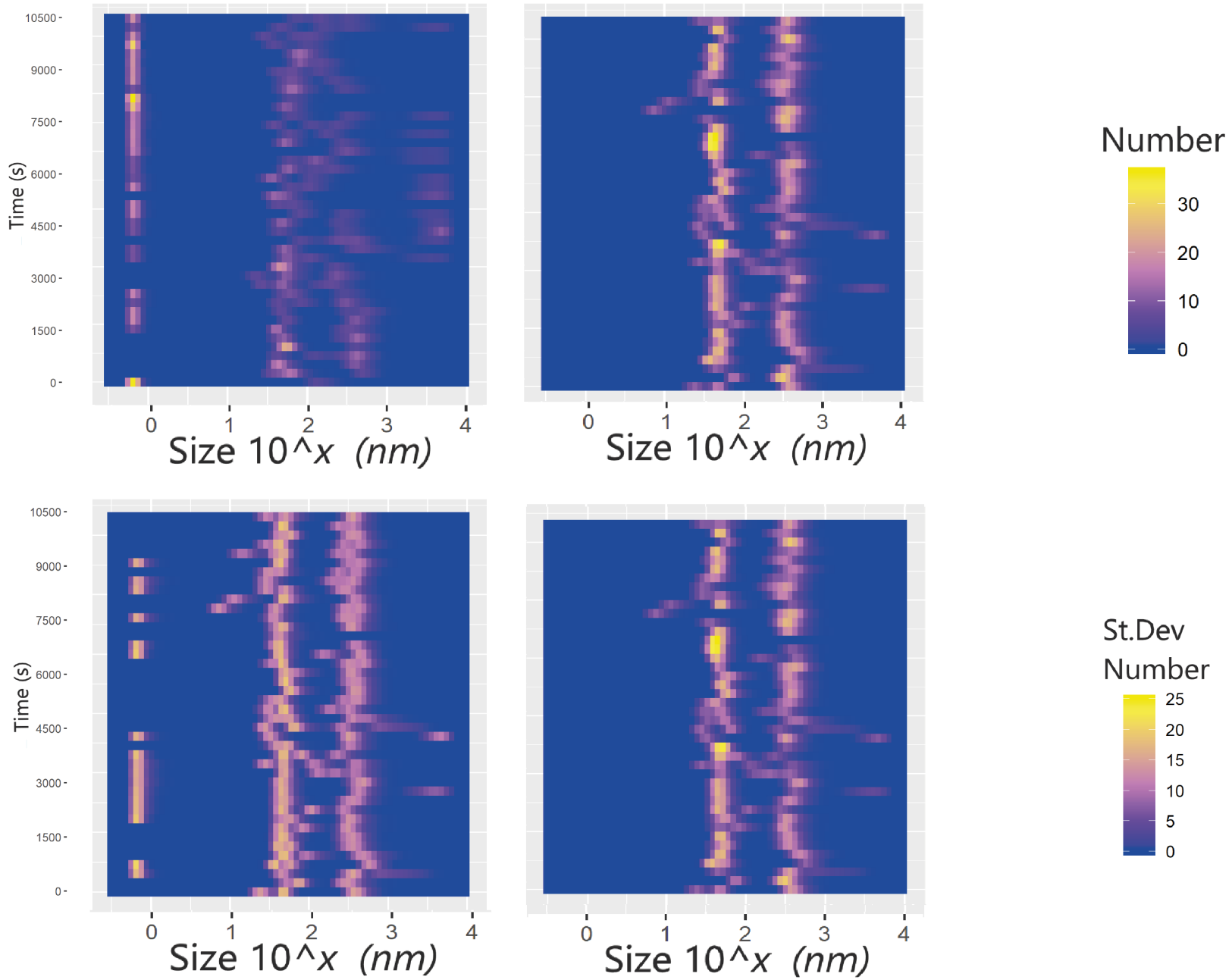

Figure A.6: Compound forward scatter results of $\Omega = 500$ *(left to right -* $r_{aq} = 10$ *and* $r_{aq} = 100$*, with standard deviation plotted underneath*

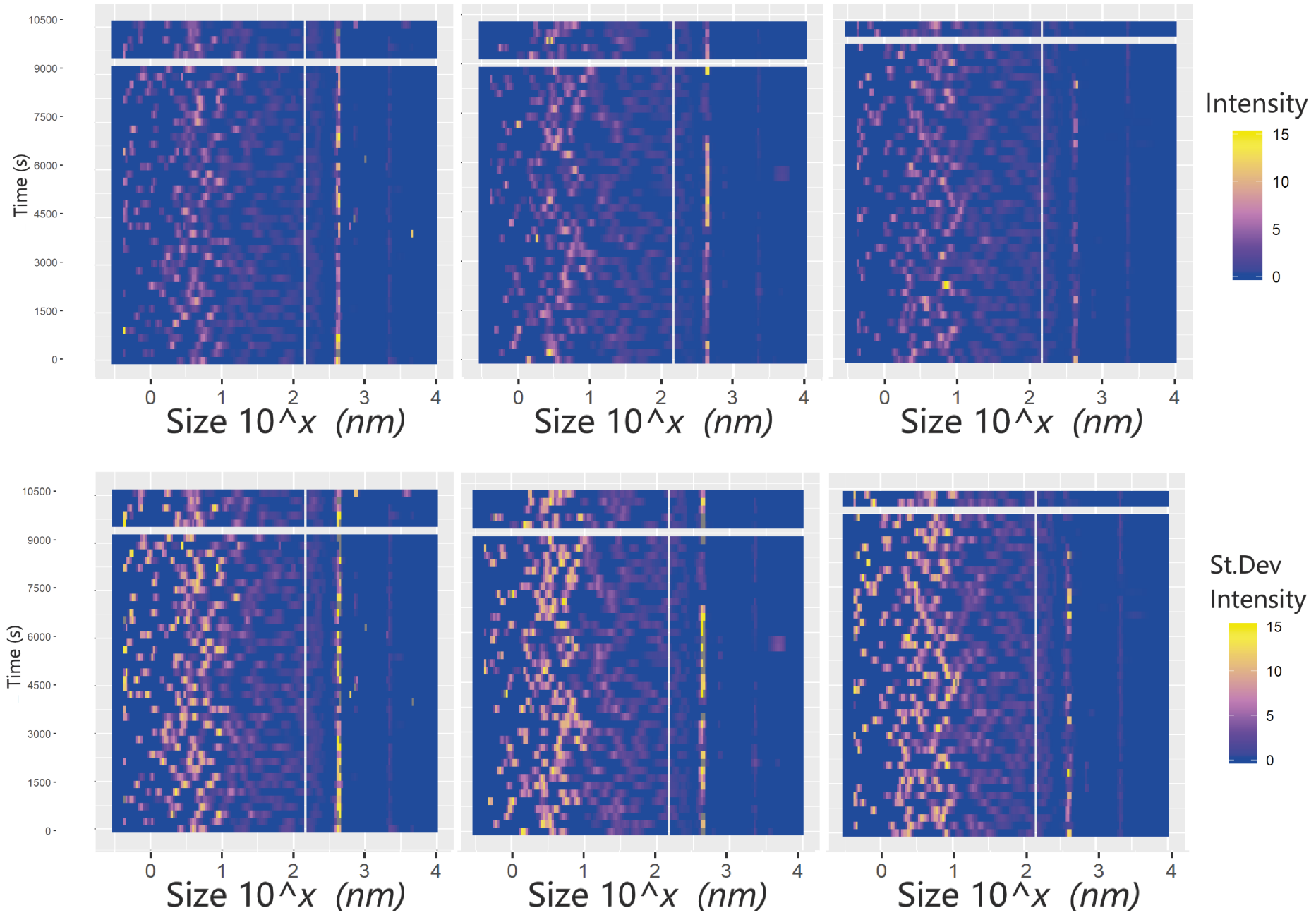

Figure A.7: Compound MADLS results of $\Omega = 100$ *(left to right -* $r_{aq} = 0.01$*,* $r_{aq} = 0.1$ *and* $r_{aq} = 1$*, with standard deviation plotted underneath*

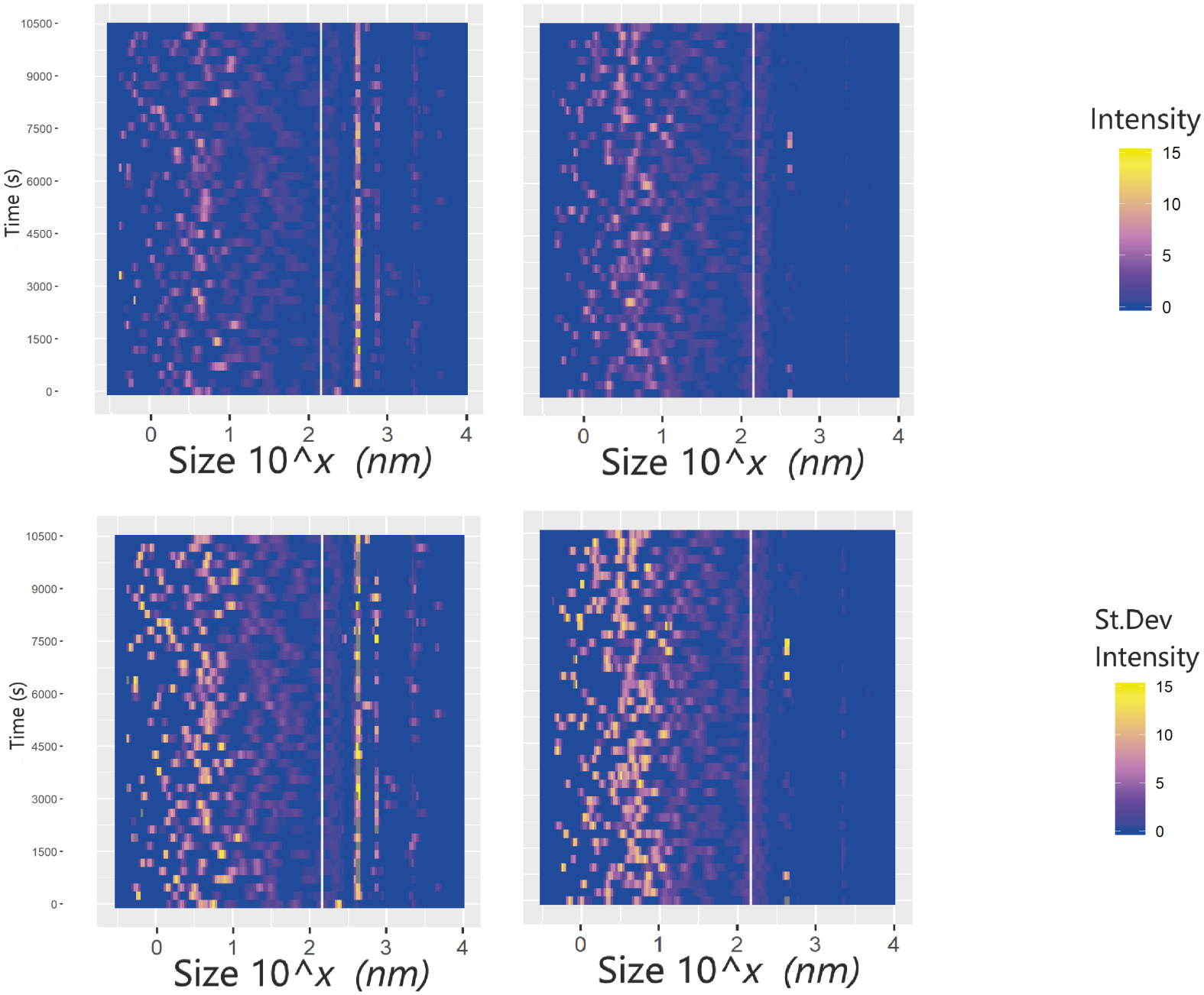

Figure A.8: Compound MADLS results of $\Omega = 100$ *(left to right -* $r_{aq} = 10$ *and* $r_{aq} = 100$*, with standard deviation plotted underneath*

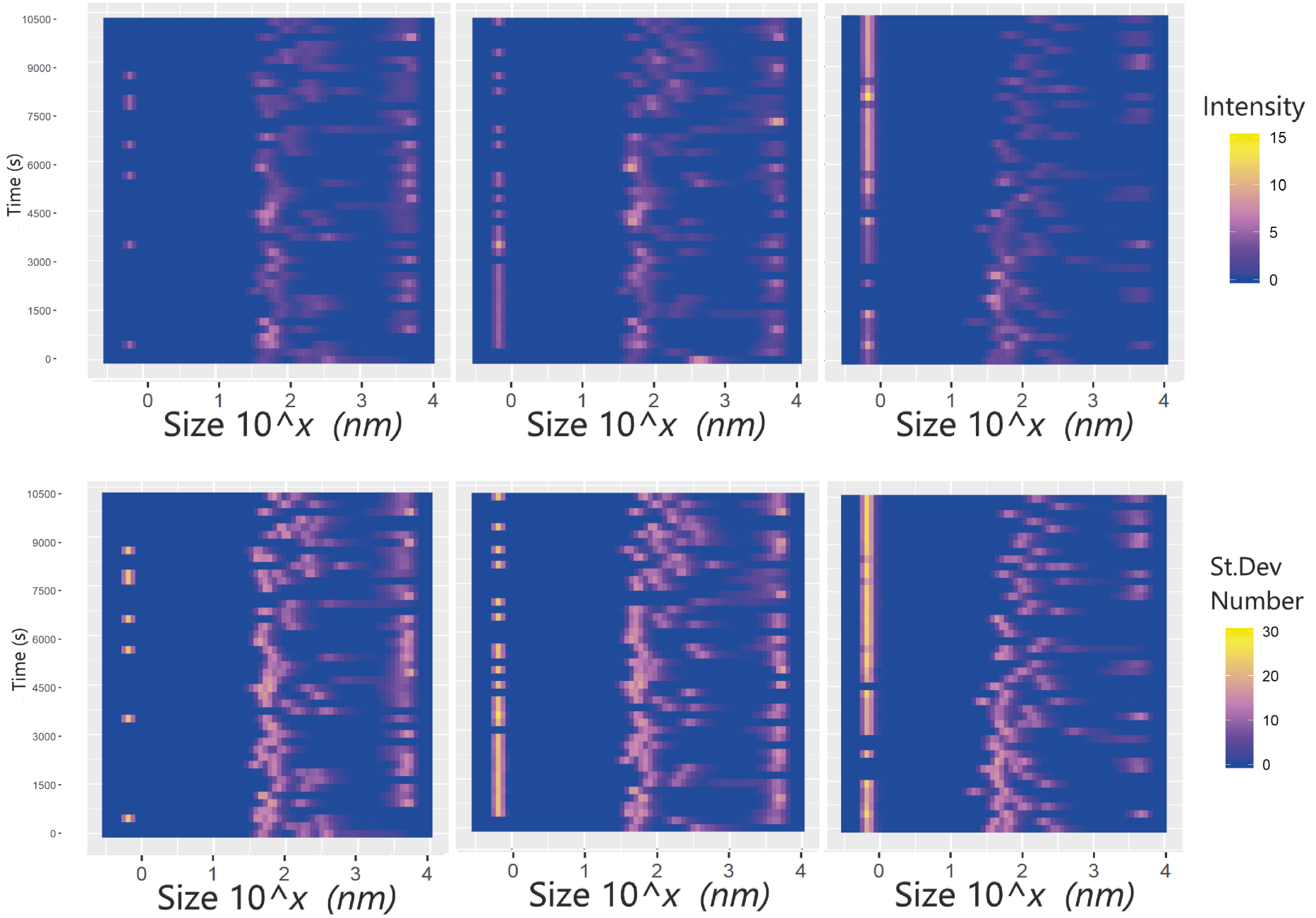

Figure A.9: Compound forward scatter results of $\Omega = 100$ *(left to right -* $r_{aq} = 0.01$, $r_{aq} = 0.1$ *and* $r_{aq} = 1$, *with standard deviation plotted underneath*

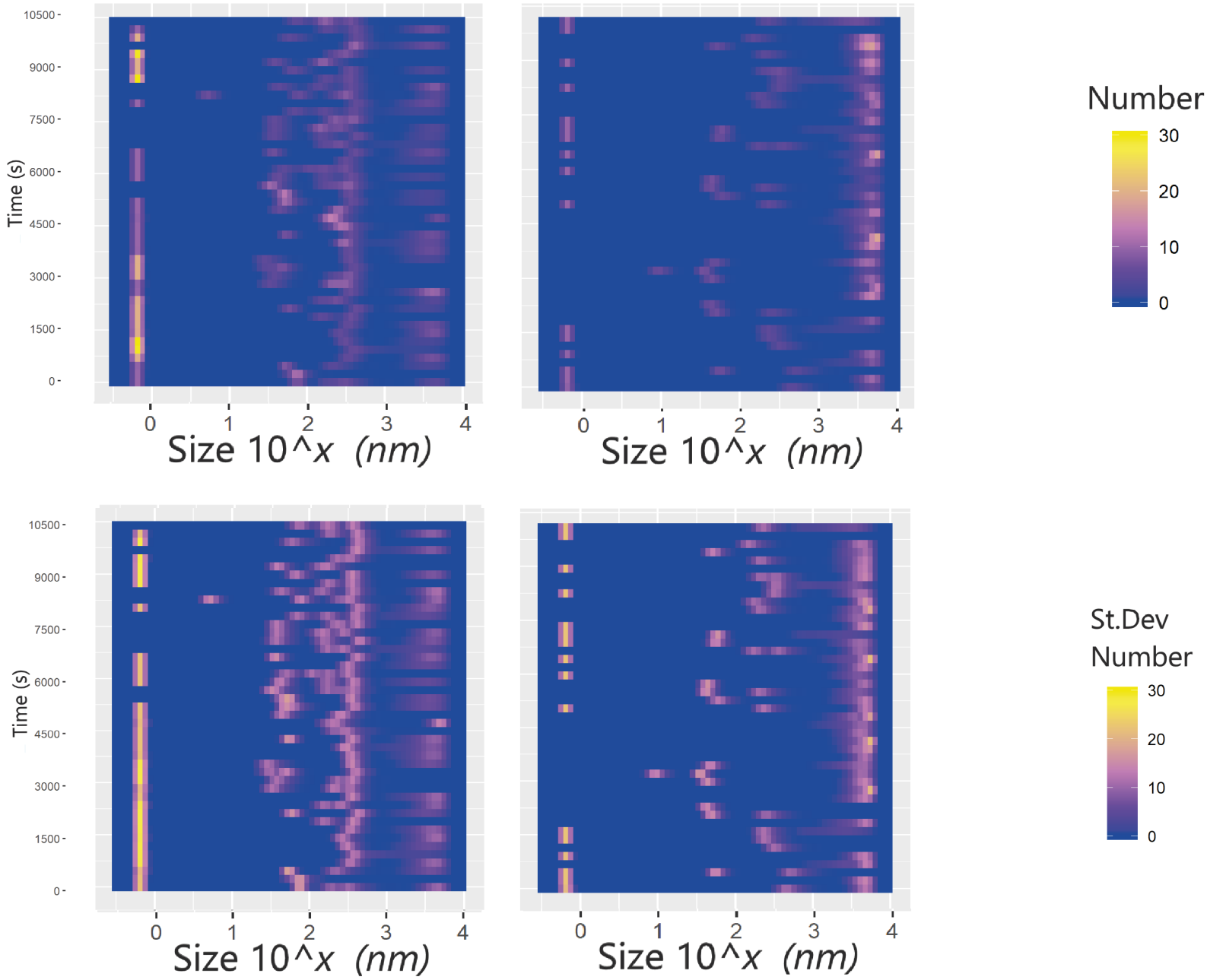

Figure A.10: Compound forward scatter results of $\Omega = 100$ *(left to right -* $r_{aq} = 10$ *and* $r_{aq} = 100$*, with standard deviation plotted underneath*

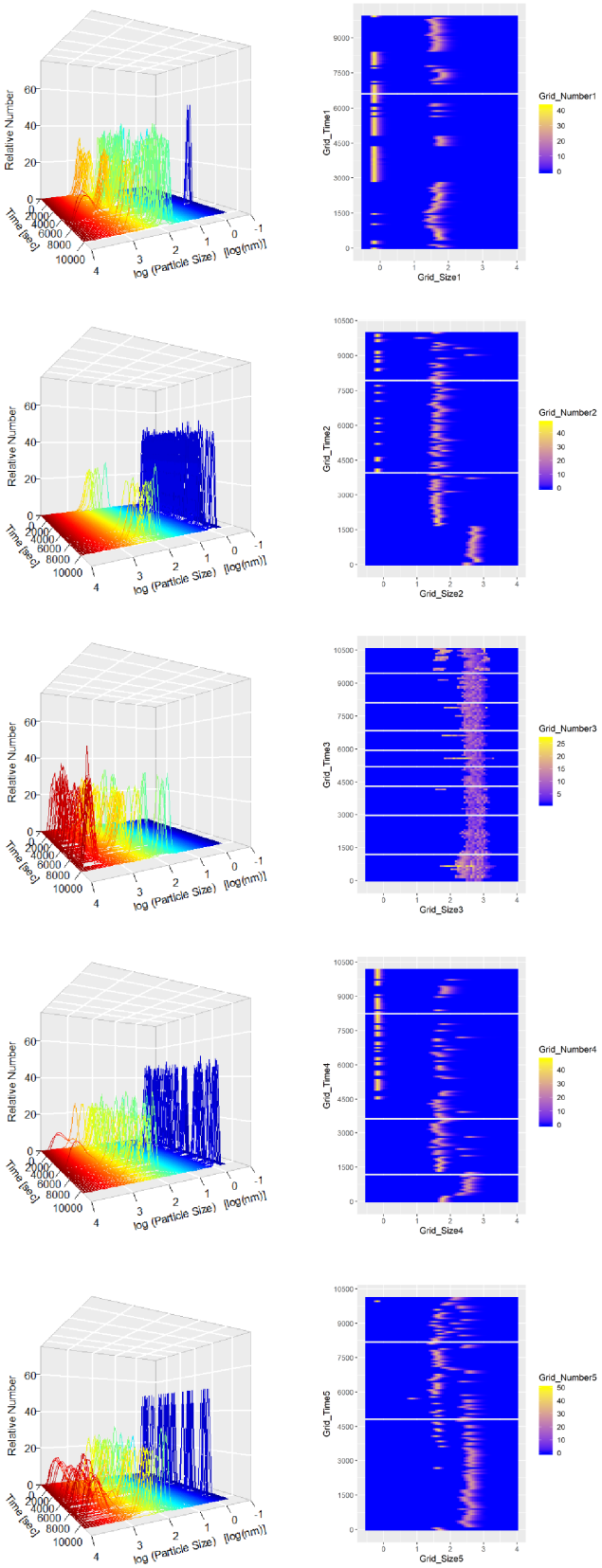

Figure A.11: Forward scatter, rapid development of $\Omega = 100$ *with* $r_{aq} = 0.01$, $r_{aq} = 0.1$, $r_{aq} = 1$, $r_{aq} = 10$ *and* $r_{aq} = 100$ *from top to bottom. Plotted side by side in 3D-plot and gridplots*

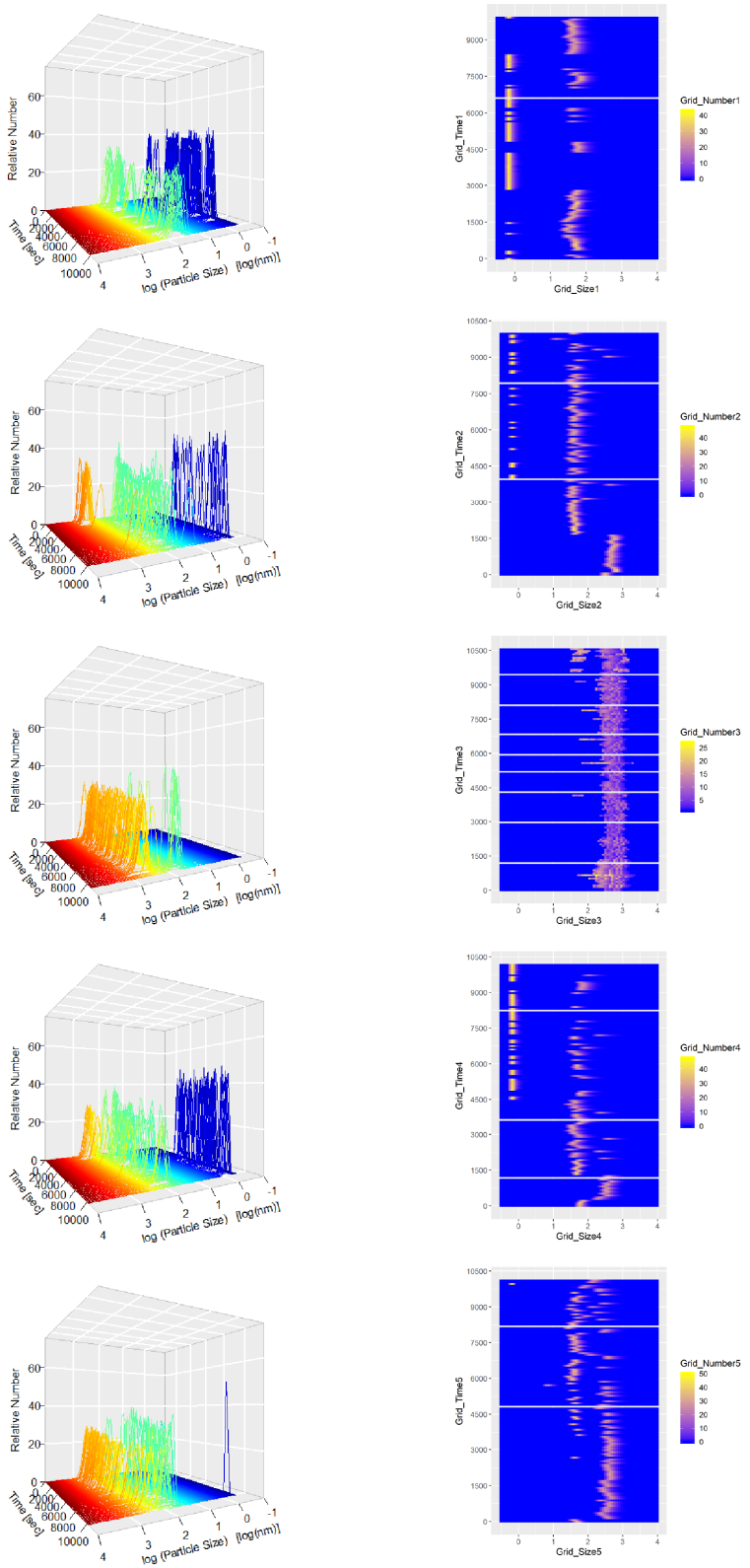

Figure A.12: Forward scatter, rapid development of $\Omega = 500$ *with* $r_{aq} = 0.01$, $r_{aq} = 0.1$, $r_{aq} = 1$, $r_{aq} = 10$ *and* $r_{aq} = 100$ *from top to bottom. Plotted side by side in 3D-plot and gridplots*

r_{aq}=0.01	Omega = 100		r_{aq}=100	Omega = 100	
Component	% of total concentration	Species name	Componer	% of total concentration	Species name
CO3-2	0.082	CO3-2	CO3-2	0.081	CO3-2
	4.655	NaHCO3 (aq)		4.474	NaHCO3 (aq)
	81.161	HCO3-		80.775	HCO3-
	13.988	H2CO3* (aq)		13.991	H2CO3* (aq)
	0.107	NaCO3-		0.567	BaHCO3+
Ba+2	73.484	Ba+2		0.103	NaCO3-
	2.572	BaSO4 (aq)	Ba+2	74.811	Ba+2
	23.928	BaNO3+		0.031	BaSO4 (aq)
	0.015	BaHCO3+		25.142	BaNO3+
Na+1	96.774	Na+1		0.015	BaHCO3+
	0.458	NaSO4-	Na+1	97.127	Na+1
	2.766	NaNO3 (aq)		2.865	NaNO3 (aq)
NO3-1	97.124	NO3-1	NO3-1	96.778	NO3-1
	2.871	NaNO3 (aq)		0.46	BaNO3+
SO4-2	74.865	SO4-2		2.762	NaNO3 (aq)
	25.104	NaSO4-	SO4-2	73.59	SO4-2
	0.031	BaSO4 (aq)		23.833	NaSO4-
				2.577	BaSO4 (aq)

Figure A.13: Example of different species distribution at extreme stochiometries

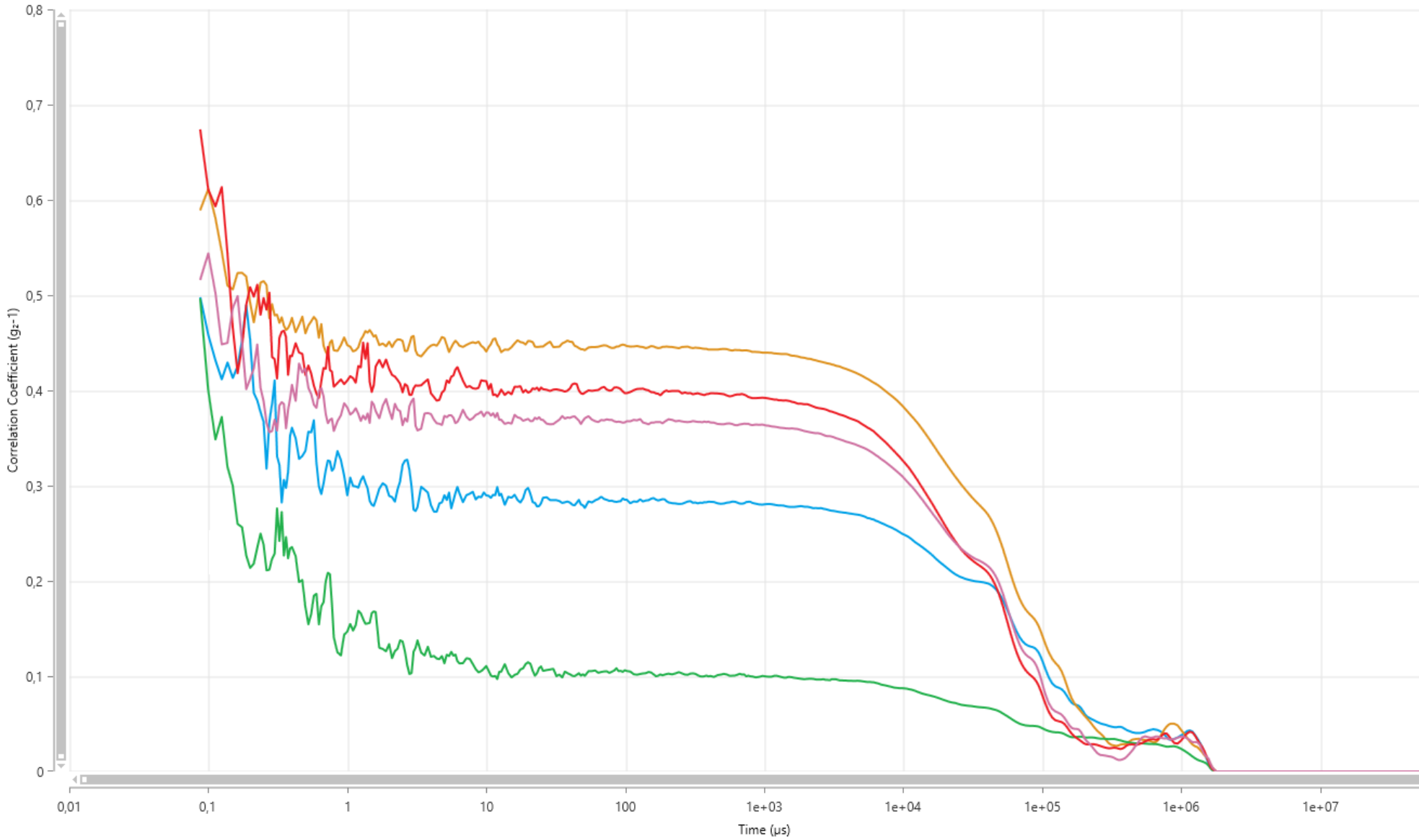

Figure A.14: Example of correlation diagram showing signs of sedimentation ($r_{aq} = 1$ and $\Omega = 500$). Timestep 20 to 24

Full Python code for automation of Minteq calculations:

```
def busc_dir():
    print ('Finding working directories')
    print ('It may take a few minutes')
    print ('Please wait')
    a=0
    flag_dir,flag_dir1,flag_dir2=False,False,False
    dbc={}
    exedir=owd+"\Mintrun17.exe"
    flag_dir2==True
    print('Working directory',owd)
    for (dirpath, dirnames, filenames) in os.walk('C:\\'):
        for f in filenames:
            if f=='comp_2008.vdb':
               dbdir=os.path.join(dirpath, f)
               db=open(dbdir,'r')
               flag_dir=True
        for f in dirnames:
            if f=='Vminteq31' and 'Program' not in dirpath:
               outdir=os.path.join(dirpath,f)
               print ('Databases directory', outdir)
               flag_dir1=True
               break
        if flag_dir==True and flag_dir1==True and flag_dir2==True:
          break
    for line in db:
        dbc[(str(line.split(',')[1]))]=str(line.split(',')[0])
    db.close()
    print ('Done')
    print ('Calculations begin. Good luck!')
    return (dbc,outdir,exedir)



def read_input(Minit,a,solutions_flag):####check if when iter the components the order is correct
    components={}
    Minit.close()
    Minit=open('initial_values_Vminteq.txt','r')
    flag=False
    lastsolution=True
    print ("Solution "+str(a))
    for line in Minit:
       if line.find("Output file")!=-1:
          outputfile=str(line.split(',')[1]).rstrip()
       if line.find("Unit")!=-1:
          unit = str(line.split(',')[1]).rstrip()
       if line.find("Ions of interest")!=-1:
          salt1=(str(line.split(',')[1]),str(line.split(',')[2]).rstrip())
       if line.find("BGE")!=-1:
          salt2=(str(line.split(',')[1]),str(line.split(',')[2]),str(line.split(',')[3]).rstrip())
       if line.find("Solution "+str(a)+'\n')!=-1:
          flag=True
          lastsolution=False
          continue
       elif line.find("Solution "+str(a+1)+'\n')!=-1:
          flag=False
          continue
       if flag==True and line.find("Boundary conditions")==-1:
          components[(str(line.split(',')[0]))]=float(line.split(',')[1])
          key = (str(line.split(',')[0]))
          if key!='"CO2 (g)"' and key !='Temp' and key!='sodiumnitrate' and unit=='Millimolal':
             components[key]=components[key]*10**(-3)
       if flag==True and line.find("Boundary conditions")!=-1:
          key=np.array(line.split())[1]
          try:
             Boundary_conditions[key]=[float(np.array(line.split())[2]),float(np.array(line.split())
                 [3])]
          except:
             Boundary_conditions[key]=str(np.array(line.split())[2])

    if lastsolution!=False:
       solutions_flag=False
    return components,Boundary_conditions,a,solutions_flag,unit,salt1,salt2,outputfile

def write_input(components,dbc,unit,outdir,exedir):
    a=0
    os.chdir(outdir)
    minin=open('minin.vda','w')
    minin.write('"Visual MINTEQ 3.1 input file  "\n')
    minin.write('"Problem no.",1\n')
    minin.write('"Databases:","thermo.vdb","type6.vdb","comp_2008.vdb","gaussian.vdb"\n')#'"Databases
        :","'+db1dir+'","'+db2dir+","+db3dir+","+db4dir+'"'+'\n')#'"\r\n')

    minin.write(str(round(components['Temp'],2))+',"'+unit+'",0.001,0\n')
    minin.write('0,0,1,0,3,0,0,0,0,1,1,0,0,0'+'\n')
    minin.write('"MULTI_/_SWEEP","",1\n')
    minin.write('0,0,0\n')
    if '"CO2 (g)"' in components:
        a+=1
    if 'Temp' in components:
        a+=1
    if 'sodiumnitrate' in components:
        a+=1
    minin.write('"No. of components",'+str(len(components)-a)+'\n')
    for key, value in components.items():
```

```
        #print('line103',key,val)
        if key!='"CO2_(g)"' and key !='Temp' and key!='sodiumnitrate':
            if components[key]<0:
                minin.write(str(dbc[key])+','+str("{:.2E}".format(components[key]))+','+'-7.00,"y","n",'+
                    str(key)+'\n')
                #minin.write('%7s%2s%8s%8s%23s%-18s\r\n'%(dbc[key],"  ",str("{:.2E}".format(components[
                    key])),'-7.00'," y                    /",str(key))) ###scientific,
            else:
                minin.write(str(dbc[key])+','+str("{:.3E}".format(components[key]))+','+str(round(math.
                    log10(components[key])))+',"y","n",'+str(key)+'\n')
                #minin.write('%7s%2s%9s%8.2f%23s%-18s\r\n'%(dbc[key],"  ",str("{:.3E}".format(components[
                    key])),float(round(math.log10(components[key]),2))," y                    /",str(key
                    ))) ###scientific,

        if key=='"CO2_(g)"':
            minin.write('""\n')
            minin.write('3,1\n')
            minin.write('3301403,18.149'+','+'-10,'+str(math.log10(components[key]))+','+str(key)+'\n')
            #minin.write('%-8s%2s%8s%11s%20s%-18s\r\n'%(str(3301403),"  ",str(round(18.149-math.log10(
                components[key]),4)),"    -10.0000","                    /",str(key))) ###scientific,
    minin.write('""\n')
    minin.write('"END"\n')
    #minin.write('  \r\n')
    #minin.write(' \r\n')
    minin.close()


def start_minteq(components,dbc,unit,outdir,exedir):
    ###create input for minteq from concentrations and species in components
    #'/mnt/c/Users/jakos/Documents/Vminteq31')
    write_input(components,dbc,unit,outdir,exedir)
    if os.system(exedir) !=0:
        print ('Oops_something_is_wrong,_please_check_input_file_in_the_Databases_directory')


## Sergio do your little dance here

def read_output(salt1,salt2,components,Boundary_conditions):#read and check decide what to do
    Minout=open('vmint.out','r')
    output={}
    eq_mass,Precipitates=False,False
    for linea in Minout:
        #if linea.find("Saturation indices and stoichiometry of all minerals")!=-1:
        #    SI=True
        if linea.find('"'+Boundary_conditions['SI_phase']+'"')!=-1:
            output['SI']=np.array(linea.split(','))[3].astype(float)
        if linea.find("Equilibrium_pH=_")!=-1:
            output['pH']=np.array(linea.split(','))[1].astype(float)
        if linea.find("Equilibrium_ionic_strength(m)=")!=-1:
            output['IS']=np.array(linea.split(','))[1].astype(float)
        if linea.find("Equilibrated_mass_distribution")!=-1:
            eq_mass=True
            continue
        if linea.find("Percent_difference=")!=-1 and eq_mass==True:
            output['Charge_Balance_%']=np.array(linea.split(','))[1].astype(float)
        if linea.find('Stoichiometry_on_line_below')!=-1:
            Precipitates=True
            a=0
            continue
        if linea.find('""')!=-1:# and Precipitates==True:
            Precipitates=False
        if Precipitates==True:
            a+=1
            if 'Precipitates' not in output and a%2!=0:
                output['Precipitates']=[(str(np.array(linea.split(','))[1]),np.array(linea.split(','))
                    [3].astype(float))]
            elif a%2!=0:
                output['Precipitates'].append((str(np.array(linea.split(','))[1]),np.array(linea.split(
                    ','))[3].astype(float)))

        if eq_mass==True and linea.find(salt1[0])!=-1:
            saltconc0=(np.array(linea.split(','))[2].astype(float))
        if eq_mass==True and linea.find(salt1[1])!=-1:
            saltconc1=(np.array(linea.split(','))[2].astype(float))
        for key, val in components.items():
            if eq_mass==True and linea.find(key)!=-1:# and linea.find("Equilibrated mass distribution
                ")==-1:
                output[key]=np.array(linea.split(','))[2].astype(float)


    output['r']=saltconc0/saltconc1

    Minout.close()
    return output


def check_parameters(output,Boundary_conditions,components,salt1,salt2):
    components

    check=False


    if not (output['IS']>(Boundary_conditions['IS'][0]-Boundary_conditions['IS'][1]) and output['IS']<
        (Boundary_conditions['IS'][0]+Boundary_conditions['IS'][1])):
        check=True
        if output['IS']<=(Boundary_conditions['IS'][0]-Boundary_conditions['IS'][1]):
```

```
            components[salt2[0]]=components[salt2[0]]*1.05###increment to go to the next loop
            components[salt2[1]]=components[salt2[1]]*1.05

        if output['IS']>= (Boundary_conditions['IS'][0]+Boundary_conditions['IS'][1]):
            check=True
            components[salt2[0]]=components[salt2[0]]*0.95###increment to go to the next loop
            components[salt2[1]]=components[salt2[1]]*0.95

    if not (output['pH']>(Boundary_conditions['pH'][0]-Boundary_conditions['pH'][1]) and output['pH']<
        (Boundary_conditions['pH'][0]+Boundary_conditions['pH'][1])):
        check=True

        if output['pH']<=(Boundary_conditions['pH'][0]-Boundary_conditions['pH'][1]):
            if components['"H+1"']<0:
                d=((14+math.log10(-components['"H+1"']))+0.01)#*1.001)###pH
                if d<=7:
                    components['"H+1"']=10**(-d)-10**(-7)
                else:
                    components['"H+1"']=-(10**(-(14-d))-10**(-7))##OH- concentration
            else:##acid
                d=(-math.log10(components['"H+1"']))+0.01###pH
                if d<=7:
                    components['"H+1"']=10**(-d)-10**(-7)
                else:
                    components['"H+1"']=-(10**(-(14-d))-10**(-7))
        if output['pH']>= (Boundary_conditions['pH'][0]+Boundary_conditions['pH'][1]):
            check=True

            if components['"H+1"']<0:
                d=((14+math.log10(-components['"H+1"']))-0.01)#*0.999)###pH
                if d<=7:
                    components['"H+1"']=10**(-d)-10**(-7)
                else:
                    components['"H+1"']=-(10**(-(14-d))-10**(-7))##OH- concentration
            else:##acid
                d=(-math.log10(components['"H+1"']))-0.01#*0.999###pH
                if d<=7:
                    components['"H+1"']=10**(-d)-10**(-7)
                else:
                    components['"H+1"']=-(10**(-(14-d))-10**(-7))##OH- concentration

    if not (output['SI']>(Boundary_conditions['SI'][0]-Boundary_conditions['SI'][1]) and output['SI']<
        (Boundary_conditions['SI'][0]+Boundary_conditions['SI'][1])):
        check=True
        if output['SI']<=(Boundary_conditions['SI'][0]-Boundary_conditions['SI'][1]):
            components[salt1[0]]=components[salt1[0]]*1.01###increment to go to the next loop
            components[salt1[1]]=components[salt1[1]]*1.05
        if output['SI']>= (Boundary_conditions['SI'][0]+Boundary_conditions['SI'][1]):
            check=True
            components[salt1[0]]=components[salt1[0]]*0.95###increment to go to the next loop
            components[salt1[1]]=components[salt1[1]]*0.95
    if not (output['r']>(Boundary_conditions['r'][0]-Boundary_conditions['r'][1]) and output['r']<(
      Boundary_conditions['r'][0]+Boundary_conditions['r'][1])):
        print('r',output['r'])
        check=True
        if output['r']<=(Boundary_conditions['r'][0]-Boundary_conditions['r'][1]):
            components[salt1[0]]=components[salt1[0]]*1.05
            #components[salt1[1]]=components[salt1[1]]*1.05
        if output['r']>= (Boundary_conditions['r'][0]+Boundary_conditions['r'][1]):
            check=True
            components[salt1[0]]=components[salt1[0]]*0.95
            #components[salt1[1]]=components[salt1[1]]*0.95

    return check, components

def excel_cal(components,output,salt2,check):#write inputs in file or RAM
    ##np the exact calulations of the excel sheet
    #sodium -2*SO4-2 - OH
    #if output['pH']>=7:
    check2=False
    if check == False:

        pOH=14-output['pH']
        OH=10**(-pOH)
        if components['"H+1"']<=0:#Na-NaSO4-NaOH-->NaNO3+Ba(NO3)2
            sodiumnitrate=components[salt2[0]] - 2*components[salt1[1]]+components['"H+1"']
            components['sodiumnitrate']=sodiumnitrate

            if sodiumnitrate==(components[salt2[1]]-2*components[salt1[0]]):
                check2=True

                print ('Final_result')###final check
            components[salt2[1]]=2*components[salt1[0]]+sodiumnitrate

        if components['"H+1"']>0 and salt2[2]==salt2[1] :#Cl-CaCl2-HCl--->NaCl+CaCl2
            sodiumnitrate=components[salt2[1]] - 2*components[salt1[0]]-components['"H+1"']
            components['sodiumnitrate']=sodiumnitrate
            if sodiumnitrate==(components[salt2[0]]-2*components[salt1[1]]):
                check2=True

                print ('Final_result')###final check

            components[salt2[0]]=2*components[salt1[1]]+sodiumnitrate

        if components['"H+1"']>0 and salt2[2]!=salt2[1] and salt2[2] in components:
            if components[salt2[2]]==components['"H+1"']:
```

```
                check2=True

                print ('Final_result')
            components[salt2[2]]=components['"H+1"']

        if components['"H+1"']>0 and salt2[2]!=salt2[1] and salt2[2] not in components:
            sodiumnitrate=components[salt2[1]] - 2*components[salt1[0]]-components['"H+1"']
            components['sodiumnitrate']=sodiumnitrate
            if sodiumnitrate==(components[salt2[0]]-2*components[salt1[1]]):
                check2=True
            components[salt2[0]]=2*components[salt1[1]]+sodiumnitrate


        #components[salt2[0]]=2*components[salt1[1]]+OH+sodiumnitrate

        ##Na=NaNO3+NaOH+Na2SO4
        ##NO3=NaNO3+BaNO3

    check=True
    return check2, components


def write_final(components,output,a,Boundary_conditions,outputfile):
    ## write everythin in output
    #a=4
    os.chdir(owd)#'#/mnt/c/Users/jakos/OneDrive/Janou-PhD/automation/')
    fout=open(outputfile,'a')
    fout.write('Solution  '+str(a)+'\n')
    fout.write(salt1[0]+'('+salt2[1]+')2    '+str("{:.3E}".format(components[salt1[0]]))+'\n')
    fout.write('('+salt2[0]+')2'+salt1[1]+'    '+str("{:.3E}".format(components[salt1[1]]))+'\n')

    if components['"H+1"']<=0:
        fout.write(salt2[0]+'OH    '+str("{:.3E}".format(-1*components['"H+1"']))+'\n')
        fout.write(salt2[0]+salt2[1]+'    '+str("{:.3E}".format(components['sodiumnitrate']))+'\n')
    if components['"H+1"']>0 and salt2[2]!=salt2[1] and salt2[2] in components:
        fout.write(salt2[0]+salt2[1]+'    '+str("{:.3E}".format((components[salt2[1]]-components[salt1
            [0]])))+'\n')
        fout.write('H'+salt2[2]+'    '+str("{:.3E}".format(components['"H+1"']))+'\n')

    if components['"H+1"']>0 and salt2[2]!=salt2[1] and salt2[2] not in components:
        fout.write(salt2[0]+salt2[1]+'    '+str("{:.3E}".format(components['sodiumnitrate']))+'\n')
        fout.write('H'+salt2[1]+'    '+str("{:.3E}".format(components['"H+1"']))+'\n')
    if components['"H+1"']>0 and salt2[2]==salt2[1]:
        fout.write(salt2[0]+salt2[1]+'    '+str("{:.3E}".format(components['sodiumnitrate']))+'\n')
        fout.write('H'+salt2[1]+'    '+str("{:.3E}".format(components['"H+1"']))+'\n')
    fout.write('pH  '+str(output['pH'])+'  SI  '+str(Boundary_conditions['SI_phase'])+'  '+str(output[
        'SI'])+'  Omega  '+str(10**output['SI'])+'  IS  '+str(output['IS'])+'  r  '+str(output['r'])+
        '\n')
    fout.write('Charge balance %  '+str(output['Charge Balance %'])+'\n')
    fout.write('Precpitates\n')
    for i in range(0,(len(output['Precipitates']))):
      fout.write(output['Precipitates'][i][0]+'  '+str(output['Precipitates'][i][1])+'\n')

    fout.write('\n')
    fout.close
    #print(salt1[0]+'('+salt2[1]+')2',components[salt1[0]])
    #print('('+salt2[0]+')2'+salt1[1],components[salt1[1]])
    #print(salt2[0]+'OH',(-1*components['"H+1"']))
    print('pH',output['pH'],'SI ',Boundary_conditions['SI_phase'],output['SI'],'Omega',(10**output['
        SI']),'IS',output['IS'],'r',output['r'])
    #print(Boundary_conditions)

def driver(components,Boundary_conditions,unit,salt1,salt2,dbc,outdir,exedir):
  check,check2=True, False
  while check2 == False:
        while check == True:
              start_minteq(components,dbc,unit,outdir,exedir)
              output=read_output(salt1,salt2,components,Boundary_conditions)
              check, components=check_parameters(output,Boundary_conditions,components,salt1,salt2)
              #print(components)
        check2,components=excel_cal(components,output,salt2,check)
        check=True


  return components,output

def run_all():
    a=1
    dbc,outdir,exedir=busc_dir()
    solutions_flag=True
    while solutions_flag==True:
        components,Boundary_conditions,a,solutions_flag,unit,salt1,salt2,outputfile=read_input(Minit,a
            ,solutions_flag)
        if solutions_flag==False:
            break
        components,output=driver(components,Boundary_conditions,unit,salt1,salt2,dbc,outdir,exedir)
        write_final(components,output,a,Boundary_conditions,outputfile)
        time.sleep(1)
        a+=1


### Main block
import numpy  as np
import math
import time
import os
```

```
start_time = time.time()
Minit=open('initial_values_Vminteq.txt','r')
salt1=('"Ba+2"','"SO4-2"')#('Ca+2','CO3-2')
salt2=('"Na+1"','"NO3-1"','"Cl-1"')#('Na+1','Cl-1')
Boundary_conditions={}
Boundary_conditions['IS']=[0.200,0.05]
Boundary_conditions['pH']=[7.0,0.05]
Boundary_conditions['SI']=[1.8,0.1]
Boundary_conditions['r']=[1.0,0.0001]
owd = os.getcwd()
###Minteq loop
##puting in the initial values
##reading and checking the output, produce new input based on the output or if everything is fine do
    the excel calculation
###reput the revised values in minteq
##Calculate NaNO3 salt, revise the input with new salt concentrations
##reput the revised values in minteq
##reading and checking the output, if something is off start minteq again according to which value is
    off.

run_all()
exe_time=round(((time.time() - start_time)/60),2)
print ('***************')
print ('Execution_time')
print(exe_time,'_minutes' )
print ('All_done._Enjoy')
print('*****************')
```

Full Python code for the fitting of the SAXS-data

```
# -*- coding: utf-8 -*-
"""
"""

# Import libraries
import matplotlib.pyplot as plt
import numpy as np
import math
import os
from scipy.optimize import leastsq
import pandas as pd
from os.path import isfile
import scipy.integrate as spi
from decimal import Decimal


#============================================================
# Parameters
#============================================================

path = 'C:/Users/David/Documents/Uni/Master/MSC_thesis/SAXS_data/Figures/'
os.chdir('C:/Users/David/Documents/Uni/Master/MSC_thesis/SAXS_data/data_treated')

# Define the range of R
R = np.arange(0.01, 250, 0.25)

# Define parameters in case of manual fitting
N = 400
mu = 100
s = 0.2
eta = 2e-9
p = [N,mu,s,eta]

#=======================================================
# Define fitting function: form factor for spheres
# with a lognormal distribution for their radii R
#=======================================================

# Lognorm(mu, s)
# Function to obtain lognormal distribution as a function of R, with a normalized area equal to 1
def Lognorm(coeffs):
    # coeffs[1] = mu, coeffs[2] = s
    Lognorm = R**(-1) * np.exp(- (np.log(R)-np.log(coeffs[1]))**2 / (2*coeffs[2]**2))
    # Obtain area with trapezoid method
    Lognorm_int = spi.trapz(Lognorm, R)
    # Divide Lognormal function by area to obtain a new area equal to 1
    Lognorm_norm = Lognorm/Lognorm_int
    # Check if area is equal to 1
    #Lognorm_int_norm =spi.trapz(Lognorm_norm, radii)
    #print(Lognorm_int_norm)
    #plt.plot(radii,Lognorm_norm)
    return(Lognorm_norm)

# Iq_calc(q, N, mu, s, eta)
# Function to obtain I(q) for plotting
def Iq_calc(q, coeffs):

    # coeffs[0] = N, coeffs[3] = eta
    # define radius R as a lognormal distribution
    Lognorm_N = coeffs[0] * Lognorm(coeffs)

    #define a matrix Iq
    Iq=[]
    # obtain I(R) at every q
    for qval in q:
```

```
        Iint=0
        rindex=0
        # sum over R values to simulate the integration over R and finally obtain I(q)
        for r in R:
            Iint=Iint+Lognorm_N[rindex]*(4/3*math.pi*r**3)**2 *coeffs[3]**2 *(((3*(math.sin(qval*r)-
                qval*r*math.cos(qval*r))/(qval*r)**3))**2)
            rindex=rindex+1
        Iq.append(Iint)
    return(Iq)

#=================================================
# Plot invariant
#=================================================

# function to plot invariant from files
# dataname, e.g. 'inv_titration_r10_KCl_v0p3_run1'
def invariant2(dataname):
    os.chdir('C:/Users/David/Documents/Uni/Master/MSC_thesis/SAXS_data/databarite')
    file=(dataname+'.csv')
    a=np.loadtxt(file).T
    plt.plot(a[0],a[1])
    plt.xlabel('time [min.]')
    plt.ylabel('Q')
    plt.savefig(os.path.join(path, dataname+'_invariant.png'), dpi=800)



#=================================================
# Function to obtain overview plot of one run,
# dataname as follows: 'data_titration_r0p1_KCl_v0p6'
#=================================================
# Label range: -7 for threenumbered timeframes; -6 for twonumbered timeframes
def multiplot(dataname, t_induction):
    os.chdir('C:/Users/David/Documents/Uni/Master/MSC_thesis/SAXS_data/data_treated')
    datapathname='./'+dataname+'/'+dataname+'_'
    range_filenames=np.arange(t_induction-10,t_induction+15,5)
    # Generate a list of expected file names
    expected_files = [datapathname+"{}.csv".format(i) for i in range_filenames]
    # Filter the list to just the files that actually exist
    actual_files = [f for f in expected_files if isfile(f)]
    # Load files and plot data in one figure
    #plt.figure(figsize=(8,10))
    for file in actual_files:
        if file[-7] == '_':
            nr = -6
        else:
            nr = -7
        a=np.loadtxt(file, skiprows=4).T
        plt.loglog(a[0][1:200],a[1][1:200], label='frame:'+str(file)[nr:-4])
        plt.legend(loc=1 ,prop={'size': 8})
        plt.xlim(min(a[0]), a[0][200])
        #plt.xlim(0,10)
        plt.ylim(1e-8, 1)
        plt.xlabel('q ($nm^{-1}$)')
        plt.ylabel('I(q)')
    plt.savefig(os.path.join(path+dataname, dataname+'multiplot2.png'), dpi=800)


#=================================================
# Open files, obtain means
#=================================================
# Function to open file and create dataframe
# Example for filename: 'data_titration_r0p1_KCl_v0p6_run2_60.csv'
def data(filename):
    if filename[-7] == '_':
        nr = -7
    else:
        nr = -8
    os.chdir('C:/Users/David/Documents/Uni/Master/MSC_thesis/SAXS_data/data_treated/'+filename[:nr])
    a=np.loadtxt(filename, skiprows=18).T   #from file Alex, skiprows=18
    X=a[0]
    Y=a[1]
    data=pd.DataFrame({'q_exp': X[1:55], 'I_exp': Y[1:55]})
    return(data)


# Functions to obtain means of datasets
def mean2(data1, data2):
    data = pd.DataFrame({'x1':data1['I_exp'],'x2':data2['I_exp']})
    mean = data.mean(axis=1)
    return(mean)

def mean3(data1, data2, data3):
    data = pd.DataFrame({'x1':data1['I_exp'],'x2':data2['I_exp'],
                         'x3':data3['I_exp']})
    mean = data.mean(axis=1)
    return(mean)



#=======================================
# Function plot data and fitting function
# with manually defined parameters
#=======================================
def manual_fit(data):
```

```
    q = data['q_exp']
    plt.loglog(q,Iq_calc(q,p), label='form_function_sphere_fit')
    plt.loglog(data['q_exp'],data['I_exp'], label='experimental_data')

    plt.title('SAXS_data_fit:_r=0.1,_v=0.6_mL_$min^{-1}$,_run_2,_timeframe_61')
    plt.xlabel('q_($nm^{-1}$)')
    plt.ylabel('I_(q)')
    plt.legend(loc=1 ,prop={'size': 8})



#=========================================
# Fitting function: nonlinear least squares
#=========================================

#define function to calculate residuals
def residuals(param, y, x):
    err = y-Iq_calc2(x,param)
    abserr = abs(err)
    return abserr

#define function to calculate leastsquares fit
def fit(data):
    dataname = 'data_titration_r1_KCl_run1'
    q = data['q_exp']
    q_4 = 0.00000001*q**-4
    #initial guesses for the fitting parameters
    N_ini=10
    mu_ini=100
    s_ini=0.2
    eta_ini=7e-8
    mu2_ini=60
    p0 = [N_ini,mu_ini,s_ini,eta_ini,mu2_ini]
    #the leastsq package calls the Levenberg-Marquandt algorithm
    plsq = leastsq(residuals, p0, args=(data['I_exp'], data['q_exp']),
                   maxfev=2000)
    #obtain plot
    plt.loglog(q,Iq_calc(q,plsq[0]), label='Nls_fit')
    plt.loglog(q, data['I_exp'],'.', label='Experimental_data')
    plt.loglog(q,q_4, label= '$q^{-4}$')
    plt.title('frame_108')
    plt.xlabel('q_($nm^{-1}$)')
    plt.ylabel('I_(q)')
    plt.text(0.07,0.00001, 'N_=_'+str(round(plsq[0][0],2)), fontsize=8)
    plt.text(0.07,0.000006, '\u03BC_=_'+str(round(plsq[0][1],0)), fontsize=8)
    plt.text(0.07,0.0000035, 's_=_'+str(round(plsq[0][2],2)), fontsize=8)
    plt.text(0.07,0.000002, '\u03B7_=_'+str("{:0.2e}".format(plsq[0][3])), fontsize=8)
    plt.text(0.07,0.000001, '\u03BC'+'$_{2}_=$'+str(round(plsq[0][4],0)), fontsize=8)
    plt.legend(loc=1 ,prop={'size': 8})
    plt.savefig(os.path.join(path, dataname+'bimodal_108_fit.png'), dpi=800)
    print(plsq[0])


#install.packages("plot3D")
library("plot3D")
library("rgl")
library(emdbook)                    # Logaritmic applications
library(bbmle)                      # Logaritmic applications
library(numDeriv)                   # Logaritmic applications
library(plot3D)
library(vrmlgen)
library(tidyr)
library(ggplot2)
library(scales)
library(base)
library(plyr)
library(dplyr)

# Set Work environment
setwd("C:\\Users\\david\\OneDrive\\Documenten\\MADLs\\Omega100\\r0.01")

# Importing datasets
NumberOfParticles_Run1 <- read.table(file = "Omega100_r0.01_Run1.txt", header = FALSE, sep="", dec=",")
NumberOfParticles_Run2 <- read.table(file = "Omega100_r0.01_Run2.txt", header = FALSE, sep="", dec=",")
NumberOfParticles_Run3 <- read.table(file = "Omega100_r0.01_Run3.txt", header = FALSE, sep="", dec=",")
NumberOfParticles_Run4 <- read.table(file = "Omega100_r0.01_Run4.txt", header = FALSE, sep="", dec=",")
NumberOfParticles_Run5 <- read.table(file = "Omega100_r0.01_Run5.txt", header = FALSE, sep="", dec=",")
Dataset_Run1 <- read.table(file = "RTimesteps_r0.01\\Dataset_Run1.txt", header = FALSE, sep="", dec=".")
Dataset_Run2 <- read.table(file = "RTimesteps_r0.01\\Dataset_Run2.txt", header = FALSE, sep="", dec=".")
Dataset_Run3 <- read.table(file = "RTimesteps_r0.01\\Dataset_Run3.txt", header = FALSE, sep="", dec=".")
Dataset_Run4 <- read.table(file = "RTimesteps_r0.01\\Dataset_Run4.txt", header = FALSE, sep="", dec=".")
Dataset_Run5 <- read.table(file = "RTimesteps_r0.01\\Dataset_Run5.txt", header = FALSE, sep="", dec=".")
Dataset_Run6 <- read.table(file = "RTimesteps_r0.01\\Dataset_Combined.txt", header = FALSE, sep="", dec=".")
Size <- NumberOfParticles_Run2$V1
Size2 <- log10(Size)
##############################
```

```
#         Create Vectors         #
##################################
#Run1_TimeVectors
Time1_Sca_Run1 <- Dataset_Run1$V1[1]
Time2_Sca_Run1 <- Dataset_Run1$V1[2]
Time3_Sca_Run1 <- Dataset_Run1$V1[3]
Time4_Sca_Run1 <- Dataset_Run1$V1[4]
Time5_Sca_Run1 <- Dataset_Run1$V1[5]
Time6_Sca_Run1 <- Dataset_Run1$V1[6]
Time7_Sca_Run1 <- Dataset_Run1$V1[7]
Time8_Sca_Run1 <- Dataset_Run1$V1[8]
Time9_Sca_Run1 <- Dataset_Run1$V1[9]
Time10_Sca_Run1 <- Dataset_Run1$V1[10]
Time11_Sca_Run1 <- Dataset_Run1$V1[11]
Time12_Sca_Run1 <- Dataset_Run1$V1[12]
Time13_Sca_Run1 <- Dataset_Run1$V1[13]
Time14_Sca_Run1 <- Dataset_Run1$V1[14]
Time15_Sca_Run1 <- Dataset_Run1$V1[15]
Time16_Sca_Run1 <- Dataset_Run1$V1[16]
Time17_Sca_Run1 <- Dataset_Run1$V1[17]
Time18_Sca_Run1 <- Dataset_Run1$V1[18]
Time19_Sca_Run1 <- Dataset_Run1$V1[19]
Time20_Sca_Run1 <- Dataset_Run1$V1[20]
Time21_Sca_Run1 <- Dataset_Run1$V1[21]
Time22_Sca_Run1 <- Dataset_Run1$V1[22]
Time23_Sca_Run1 <- Dataset_Run1$V1[23]
Time24_Sca_Run1 <- Dataset_Run1$V1[24]
Time25_Sca_Run1 <- Dataset_Run1$V1[25]
Time26_Sca_Run1 <- Dataset_Run1$V1[26]
Time27_Sca_Run1 <- Dataset_Run1$V1[27]
Time28_Sca_Run1 <- Dataset_Run1$V1[28]
Time29_Sca_Run1 <- Dataset_Run1$V1[29]
Time30_Sca_Run1 <- Dataset_Run1$V1[30]
Time31_Sca_Run1 <- Dataset_Run1$V1[31]
Time32_Sca_Run1 <- Dataset_Run1$V1[32]
Time33_Sca_Run1 <- Dataset_Run1$V1[33]
Time34_Sca_Run1 <- Dataset_Run1$V1[34]
Time35_Sca_Run1 <- Dataset_Run1$V1[35]
Time36_Sca_Run1 <- Dataset_Run1$V1[36]
Time37_Sca_Run1 <- Dataset_Run1$V1[37]
Time38_Sca_Run1 <- Dataset_Run1$V1[38]
Time39_Sca_Run1 <- Dataset_Run1$V1[39]
Time40_Sca_Run1 <- Dataset_Run1$V1[40]
Time41_Sca_Run1 <- Dataset_Run1$V1[41]
Time42_Sca_Run1 <- Dataset_Run1$V1[42]
Time43_Sca_Run1 <- Dataset_Run1$V1[43]
Time44_Sca_Run1 <- Dataset_Run1$V1[44]
Time45_Sca_Run1 <- Dataset_Run1$V1[45]

Time1_Vec_Run1 <- rep(Time1_Sca_Run1, each=150)
Time2_Vec_Run1 <- rep(Time2_Sca_Run1, each=150)
Time3_Vec_Run1 <- rep(Time3_Sca_Run1, each=150)
Time4_Vec_Run1 <- rep(Time4_Sca_Run1, each=150)
Time5_Vec_Run1 <- rep(Time5_Sca_Run1, each=150)
Time6_Vec_Run1 <- rep(Time6_Sca_Run1, each=150)
Time7_Vec_Run1 <- rep(Time7_Sca_Run1, each=150)
Time8_Vec_Run1 <- rep(Time8_Sca_Run1, each=150)
Time9_Vec_Run1 <- rep(Time9_Sca_Run1, each=150)
Time10_Vec_Run1 <- rep(Time10_Sca_Run1, each=150)
Time11_Vec_Run1 <- rep(Time11_Sca_Run1, each=150)
Time12_Vec_Run1 <- rep(Time12_Sca_Run1, each=150)
Time13_Vec_Run1 <- rep(Time13_Sca_Run1, each=150)
Time14_Vec_Run1 <- rep(Time14_Sca_Run1, each=150)
Time15_Vec_Run1 <- rep(Time15_Sca_Run1, each=150)
Time16_Vec_Run1 <- rep(Time16_Sca_Run1, each=150)
Time17_Vec_Run1 <- rep(Time17_Sca_Run1, each=150)
Time18_Vec_Run1 <- rep(Time18_Sca_Run1, each=150)
Time19_Vec_Run1 <- rep(Time19_Sca_Run1, each=150)
Time20_Vec_Run1 <- rep(Time20_Sca_Run1, each=150)
Time21_Vec_Run1 <- rep(Time21_Sca_Run1, each=150)
Time22_Vec_Run1 <- rep(Time22_Sca_Run1, each=150)
Time23_Vec_Run1 <- rep(Time23_Sca_Run1, each=150)
Time24_Vec_Run1 <- rep(Time24_Sca_Run1, each=150)
Time25_Vec_Run1 <- rep(Time25_Sca_Run1, each=150)
Time26_Vec_Run1 <- rep(Time26_Sca_Run1, each=150)
Time27_Vec_Run1 <- rep(Time27_Sca_Run1, each=150)
Time28_Vec_Run1 <- rep(Time28_Sca_Run1, each=150)
Time29_Vec_Run1 <- rep(Time29_Sca_Run1, each=150)
Time30_Vec_Run1 <- rep(Time30_Sca_Run1, each=150)
Time31_Vec_Run1 <- rep(Time31_Sca_Run1, each=150)
Time32_Vec_Run1 <- rep(Time32_Sca_Run1, each=150)
Time33_Vec_Run1 <- rep(Time33_Sca_Run1, each=150)
Time34_Vec_Run1 <- rep(Time34_Sca_Run1, each=150)
Time35_Vec_Run1 <- rep(Time35_Sca_Run1, each=150)
Time36_Vec_Run1 <- rep(Time36_Sca_Run1, each=150)
Time37_Vec_Run1 <- rep(Time37_Sca_Run1, each=150)
Time38_Vec_Run1 <- rep(Time38_Sca_Run1, each=150)
Time39_Vec_Run1 <- rep(Time39_Sca_Run1, each=150)
Time40_Vec_Run1 <- rep(Time40_Sca_Run1, each=150)
Time41_Vec_Run1 <- rep(Time41_Sca_Run1, each=150)
Time42_Vec_Run1 <- rep(Time42_Sca_Run1, each=150)
Time43_Vec_Run1 <- rep(Time43_Sca_Run1, each=150)
Time44_Vec_Run1 <- rep(Time44_Sca_Run1, each=150)
Time45_Vec_Run1 <- rep(Time45_Sca_Run1, each=150)

# #Run2_Timevectors
```

```
Time1_Sca_Run2 <- Dataset_Run2$V1[1]
Time2_Sca_Run2 <- Dataset_Run2$V1[2]
Time3_Sca_Run2 <- Dataset_Run2$V1[3]
Time4_Sca_Run2 <- Dataset_Run2$V1[4]
Time5_Sca_Run2 <- Dataset_Run2$V1[5]
Time6_Sca_Run2 <- Dataset_Run2$V1[6]
Time7_Sca_Run2 <- Dataset_Run2$V1[7]
Time8_Sca_Run2 <- Dataset_Run2$V1[8]
Time9_Sca_Run2 <- Dataset_Run2$V1[9]
Time10_Sca_Run2 <- Dataset_Run2$V1[10]
Time11_Sca_Run2 <- Dataset_Run2$V1[11]
Time12_Sca_Run2 <- Dataset_Run2$V1[12]
Time13_Sca_Run2 <- Dataset_Run2$V1[13]
Time14_Sca_Run2 <- Dataset_Run2$V1[14]
Time15_Sca_Run2 <- Dataset_Run2$V1[15]
Time16_Sca_Run2 <- Dataset_Run2$V1[16]
Time17_Sca_Run2 <- Dataset_Run2$V1[17]
Time18_Sca_Run2 <- Dataset_Run2$V1[18]
Time19_Sca_Run2 <- Dataset_Run2$V1[19]
Time20_Sca_Run2 <- Dataset_Run2$V1[20]
Time21_Sca_Run2 <- Dataset_Run2$V1[21]
Time22_Sca_Run2 <- Dataset_Run2$V1[22]
Time23_Sca_Run2 <- Dataset_Run2$V1[23]
Time24_Sca_Run2 <- Dataset_Run2$V1[24]
Time25_Sca_Run2 <- Dataset_Run2$V1[25]
Time26_Sca_Run2 <- Dataset_Run2$V1[26]
Time27_Sca_Run2 <- Dataset_Run2$V1[27]
Time28_Sca_Run2 <- Dataset_Run2$V1[28]
Time29_Sca_Run2 <- Dataset_Run2$V1[29]
Time30_Sca_Run2 <- Dataset_Run2$V1[30]
Time31_Sca_Run2 <- Dataset_Run2$V1[31]
Time32_Sca_Run2 <- Dataset_Run2$V1[32]
Time33_Sca_Run2 <- Dataset_Run2$V1[33]
Time34_Sca_Run2 <- Dataset_Run2$V1[34]
Time35_Sca_Run2 <- Dataset_Run2$V1[35]
Time36_Sca_Run2 <- Dataset_Run2$V1[36]
Time37_Sca_Run2 <- Dataset_Run2$V1[37]
Time38_Sca_Run2 <- Dataset_Run2$V1[38]
Time39_Sca_Run2 <- Dataset_Run2$V1[39]
Time40_Sca_Run2 <- Dataset_Run2$V1[40]
Time41_Sca_Run2 <- Dataset_Run2$V1[41]
Time42_Sca_Run2 <- Dataset_Run2$V1[42]
Time43_Sca_Run2 <- Dataset_Run2$V1[43]
Time44_Sca_Run2 <- Dataset_Run2$V1[44]
Time45_Sca_Run2 <- Dataset_Run2$V1[45]

Time1_Vec_Run2 <- rep(Time1_Sca_Run2, each=150)
Time2_Vec_Run2 <- rep(Time2_Sca_Run2, each=150)
Time3_Vec_Run2 <- rep(Time3_Sca_Run2, each=150)
Time4_Vec_Run2 <- rep(Time4_Sca_Run2, each=150)
Time5_Vec_Run2 <- rep(Time5_Sca_Run2, each=150)
Time6_Vec_Run2 <- rep(Time6_Sca_Run2, each=150)
Time7_Vec_Run2 <- rep(Time7_Sca_Run2, each=150)
Time8_Vec_Run2 <- rep(Time8_Sca_Run2, each=150)
Time9_Vec_Run2 <- rep(Time9_Sca_Run2, each=150)
Time10_Vec_Run2 <- rep(Time10_Sca_Run2, each=150)
Time11_Vec_Run2 <- rep(Time11_Sca_Run2, each=150)
Time12_Vec_Run2 <- rep(Time12_Sca_Run2, each=150)
Time13_Vec_Run2 <- rep(Time13_Sca_Run2, each=150)
Time14_Vec_Run2 <- rep(Time14_Sca_Run2, each=150)
Time15_Vec_Run2 <- rep(Time15_Sca_Run2, each=150)
Time16_Vec_Run2 <- rep(Time16_Sca_Run2, each=150)
Time17_Vec_Run2 <- rep(Time17_Sca_Run2, each=150)
Time18_Vec_Run2 <- rep(Time18_Sca_Run2, each=150)
Time19_Vec_Run2 <- rep(Time19_Sca_Run2, each=150)
Time20_Vec_Run2 <- rep(Time20_Sca_Run2, each=150)
Time21_Vec_Run2 <- rep(Time21_Sca_Run2, each=150)
Time22_Vec_Run2 <- rep(Time22_Sca_Run2, each=150)
Time23_Vec_Run2 <- rep(Time23_Sca_Run2, each=150)
Time24_Vec_Run2 <- rep(Time24_Sca_Run2, each=150)
Time25_Vec_Run2 <- rep(Time25_Sca_Run2, each=150)
Time26_Vec_Run2 <- rep(Time26_Sca_Run2, each=150)
Time27_Vec_Run2 <- rep(Time27_Sca_Run2, each=150)
Time28_Vec_Run2 <- rep(Time28_Sca_Run2, each=150)
Time29_Vec_Run2 <- rep(Time29_Sca_Run2, each=150)
Time30_Vec_Run2 <- rep(Time30_Sca_Run2, each=150)
Time31_Vec_Run2 <- rep(Time31_Sca_Run2, each=150)
Time32_Vec_Run2 <- rep(Time32_Sca_Run2, each=150)
Time33_Vec_Run2 <- rep(Time33_Sca_Run2, each=150)
Time34_Vec_Run2 <- rep(Time34_Sca_Run2, each=150)
Time35_Vec_Run2 <- rep(Time35_Sca_Run2, each=150)
Time36_Vec_Run2 <- rep(Time36_Sca_Run2, each=150)
Time37_Vec_Run2 <- rep(Time37_Sca_Run2, each=150)
Time38_Vec_Run2 <- rep(Time38_Sca_Run2, each=150)
Time39_Vec_Run2 <- rep(Time39_Sca_Run2, each=150)
Time40_Vec_Run2 <- rep(Time40_Sca_Run2, each=150)
Time41_Vec_Run2 <- rep(Time41_Sca_Run2, each=150)
Time42_Vec_Run2 <- rep(Time42_Sca_Run2, each=150)
Time43_Vec_Run2 <- rep(Time43_Sca_Run2, each=150)
Time44_Vec_Run2 <- rep(Time44_Sca_Run2, each=150)
Time45_Vec_Run2 <- rep(Time45_Sca_Run2, each=150)
#
# #Run3_TimeVectors
Time1_Sca_Run3 <- Dataset_Run3$V1[1]
Time2_Sca_Run3 <- Dataset_Run3$V1[2]
Time3_Sca_Run3 <- Dataset_Run3$V1[3]
```

```
Time4_Sca_Run3 <- Dataset_Run3$V1[4]
Time5_Sca_Run3 <- Dataset_Run3$V1[5]
Time6_Sca_Run3 <- Dataset_Run3$V1[6]
Time7_Sca_Run3 <- Dataset_Run3$V1[7]
Time8_Sca_Run3 <- Dataset_Run3$V1[8]
Time9_Sca_Run3 <- Dataset_Run3$V1[9]
Time10_Sca_Run3 <- Dataset_Run3$V1[10]
Time11_Sca_Run3 <- Dataset_Run3$V1[11]
Time12_Sca_Run3 <- Dataset_Run3$V1[12]
Time13_Sca_Run3 <- Dataset_Run3$V1[13]
Time14_Sca_Run3 <- Dataset_Run3$V1[14]
Time15_Sca_Run3 <- Dataset_Run3$V1[15]
Time16_Sca_Run3 <- Dataset_Run3$V1[16]
Time17_Sca_Run3 <- Dataset_Run3$V1[17]
Time18_Sca_Run3 <- Dataset_Run3$V1[18]
Time19_Sca_Run3 <- Dataset_Run3$V1[19]
Time20_Sca_Run3 <- Dataset_Run3$V1[20]
Time21_Sca_Run3 <- Dataset_Run3$V1[21]
Time22_Sca_Run3 <- Dataset_Run3$V1[22]
Time23_Sca_Run3 <- Dataset_Run3$V1[23]
Time24_Sca_Run3 <- Dataset_Run3$V1[24]
Time25_Sca_Run3 <- Dataset_Run3$V1[25]
Time26_Sca_Run3 <- Dataset_Run3$V1[26]
Time27_Sca_Run3 <- Dataset_Run3$V1[27]
Time28_Sca_Run3 <- Dataset_Run3$V1[28]
Time29_Sca_Run3 <- Dataset_Run3$V1[29]
Time30_Sca_Run3 <- Dataset_Run3$V1[30]
Time31_Sca_Run3 <- Dataset_Run3$V1[31]
Time32_Sca_Run3 <- Dataset_Run3$V1[32]
Time33_Sca_Run3 <- Dataset_Run3$V1[33]
Time34_Sca_Run3 <- Dataset_Run3$V1[34]
Time35_Sca_Run3 <- Dataset_Run3$V1[35]
Time36_Sca_Run3 <- Dataset_Run3$V1[36]
Time37_Sca_Run3 <- Dataset_Run3$V1[37]
Time38_Sca_Run3 <- Dataset_Run3$V1[38]
Time39_Sca_Run3 <- Dataset_Run3$V1[39]
Time40_Sca_Run3 <- Dataset_Run3$V1[40]
Time41_Sca_Run3 <- Dataset_Run3$V1[41]
Time42_Sca_Run3 <- Dataset_Run3$V1[42]
Time43_Sca_Run3 <- Dataset_Run3$V1[43]
Time44_Sca_Run3 <- Dataset_Run3$V1[44]
Time45_Sca_Run3 <- Dataset_Run3$V1[45]

Time1_Vec_Run3 <- rep(Time1_Sca_Run3, each=150)
Time2_Vec_Run3 <- rep(Time2_Sca_Run3, each=150)
Time3_Vec_Run3 <- rep(Time3_Sca_Run3, each=150)
Time4_Vec_Run3 <- rep(Time4_Sca_Run3, each=150)
Time5_Vec_Run3 <- rep(Time5_Sca_Run3, each=150)
Time6_Vec_Run3 <- rep(Time6_Sca_Run3, each=150)
Time7_Vec_Run3 <- rep(Time7_Sca_Run3, each=150)
Time8_Vec_Run3 <- rep(Time8_Sca_Run3, each=150)
Time9_Vec_Run3 <- rep(Time9_Sca_Run3, each=150)
Time10_Vec_Run3 <- rep(Time10_Sca_Run3, each=150)
Time11_Vec_Run3 <- rep(Time11_Sca_Run3, each=150)
Time12_Vec_Run3 <- rep(Time12_Sca_Run3, each=150)
Time13_Vec_Run3 <- rep(Time13_Sca_Run3, each=150)
Time14_Vec_Run3 <- rep(Time14_Sca_Run3, each=150)
Time15_Vec_Run3 <- rep(Time15_Sca_Run3, each=150)
Time16_Vec_Run3 <- rep(Time16_Sca_Run3, each=150)
Time17_Vec_Run3 <- rep(Time17_Sca_Run3, each=150)
Time18_Vec_Run3 <- rep(Time18_Sca_Run3, each=150)
Time19_Vec_Run3 <- rep(Time19_Sca_Run3, each=150)
Time20_Vec_Run3 <- rep(Time20_Sca_Run3, each=150)
Time21_Vec_Run3 <- rep(Time21_Sca_Run3, each=150)
Time22_Vec_Run3 <- rep(Time22_Sca_Run3, each=150)
Time23_Vec_Run3 <- rep(Time23_Sca_Run3, each=150)
Time24_Vec_Run3 <- rep(Time24_Sca_Run3, each=150)
Time25_Vec_Run3 <- rep(Time25_Sca_Run3, each=150)
Time26_Vec_Run3 <- rep(Time26_Sca_Run3, each=150)
Time27_Vec_Run3 <- rep(Time27_Sca_Run3, each=150)
Time28_Vec_Run3 <- rep(Time28_Sca_Run3, each=150)
Time29_Vec_Run3 <- rep(Time29_Sca_Run3, each=150)
Time30_Vec_Run3 <- rep(Time30_Sca_Run3, each=150)
Time31_Vec_Run3 <- rep(Time31_Sca_Run3, each=150)
Time32_Vec_Run3 <- rep(Time32_Sca_Run3, each=150)
Time33_Vec_Run3 <- rep(Time33_Sca_Run3, each=150)
Time34_Vec_Run3 <- rep(Time34_Sca_Run3, each=150)
Time35_Vec_Run3 <- rep(Time35_Sca_Run3, each=150)
Time36_Vec_Run3 <- rep(Time36_Sca_Run3, each=150)
Time37_Vec_Run3 <- rep(Time37_Sca_Run3, each=150)
Time38_Vec_Run3 <- rep(Time38_Sca_Run3, each=150)
Time39_Vec_Run3 <- rep(Time39_Sca_Run3, each=150)
Time40_Vec_Run3 <- rep(Time40_Sca_Run3, each=150)
Time41_Vec_Run3 <- rep(Time41_Sca_Run3, each=150)
Time42_Vec_Run3 <- rep(Time42_Sca_Run3, each=150)
Time43_Vec_Run3 <- rep(Time43_Sca_Run3, each=150)
Time44_Vec_Run3 <- rep(Time44_Sca_Run3, each=150)
Time45_Vec_Run3 <- rep(Time45_Sca_Run3, each=150)
#
#Run4_TimeVectors
Time1_Sca_Run4 <- Dataset_Run4$V1[1]
Time2_Sca_Run4 <- Dataset_Run4$V1[2]
Time3_Sca_Run4 <- Dataset_Run4$V1[3]
Time4_Sca_Run4 <- Dataset_Run4$V1[4]
Time5_Sca_Run4 <- Dataset_Run4$V1[5]
Time6_Sca_Run4 <- Dataset_Run4$V1[6]
```

```
Time7_Sca_Run4 <- Dataset_Run4$V1[7]
Time8_Sca_Run4 <- Dataset_Run4$V1[8]
Time9_Sca_Run4 <- Dataset_Run4$V1[9]
Time10_Sca_Run4 <- Dataset_Run4$V1[10]
Time11_Sca_Run4 <- Dataset_Run4$V1[11]
Time12_Sca_Run4 <- Dataset_Run4$V1[12]
Time13_Sca_Run4 <- Dataset_Run4$V1[13]
Time14_Sca_Run4 <- Dataset_Run4$V1[14]
Time15_Sca_Run4 <- Dataset_Run4$V1[15]
Time16_Sca_Run4 <- Dataset_Run4$V1[16]
Time17_Sca_Run4 <- Dataset_Run4$V1[17]
Time18_Sca_Run4 <- Dataset_Run4$V1[18]
Time19_Sca_Run4 <- Dataset_Run4$V1[19]
Time20_Sca_Run4 <- Dataset_Run4$V1[20]
Time21_Sca_Run4 <- Dataset_Run4$V1[21]
Time22_Sca_Run4 <- Dataset_Run4$V1[22]
Time23_Sca_Run4 <- Dataset_Run4$V1[23]
Time24_Sca_Run4 <- Dataset_Run4$V1[24]
Time25_Sca_Run4 <- Dataset_Run4$V1[25]
Time26_Sca_Run4 <- Dataset_Run4$V1[26]
Time27_Sca_Run4 <- Dataset_Run4$V1[27]
Time28_Sca_Run4 <- Dataset_Run4$V1[28]
Time29_Sca_Run4 <- Dataset_Run4$V1[29]
Time30_Sca_Run4 <- Dataset_Run4$V1[30]
Time31_Sca_Run4 <- Dataset_Run4$V1[31]
Time32_Sca_Run4 <- Dataset_Run4$V1[32]
Time33_Sca_Run4 <- Dataset_Run4$V1[33]
Time34_Sca_Run4 <- Dataset_Run4$V1[34]
Time35_Sca_Run4 <- Dataset_Run4$V1[35]
Time36_Sca_Run4 <- Dataset_Run4$V1[36]
Time37_Sca_Run4 <- Dataset_Run4$V1[37]
Time38_Sca_Run4 <- Dataset_Run4$V1[38]
Time39_Sca_Run4 <- Dataset_Run4$V1[39]
Time40_Sca_Run4 <- Dataset_Run4$V1[40]
Time41_Sca_Run4 <- Dataset_Run4$V1[41]
Time42_Sca_Run4 <- Dataset_Run4$V1[42]
Time43_Sca_Run4 <- Dataset_Run4$V1[43]
Time44_Sca_Run4 <- Dataset_Run4$V1[44]
Time45_Sca_Run4 <- Dataset_Run4$V1[45]

Time1_Vec_Run4 <- rep(Time1_Sca_Run4, each=150)
Time2_Vec_Run4 <- rep(Time2_Sca_Run4, each=150)
Time3_Vec_Run4 <- rep(Time3_Sca_Run4, each=150)
Time4_Vec_Run4 <- rep(Time4_Sca_Run4, each=150)
Time5_Vec_Run4 <- rep(Time5_Sca_Run4, each=150)
Time6_Vec_Run4 <- rep(Time6_Sca_Run4, each=150)
Time7_Vec_Run4 <- rep(Time7_Sca_Run4, each=150)
Time8_Vec_Run4 <- rep(Time8_Sca_Run4, each=150)
Time9_Vec_Run4 <- rep(Time9_Sca_Run4, each=150)
Time10_Vec_Run4 <- rep(Time10_Sca_Run4, each=150)
Time11_Vec_Run4 <- rep(Time11_Sca_Run4, each=150)
Time12_Vec_Run4 <- rep(Time12_Sca_Run4, each=150)
Time13_Vec_Run4 <- rep(Time13_Sca_Run4, each=150)
Time14_Vec_Run4 <- rep(Time14_Sca_Run4, each=150)
Time15_Vec_Run4 <- rep(Time15_Sca_Run4, each=150)
Time16_Vec_Run4 <- rep(Time16_Sca_Run4, each=150)
Time17_Vec_Run4 <- rep(Time17_Sca_Run4, each=150)
Time18_Vec_Run4 <- rep(Time18_Sca_Run4, each=150)
Time19_Vec_Run4 <- rep(Time19_Sca_Run4, each=150)
Time20_Vec_Run4 <- rep(Time20_Sca_Run4, each=150)
Time21_Vec_Run4 <- rep(Time21_Sca_Run4, each=150)
Time22_Vec_Run4 <- rep(Time22_Sca_Run4, each=150)
Time23_Vec_Run4 <- rep(Time23_Sca_Run4, each=150)
Time24_Vec_Run4 <- rep(Time24_Sca_Run4, each=150)
Time25_Vec_Run4 <- rep(Time25_Sca_Run4, each=150)
Time26_Vec_Run4 <- rep(Time26_Sca_Run4, each=150)
Time27_Vec_Run4 <- rep(Time27_Sca_Run4, each=150)
Time28_Vec_Run4 <- rep(Time28_Sca_Run4, each=150)
Time29_Vec_Run4 <- rep(Time29_Sca_Run4, each=150)
Time30_Vec_Run4 <- rep(Time30_Sca_Run4, each=150)
Time31_Vec_Run4 <- rep(Time31_Sca_Run4, each=150)
Time32_Vec_Run4 <- rep(Time32_Sca_Run4, each=150)
Time33_Vec_Run4 <- rep(Time33_Sca_Run4, each=150)
Time34_Vec_Run4 <- rep(Time34_Sca_Run4, each=150)
Time35_Vec_Run4 <- rep(Time35_Sca_Run4, each=150)
Time36_Vec_Run4 <- rep(Time36_Sca_Run4, each=150)
Time37_Vec_Run4 <- rep(Time37_Sca_Run4, each=150)
Time38_Vec_Run4 <- rep(Time38_Sca_Run4, each=150)
Time39_Vec_Run4 <- rep(Time39_Sca_Run4, each=150)
Time40_Vec_Run4 <- rep(Time40_Sca_Run4, each=150)
Time41_Vec_Run4 <- rep(Time41_Sca_Run4, each=150)
Time42_Vec_Run4 <- rep(Time42_Sca_Run4, each=150)
Time43_Vec_Run4 <- rep(Time43_Sca_Run4, each=150)
Time44_Vec_Run4 <- rep(Time44_Sca_Run4, each=150)
Time45_Vec_Run4 <- rep(Time45_Sca_Run4, each=150)
#
# #Run5_TimeVectors
Time1_Sca_Run5 <- Dataset_Run5$V1[1]
Time2_Sca_Run5 <- Dataset_Run5$V1[2]
Time3_Sca_Run5 <- Dataset_Run5$V1[3]
Time4_Sca_Run5 <- Dataset_Run5$V1[4]
Time5_Sca_Run5 <- Dataset_Run5$V1[5]
Time6_Sca_Run5 <- Dataset_Run5$V1[6]
Time7_Sca_Run5 <- Dataset_Run5$V1[7]
Time8_Sca_Run5 <- Dataset_Run5$V1[8]
Time9_Sca_Run5 <- Dataset_Run5$V1[9]
```

```
Time10_Sca_Run5 <- Dataset_Run5$V1[10]
Time11_Sca_Run5 <- Dataset_Run5$V1[11]
Time12_Sca_Run5 <- Dataset_Run5$V1[12]
Time13_Sca_Run5 <- Dataset_Run5$V1[13]
Time14_Sca_Run5 <- Dataset_Run5$V1[14]
Time15_Sca_Run5 <- Dataset_Run5$V1[15]
Time16_Sca_Run5 <- Dataset_Run5$V1[16]
Time17_Sca_Run5 <- Dataset_Run5$V1[17]
Time18_Sca_Run5 <- Dataset_Run5$V1[18]
Time19_Sca_Run5 <- Dataset_Run5$V1[19]
Time20_Sca_Run5 <- Dataset_Run5$V1[20]
Time21_Sca_Run5 <- Dataset_Run5$V1[21]
Time22_Sca_Run5 <- Dataset_Run5$V1[22]
Time23_Sca_Run5 <- Dataset_Run5$V1[23]
Time24_Sca_Run5 <- Dataset_Run5$V1[24]
Time25_Sca_Run5 <- Dataset_Run5$V1[25]
Time26_Sca_Run5 <- Dataset_Run5$V1[26]
Time27_Sca_Run5 <- Dataset_Run5$V1[27]
Time28_Sca_Run5 <- Dataset_Run5$V1[28]
Time29_Sca_Run5 <- Dataset_Run5$V1[29]
Time30_Sca_Run5 <- Dataset_Run5$V1[30]
Time31_Sca_Run5 <- Dataset_Run5$V1[31]
Time32_Sca_Run5 <- Dataset_Run5$V1[32]
Time33_Sca_Run5 <- Dataset_Run5$V1[33]
Time34_Sca_Run5 <- Dataset_Run5$V1[34]
Time35_Sca_Run5 <- Dataset_Run5$V1[35]
Time36_Sca_Run5 <- Dataset_Run5$V1[36]
Time37_Sca_Run5 <- Dataset_Run5$V1[37]
Time38_Sca_Run5 <- Dataset_Run5$V1[38]
Time39_Sca_Run5 <- Dataset_Run5$V1[39]
Time40_Sca_Run5 <- Dataset_Run5$V1[40]
Time41_Sca_Run5 <- Dataset_Run5$V1[41]
Time42_Sca_Run5 <- Dataset_Run5$V1[42]
Time43_Sca_Run5 <- Dataset_Run5$V1[43]
Time44_Sca_Run5 <- Dataset_Run5$V1[44]
Time45_Sca_Run5 <- Dataset_Run5$V1[45]

Time1_Vec_Run5 <- rep(Time1_Sca_Run5, each=150)
Time2_Vec_Run5 <- rep(Time2_Sca_Run5, each=150)
Time3_Vec_Run5 <- rep(Time3_Sca_Run5, each=150)
Time4_Vec_Run5 <- rep(Time4_Sca_Run5, each=150)
Time5_Vec_Run5 <- rep(Time5_Sca_Run5, each=150)
Time6_Vec_Run5 <- rep(Time6_Sca_Run5, each=150)
Time7_Vec_Run5 <- rep(Time7_Sca_Run5, each=150)
Time8_Vec_Run5 <- rep(Time8_Sca_Run5, each=150)
Time9_Vec_Run5 <- rep(Time9_Sca_Run5, each=150)
Time10_Vec_Run5 <- rep(Time10_Sca_Run5, each=150)
Time11_Vec_Run5 <- rep(Time11_Sca_Run5, each=150)
Time12_Vec_Run5 <- rep(Time12_Sca_Run5, each=150)
Time13_Vec_Run5 <- rep(Time13_Sca_Run5, each=150)
Time14_Vec_Run5 <- rep(Time14_Sca_Run5, each=150)
Time15_Vec_Run5 <- rep(Time15_Sca_Run5, each=150)
Time16_Vec_Run5 <- rep(Time16_Sca_Run5, each=150)
Time17_Vec_Run5 <- rep(Time17_Sca_Run5, each=150)
Time18_Vec_Run5 <- rep(Time18_Sca_Run5, each=150)
Time19_Vec_Run5 <- rep(Time19_Sca_Run5, each=150)
Time20_Vec_Run5 <- rep(Time20_Sca_Run5, each=150)
Time21_Vec_Run5 <- rep(Time21_Sca_Run5, each=150)
Time22_Vec_Run5 <- rep(Time22_Sca_Run5, each=150)
Time23_Vec_Run5 <- rep(Time23_Sca_Run5, each=150)
Time24_Vec_Run5 <- rep(Time24_Sca_Run5, each=150)
Time25_Vec_Run5 <- rep(Time25_Sca_Run5, each=150)
Time26_Vec_Run5 <- rep(Time26_Sca_Run5, each=150)
Time27_Vec_Run5 <- rep(Time27_Sca_Run5, each=150)
Time28_Vec_Run5 <- rep(Time28_Sca_Run5, each=150)
Time29_Vec_Run5 <- rep(Time29_Sca_Run5, each=150)
Time30_Vec_Run5 <- rep(Time30_Sca_Run5, each=150)
Time31_Vec_Run5 <- rep(Time31_Sca_Run5, each=150)
Time32_Vec_Run5 <- rep(Time32_Sca_Run5, each=150)
Time33_Vec_Run5 <- rep(Time33_Sca_Run5, each=150)
Time34_Vec_Run5 <- rep(Time34_Sca_Run5, each=150)
Time35_Vec_Run5 <- rep(Time35_Sca_Run5, each=150)
Time36_Vec_Run5 <- rep(Time36_Sca_Run5, each=150)
Time37_Vec_Run5 <- rep(Time37_Sca_Run5, each=150)
Time38_Vec_Run5 <- rep(Time38_Sca_Run5, each=150)
Time39_Vec_Run5 <- rep(Time39_Sca_Run5, each=150)
Time40_Vec_Run5 <- rep(Time40_Sca_Run5, each=150)
Time41_Vec_Run5 <- rep(Time41_Sca_Run5, each=150)
Time42_Vec_Run5 <- rep(Time42_Sca_Run5, each=150)
Time43_Vec_Run5 <- rep(Time43_Sca_Run5, each=150)
Time44_Vec_Run5 <- rep(Time44_Sca_Run5, each=150)
Time45_Vec_Run5 <- rep(Time45_Sca_Run5, each=150)
#Run1_graph
tiff("Run1_r0.01_Omega100_Grid_MADLS_Intensity.tiff", units="in", width=5, height=5, res=300)

Time_Vec1 <- as.data.frame(c(Time1_Vec_Run1, Time2_Vec_Run1, Time3_Vec_Run1, Time4_Vec_Run1, Time5_Vec
    _Run1, Time6_Vec_Run1, Time7_Vec_Run1,
                             Time8_Vec_Run1, Time9_Vec_Run1, Time10_Vec_Run1, Time11_Vec_Run1, Time12_
                                 Vec_Run1, Time13_Vec_Run1, Time14_Vec_Run1,
                             Time15_Vec_Run1, Time16_Vec_Run1, Time17_Vec_Run1, Time18_Vec_Run1,
                                 Time19_Vec_Run1, Time20_Vec_Run1, Time21_Vec_Run1,
                             Time22_Vec_Run1, Time23_Vec_Run1, Time24_Vec_Run1, Time25_Vec_Run1,
                                 Time26_Vec_Run1, Time27_Vec_Run1, Time28_Vec_Run1,
                             Time29_Vec_Run1, Time30_Vec_Run1, Time31_Vec_Run1, Time32_Vec_Run1,
                                 Time33_Vec_Run1, Time34_Vec_Run1, Time35_Vec_Run1,
                             Time36_Vec_Run1, Time37_Vec_Run1, Time38_Vec_Run1, Time39_Vec_Run1,
```

```
                                Time40_Vec_Run1, Time41_Vec_Run1, Time42_Vec_Run1,
                              Time43_Vec_Run1, Time44_Vec_Run1, Time45_Vec_Run1))
Size_Vec1 <- as.data.frame(c(Size2, Size2, Size2, Size2, Size2, Size2, Size2, Size2, Size2, Size2,
    Size2, Size2,
                              Size2, Size2, Size2, Size2, Size2, Size2, Size2, Size2, Size2, Size2,
                                  Size2, Size2,
                              Size2, Size2, Size2, Size2, Size2, Size2, Size2, Size2, Size2, Size2,
                                  Size2, Size2,
                              Size2, Size2, Size2, Size2, Size2, Size2, Size2, Size2, Size2))
Number_Vec1 <- as.data.frame(c(NumberOfParticles_Run1$V2, NumberOfParticles_Run1$V3, NumberOfParticles
    _Run1$V4, NumberOfParticles_Run1$V5, NumberOfParticles_Run1$V6, NumberOfParticles_Run1$V7,
    NumberOfParticles_Run1$V8,
                                NumberOfParticles_Run1$V9, NumberOfParticles_Run1$V10,
                                    NumberOfParticles_Run1$V11, NumberOfParticles_Run1$V12,
                                    NumberOfParticles_Run1$V13, NumberOfParticles_Run1$V14,
                                    NumberOfParticles_Run1$V15,
                                NumberOfParticles_Run1$V16, NumberOfParticles_Run1$V17,
                                    NumberOfParticles_Run1$V18, NumberOfParticles_Run1$V19,
                                    NumberOfParticles_Run1$V20, NumberOfParticles_Run1$V21,
                                    NumberOfParticles_Run1$V22,
                                NumberOfParticles_Run1$V23, NumberOfParticles_Run1$V24,
                                    NumberOfParticles_Run1$V25, NumberOfParticles_Run1$V26,
                                    NumberOfParticles_Run1$V27, NumberOfParticles_Run1$V28,
                                    NumberOfParticles_Run1$V29,
                                NumberOfParticles_Run1$V30, NumberOfParticles_Run1$V31,
                                    NumberOfParticles_Run1$V32, NumberOfParticles_Run1$V33,
                                    NumberOfParticles_Run1$V34, NumberOfParticles_Run1$V35,
                                    NumberOfParticles_Run1$V36,
                                NumberOfParticles_Run1$V37, NumberOfParticles_Run1$V38,
                                    NumberOfParticles_Run1$V39, NumberOfParticles_Run1$V40,
                                    NumberOfParticles_Run1$V41, NumberOfParticles_Run1$V42,
                                    NumberOfParticles_Run1$V43,
                                NumberOfParticles_Run1$V44, NumberOfParticles_Run1$V45,
                                    NumberOfParticles_Run1$V46))
Dataset_Run1_2 <- as.data.frame(cbind(Time_Vec1, Size_Vec1, Number_Vec1))

write.table(Dataset_Run1_2, file="Omega100_r0.01_Run1_GRID_MADLS_Intensity.txt",
            row.names=FALSE, col.names=FALSE, sep=",")
Dataset_Run1_3 <- read.table(file = "Omega100_r0.01_Run1_GRID_MADLS_Intensity.txt", header = FALSE,
    sep=",", dec=".")

Grid_Time1 <- Dataset_Run1_3$V1
Grid_Size1 <- Dataset_Run1_3$V2
Grid_Number1 <- Dataset_Run1_3$V3


Dataset_Run1_3 %>% ggplot(aes(x = Grid_Size1, y = Grid_Time1, z = Grid_Number1, fill = Grid_Number1))
    +
  geom_raster(aes(fill=Grid_Number1)) +
  scale_y_continuous(breaks = seq(0, 10500, by = 1500)) +
  scale_fill_gradient(low="blue", high="yellow")      #limits=c(0,50)
dev.off()

#Run2_Graph
tiff("Run2_r0.01_Omega100_Grid_MADLS_Intensity.tiff", units="in", width=5, height=5, res=300)

Time_Vec2 <- as.data.frame(c(Time1_Vec_Run2, Time2_Vec_Run2, Time3_Vec_Run2, Time4_Vec_Run2, Time5_Vec
    _Run2, Time6_Vec_Run2, Time7_Vec_Run2,
                             Time8_Vec_Run2, Time9_Vec_Run2, Time10_Vec_Run2, Time11_Vec_Run2, Time12_
                                 Vec_Run2, Time13_Vec_Run2, Time14_Vec_Run2,
                             Time15_Vec_Run2, Time16_Vec_Run2, Time17_Vec_Run2, Time18_Vec_Run2, Time19
                                 _Vec_Run2, Time20_Vec_Run2, Time21_Vec_Run2,
                             Time22_Vec_Run2, Time23_Vec_Run2, Time24_Vec_Run2, Time25_Vec_Run2, Time26
                                 _Vec_Run2, Time27_Vec_Run2, Time28_Vec_Run2,
                             Time29_Vec_Run2, Time30_Vec_Run2, Time31_Vec_Run2, Time32_Vec_Run2, Time33
                                 _Vec_Run2, Time34_Vec_Run2, Time35_Vec_Run2,
                             Time36_Vec_Run2, Time37_Vec_Run2, Time38_Vec_Run2, Time39_Vec_Run2, Time40
                                 _Vec_Run2, Time41_Vec_Run2, Time42_Vec_Run2,
                             Time43_Vec_Run2, Time44_Vec_Run2, Time45_Vec_Run2))
Size_Vec2 <- as.data.frame(c(Size2, Size2, Size2, Size2, Size2, Size2, Size2, Size2, Size2, Size2,
    Size2, Size2,
                             Size2, Size2, Size2, Size2, Size2, Size2, Size2, Size2, Size2, Size2,
                                 Size2, Size2,
                             Size2, Size2, Size2, Size2, Size2, Size2, Size2, Size2, Size2, Size2,
                                 Size2, Size2,
                             Size2, Size2, Size2, Size2, Size2, Size2, Size2, Size2, Size2))
Number_Vec2 <- as.data.frame(c(NumberOfParticles_Run2$V2, NumberOfParticles_Run2$V3, NumberOfParticles
    _Run2$V4, NumberOfParticles_Run2$V5, NumberOfParticles_Run2$V6, NumberOfParticles_Run2$V7,
    NumberOfParticles_Run2$V8,
                               NumberOfParticles_Run2$V9, NumberOfParticles_Run2$V10, NumberOfParticles
                                   _Run2$V11, NumberOfParticles_Run2$V12, NumberOfParticles_Run2$V13,
                                   NumberOfParticles_Run2$V14, NumberOfParticles_Run2$V15,
                               NumberOfParticles_Run2$V16, NumberOfParticles_Run2$V17,
                                   NumberOfParticles_Run2$V18, NumberOfParticles_Run2$V19,
                                   NumberOfParticles_Run2$V20, NumberOfParticles_Run2$V21,
                                   NumberOfParticles_Run2$V22,
                               NumberOfParticles_Run2$V23, NumberOfParticles_Run2$V24,
                                   NumberOfParticles_Run2$V25, NumberOfParticles_Run2$V26,
                                   NumberOfParticles_Run2$V27, NumberOfParticles_Run2$V28,
                                   NumberOfParticles_Run2$V29,
                               NumberOfParticles_Run2$V30, NumberOfParticles_Run2$V31,
                                   NumberOfParticles_Run2$V32, NumberOfParticles_Run2$V33,
                                   NumberOfParticles_Run2$V34, NumberOfParticles_Run2$V35,
                                   NumberOfParticles_Run2$V36,
                               NumberOfParticles_Run2$V37, NumberOfParticles_Run2$V38,
                                   NumberOfParticles_Run2$V39, NumberOfParticles_Run2$V40,
```

```
                                    NumberOfParticles_Run2$V41, NumberOfParticles_Run2$V42,
                                    NumberOfParticles_Run2$V43,
                                NumberOfParticles_Run2$V44, NumberOfParticles_Run2$V45,
                                    NumberOfParticles_Run2$V46))
Dataset_Run2_2 <- as.data.frame(cbind(Time_Vec2, Size_Vec2,Number_Vec2))
write.table(Dataset_Run2_2, file="Omega100_r0.01_Run2_GRID_MADLS_Intensity.txt",
            row.names=FALSE, col.names=FALSE, sep=",", quote = FALSE)
Dataset_Run2_3 <- read.table(file = "Omega100_r0.01_Run2_GRID_MADLS_Intensity.txt", header = FALSE,
    sep=",", dec=".")

Grid_Time2 <- Dataset_Run2_3$V1
Grid_Size2 <- Dataset_Run2_3$V2
Grid_Number2 <- Dataset_Run2_3$V3

Dataset_Run2_3 %>% ggplot(aes(x = Grid_Size2, y = Grid_Time2, z = Grid_Number2, fill = Grid_Number2))
    +
  geom_raster(aes(fill=Grid_Number2)) +
  scale_y_continuous(breaks = seq(0, 13500, by = 1500)) +
  scale_fill_gradient(low="blue", high="yellow")      #limits=c(0,50)
dev.off()

#Run3_Graph
tiff("Run3_r0.01_Omega100_Grid_MADLS_Intensity.tiff", units="in", width=5, height=5, res=300)

Time_Vec3 <- as.data.frame(c(Time1_Vec_Run3, Time2_Vec_Run3, Time3_Vec_Run3, Time4_Vec_Run3, Time5_Vec
    _Run3, Time6_Vec_Run3, Time7_Vec_Run3,
                             Time8_Vec_Run3, Time9_Vec_Run3, Time10_Vec_Run3, Time11_Vec_Run3, Time12_
                                 Vec_Run3, Time13_Vec_Run3, Time14_Vec_Run3,
                             Time15_Vec_Run3, Time16_Vec_Run3, Time17_Vec_Run3, Time18_Vec_Run3,
                                 Time19_Vec_Run3, Time20_Vec_Run3, Time21_Vec_Run3,
                             Time22_Vec_Run3, Time23_Vec_Run3, Time24_Vec_Run3, Time25_Vec_Run3,
                                 Time26_Vec_Run3, Time27_Vec_Run3, Time28_Vec_Run3,
                             Time29_Vec_Run3, Time30_Vec_Run3, Time31_Vec_Run3, Time32_Vec_Run3,
                                 Time33_Vec_Run3, Time34_Vec_Run3, Time35_Vec_Run3,
                             Time36_Vec_Run3, Time37_Vec_Run3, Time38_Vec_Run3, Time39_Vec_Run3,
                                 Time39_Vec_Run3, Time41_Vec_Run3, Time42_Vec_Run3,
                             Time43_Vec_Run3, Time44_Vec_Run3, Time45_Vec_Run3))
Size_Vec3 <- as.data.frame(c(Size2, Size2, Size2, Size2, Size2, Size2, Size2, Size2, Size2, Size2,
    Size2, Size2,
                             Size2, Size2, Size2, Size2, Size2, Size2, Size2, Size2, Size2, Size2,
                                 Size2, Size2,
                             Size2, Size2, Size2, Size2, Size2, Size2, Size2, Size2, Size2, Size2,
                                 Size2, Size2,
                             Size2, Size2, Size2, Size2, Size2, Size2, Size2, Size2, Size2))
Number_Vec3<- as.data.frame(c(NumberOfParticles_Run3$V2, NumberOfParticles_Run3$V3, NumberOfParticles_
    Run3$V4, NumberOfParticles_Run3$V5, NumberOfParticles_Run3$V6, NumberOfParticles_Run3$V7,
    NumberOfParticles_Run3$V8,
                              NumberOfParticles_Run3$V9, NumberOfParticles_Run3$V10,
                                  NumberOfParticles_Run3$V11, NumberOfParticles_Run3$V12,
                                  NumberOfParticles_Run3$V13, NumberOfParticles_Run3$V14,
                                  NumberOfParticles_Run3$V15,
                              NumberOfParticles_Run3$V16, NumberOfParticles_Run3$V17,
                                  NumberOfParticles_Run3$V18, NumberOfParticles_Run3$V19,
                                  NumberOfParticles_Run3$V20, NumberOfParticles_Run3$V21,
                                  NumberOfParticles_Run3$V22,
                              NumberOfParticles_Run3$V23, NumberOfParticles_Run3$V24,
                                  NumberOfParticles_Run3$V25, NumberOfParticles_Run3$V26,
                                  NumberOfParticles_Run3$V27, NumberOfParticles_Run3$V28,
                                  NumberOfParticles_Run3$V29,
                              NumberOfParticles_Run3$V30, NumberOfParticles_Run3$V31,
                                  NumberOfParticles_Run3$V32, NumberOfParticles_Run3$V33,
                                  NumberOfParticles_Run3$V34, NumberOfParticles_Run3$V35,
                                  NumberOfParticles_Run3$V36,
                              NumberOfParticles_Run3$V37, NumberOfParticles_Run3$V38,
                                  NumberOfParticles_Run3$V39, NumberOfParticles_Run3$V40,
                                  NumberOfParticles_Run3$V41, NumberOfParticles_Run3$V42,
                                  NumberOfParticles_Run3$V43,
                              NumberOfParticles_Run3$V44, NumberOfParticles_Run3$V45,
                                  NumberOfParticles_Run3$V46))
Dataset_Run3_2 <- as.data.frame(cbind(Time_Vec3, Size_Vec3, Number_Vec3))

write.table(Dataset_Run3_2, file="Omega100_r0.01_Run3_GRID_MADLS_Intensity.txt",
            row.names=FALSE, col.names=FALSE, sep=",")
Dataset_Run3_3 <- read.table(file = "Omega100_r0.01_Run3_GRID_MADLS_Intensity.txt", header = FALSE,
    sep=",", dec=".")

Grid_Time3 <- Dataset_Run3_3$V1
Grid_Size3 <- Dataset_Run3_3$V2
Grid_Number3 <- Dataset_Run3_3$V3


Dataset_Run3_3 %>% ggplot(aes(x = Grid_Size3, y = Grid_Time3, z = Grid_Number3, fill = Grid_Number3))
    +
  geom_raster(aes(fill=Grid_Number3)) +
  scale_y_continuous(breaks = seq(0, 13500, by = 1500)) +
  scale_fill_gradient(low="blue", high="yellow")      #limits=c(0,50)
dev.off()
#Run4
tiff("Run4_r0.01_Omega100_Grid_MADLS_Intensity.tiff", units="in", width=5, height=5, res=300)

Time_Vec4 <- as.data.frame(c(Time1_Vec_Run4, Time2_Vec_Run4, Time3_Vec_Run4, Time4_Vec_Run4, Time5_Vec
    _Run4, Time6_Vec_Run4, Time7_Vec_Run4,
                             Time8_Vec_Run4, Time9_Vec_Run4, Time10_Vec_Run4, Time11_Vec_Run4, Time12_
                                 Vec_Run4, Time13_Vec_Run4, Time14_Vec_Run4,
                             Time15_Vec_Run4, Time16_Vec_Run4, Time17_Vec_Run4, Time18_Vec_Run4,
                                 Time19_Vec_Run4, Time20_Vec_Run4, Time21_Vec_Run4,
```

```
                                Time22_Vec_Run4, Time23_Vec_Run4, Time24_Vec_Run4, Time25_Vec_Run4,
                                    Time26_Vec_Run4, Time27_Vec_Run4, Time28_Vec_Run4,
                                Time29_Vec_Run4, Time30_Vec_Run4, Time31_Vec_Run4, Time32_Vec_Run4,
                                    Time33_Vec_Run4, Time34_Vec_Run4, Time35_Vec_Run4,
                                Time36_Vec_Run4, Time37_Vec_Run4, Time38_Vec_Run4, Time39_Vec_Run4,
                                    Time40_Vec_Run4, Time41_Vec_Run4, Time42_Vec_Run4,
                                Time43_Vec_Run4, Time44_Vec_Run4, Time45_Vec_Run4))
Size_Vec4 <- as.data.frame(c(Size2, Size2, Size2, Size2, Size2, Size2, Size2, Size2, Size2, Size2,
    Size2, Size2,
                                Size2, Size2, Size2, Size2, Size2, Size2, Size2, Size2, Size2, Size2,
                                    Size2, Size2,
                                Size2, Size2, Size2, Size2, Size2, Size2, Size2, Size2, Size2, Size2,
                                    Size2, Size2,
                                Size2, Size2, Size2, Size2, Size2, Size2, Size2, Size2, Size2))
Number_Vec4<- as.data.frame(c(NumberOfParticles_Run4$V2, NumberOfParticles_Run4$V3, NumberOfParticles_
    Run4$V4, NumberOfParticles_Run4$V5, NumberOfParticles_Run4$V6, NumberOfParticles_Run4$V7,
    NumberOfParticles_Run4$V8,
                                NumberOfParticles_Run4$V9, NumberOfParticles_Run4$V10, NumberOfParticles
                                    _Run4$V11, NumberOfParticles_Run4$V12, NumberOfParticles_Run4$V13,
                                    NumberOfParticles_Run4$V14, NumberOfParticles_Run4$V15,
                                NumberOfParticles_Run4$V16, NumberOfParticles_Run4$V17,
                                    NumberOfParticles_Run4$V18, NumberOfParticles_Run4$V19,
                                    NumberOfParticles_Run4$V20, NumberOfParticles_Run4$V21,
                                    NumberOfParticles_Run4$V22,
                                NumberOfParticles_Run4$V23, NumberOfParticles_Run4$V24,
                                    NumberOfParticles_Run4$V25, NumberOfParticles_Run4$V26,
                                    NumberOfParticles_Run4$V27, NumberOfParticles_Run4$V28,
                                    NumberOfParticles_Run4$V29,
                                NumberOfParticles_Run4$V30, NumberOfParticles_Run4$V31,
                                    NumberOfParticles_Run4$V32, NumberOfParticles_Run4$V33,
                                    NumberOfParticles_Run4$V34, NumberOfParticles_Run4$V35,
                                    NumberOfParticles_Run4$V36,
                                NumberOfParticles_Run4$V37, NumberOfParticles_Run4$V38,
                                    NumberOfParticles_Run4$V39, NumberOfParticles_Run4$V40,
                                    NumberOfParticles_Run4$V41, NumberOfParticles_Run4$V42,
                                    NumberOfParticles_Run4$V43,
                                NumberOfParticles_Run4$V44, NumberOfParticles_Run4$V45,
                                    NumberOfParticles_Run4$V46))
Dataset_Run4_2 <- as.data.frame(cbind(Time_Vec4, Size_Vec4, Number_Vec4))

write.table(Dataset_Run4_2, file="Omega100_r0.01_Run4_GRID_MADLS_Intensity.txt",
            row.names=FALSE, col.names=FALSE, sep=",")
Dataset_Run4_3 <- read.table(file = "Omega100_r0.01_Run4_GRID_MADLS_Intensity.txt", header = FALSE,
    sep=",", dec=".")

Grid_Time4 <- Dataset_Run4_3$V1
Grid_Size4 <- Dataset_Run4_3$V2
Grid_Number4 <- Dataset_Run4_3$V3


Dataset_Run4_3 %>% ggplot(aes(x = Grid_Size4, y = Grid_Time4, z = Grid_Number4, fill = Grid_Number4))
    +
  geom_raster(aes(fill=Grid_Number4)) +
  scale_y_continuous(breaks = seq(0, 13500, by = 1500)) +
  scale_fill_gradient(low="blue", high="yellow")      #limits=c(0,50)
dev.off()

#Run5
tiff("Run5_r0.01_Omega100_Grid_MADLS_Intensity.tiff", units="in", width=5, height=5, res=300)

Time_Vec5 <- as.data.frame(c(Time1_Vec_Run5, Time2_Vec_Run5, Time3_Vec_Run5, Time4_Vec_Run5, Time5_Vec
    _Run5, Time6_Vec_Run5, Time7_Vec_Run5,
                                Time8_Vec_Run5, Time9_Vec_Run5, Time10_Vec_Run5, Time11_Vec_Run5, Time12_
                                    Vec_Run5, Time13_Vec_Run5, Time14_Vec_Run5,
                                Time15_Vec_Run5, Time16_Vec_Run5, Time17_Vec_Run5, Time18_Vec_Run5,
                                    Time19_Vec_Run5, Time20_Vec_Run5, Time21_Vec_Run5,
                                Time22_Vec_Run5, Time23_Vec_Run5, Time24_Vec_Run5, Time25_Vec_Run5,
                                    Time26_Vec_Run5, Time27_Vec_Run5, Time28_Vec_Run5,
                                Time29_Vec_Run5, Time30_Vec_Run5, Time31_Vec_Run5, Time32_Vec_Run5,
                                    Time33_Vec_Run5, Time34_Vec_Run5, Time35_Vec_Run5,
                                Time36_Vec_Run5, Time37_Vec_Run5, Time38_Vec_Run5, Time39_Vec_Run5,
                                    Time40_Vec_Run5, Time41_Vec_Run5, Time42_Vec_Run5,
                                Time43_Vec_Run5, Time44_Vec_Run5, Time45_Vec_Run5))
Size_Vec5 <- as.data.frame(c(Size2, Size2, Size2, Size2, Size2, Size2, Size2, Size2, Size2, Size2,
    Size2, Size2,
                                Size2, Size2, Size2, Size2, Size2, Size2, Size2, Size2, Size2, Size2,
                                    Size2, Size2,
                                Size2, Size2, Size2, Size2, Size2, Size2, Size2, Size2, Size2, Size2,
                                    Size2, Size2,
                                Size2, Size2, Size2, Size2, Size2, Size2, Size2, Size2, Size2))
Number_Vec5<- as.data.frame(c(NumberOfParticles_Run5$V2, NumberOfParticles_Run5$V3, NumberOfParticles_
    Run5$V4, NumberOfParticles_Run5$V5, NumberOfParticles_Run5$V6, NumberOfParticles_Run5$V7,
    NumberOfParticles_Run5$V8,
                                NumberOfParticles_Run5$V9, NumberOfParticles_Run5$V10, NumberOfParticles
                                    _Run5$V11, NumberOfParticles_Run5$V12, NumberOfParticles_Run5$V13,
                                    NumberOfParticles_Run5$V14, NumberOfParticles_Run5$V15,
                                NumberOfParticles_Run5$V16, NumberOfParticles_Run5$V17,
                                    NumberOfParticles_Run5$V18, NumberOfParticles_Run5$V19,
                                    NumberOfParticles_Run5$V20, NumberOfParticles_Run5$V21,
                                    NumberOfParticles_Run5$V22,
                                NumberOfParticles_Run5$V23, NumberOfParticles_Run5$V24,
                                    NumberOfParticles_Run5$V25, NumberOfParticles_Run5$V26,
                                    NumberOfParticles_Run5$V27, NumberOfParticles_Run5$V28,
                                    NumberOfParticles_Run5$V29,
                                NumberOfParticles_Run5$V30, NumberOfParticles_Run5$V31,
                                    NumberOfParticles_Run5$V32, NumberOfParticles_Run5$V33,
```

```
                                        NumberOfParticles_Run5$V34, NumberOfParticles_Run5$V35,
                                        NumberOfParticles_Run5$V36,
                                    NumberOfParticles_Run5$V37, NumberOfParticles_Run5$V38,
                                        NumberOfParticles_Run5$V39, NumberOfParticles_Run5$V40,
                                        NumberOfParticles_Run5$V41, NumberOfParticles_Run5$V42,
                                        NumberOfParticles_Run5$V43,
                                    NumberOfParticles_Run5$V44, NumberOfParticles_Run5$V45,
                                        NumberOfParticles_Run5$V46))
Dataset_Run5_2 <- as.data.frame(cbind(Time_Vec5, Size_Vec5, Number_Vec5))

write.table(Dataset_Run5_2, file="Omega100_r0.01_Run5_GRID_MADLS_Intensity.txt",
            row.names=FALSE, col.names=FALSE, sep=",")
Dataset_Run5_3 <- read.table(file = "Omega100_r0.01_Run5_GRID_MADLS_Intensity.txt", header = FALSE,
    sep=",", dec=".")

Grid_Time5 <- Dataset_Run5_3$V1
Grid_Size5 <- Dataset_Run5_3$V2
Grid_Number5 <- Dataset_Run5_3$V3


Dataset_Run5_3 %>% ggplot(aes(x = Grid_Size5, y = Grid_Time5, z = Grid_Number5, fill = Grid_Number5))
    +
  geom_raster(aes(fill=Grid_Number5)) +
  scale_y_continuous(breaks = seq(0, 13500, by = 1500)) +
  scale_fill_gradient(low="blue", high="yellow")      #limits=c(0,50)
dev.off()

#Combined_Grid_Plot_r0.01
tiff("Combined_r0.01_Omega100_Grid_MADLS_Intensity.tiff", units="in", width=5, height=5, res=300)
Number_Vec_Combined <- (Number_Vec1 + Number_Vec2 + Number_Vec3 + Number_Vec4 + Number_Vec5)/5
Time_Vec_Combined <-  Dataset_Run6
Dataset_Combined_2 <- as.data.frame(cbind(Time_Vec_Combined, Size_Vec5, Number_Vec_Combined))
write.table(Dataset_Combined_2, file="Omega100_r0.01_Combined_GRID_MADLS_Intensity.txt",
            row.names=FALSE, col.names=FALSE, sep=",")
Dataset_Combined_3 <- read.table(file = "Omega100_r0.01_Combined_GRID_MADLS_Intensity.txt", header =
    FALSE, sep=",", dec=".")

Grid_Time_Combined <- Dataset_Combined_3$V1
Grid_Size_Combined <- Dataset_Combined_3$V2
Grid_Number_Combined <- Dataset_Combined_3$V3

Dataset_Combined_3 %>% ggplot(aes(x = Grid_Size_Combined, y = Grid_Time_Combined, z = Grid_Number_
    Combined, fill = Grid_Number_Combined)) +
  geom_raster(aes(fill=Grid_Number_Combined)) +
  scale_y_continuous(breaks = seq(0, 13500, by = 1500)) +
  scale_fill_gradient(low="blue", high="yellow",limits=c(0,15))      #limits=c(0,50)
dev.off()

a <- data.frame(matrix(ncol=1,nrow=150))


stdev <- function(timestep){
  for (i in 1:150){
    a[i,1] <- sd(c(NumberOfParticles_Run1[i,timestep],NumberOfParticles_Run2[i,timestep],
        NumberOfParticles_Run3[i,timestep], NumberOfParticles_Run4[i,timestep], NumberOfParticles_
        Run5[i,timestep]))
  }
  return(a)
}

b <- data.frame(matrix(ncol=45,nrow=150))

stdev(2)

for (i in 1:45){

  b[,i] <- stdev(i+1)
}
c <- c(b[,1],b[,2],b[,3],b[,4],b[,5],b[,6],b[,7],b[,8],b[,9],b[,10],b[,11],b[,12],b[,13],b[,14],b
    [,15],b[,16],
       b[,17],b[,18],b[,19],b[,20],b[,21],b[,22],b[,23],b[,24],b[,25],b[,26],b[,27],b[,28],b[,29],b
           [,30],b[,31],b[,32],
       b[,33],b[,34],b[,35],b[,36],b[,37],b[,38],b[,39],b[,40],b[,41],b[,42],b[,43],b[,44],b[,45])

#Combined_Grid_Plot_r0.01_Errormargin
tiff("Combined_STDev_r0.01_Omega100_Grid_MADLS_Intensity.tiff", units="in", width=5, height=5, res
    =300)
Number_Vec_Error <- c
Time_Vec_Combined <-  Dataset_Run6
Dataset_Error_2 <- as.data.frame(cbind(Time_Vec_Combined, Size_Vec5, Number_Vec_Error))
write.table(Dataset_Error_2, file="Omega100_r0.01_Combined_Error_GRID_MADLS_Intensity.txt",
            row.names=FALSE, col.names=FALSE, sep=",")
Dataset_Error_3 <- read.table(file = "Omega100_r0.01_Combined_Error_GRID_MADLS_Intensity.txt", header
    = FALSE, sep=",", dec=".")
Grid_Time_Error <- Dataset_Error_3$V1
Grid_Size_Error <- Dataset_Error_3$V2
Grid_Number_Error <- Dataset_Error_3$V3

Dataset_Error_3 %>% ggplot(aes(x = Grid_Size_Error, y = Grid_Time_Error, z = Grid_Number_Error, fill =
     Grid_Number_Error)) +
  geom_raster(aes(fill=Grid_Number_Error)) +
  scale_y_continuous(breaks = seq(0, 13500, by = 1500)) +
  scale_fill_gradient(low="blue", high="yellow",limits=c(0,15))      #limits=c(0,50)
dev.off()
```